J Mater Sci (2020) 55:6242–6304

Review

A glimpse on all-solid-state Li-ion battery (ASSLIB) performance based on novel solid polymer electrolytes: a topical review

Anil Arya[1] and A. L. Sharma[1,*]

[1] *Department of Physical Sciences, Central University of Punjab, Bathinda, Punjab 151001, India*

Received: 9 October 2019
Accepted: 10 February 2020

ABSTRACT

All-solid-state batteries are swiftly gaining the attention of the research community owing to their widespread applications in electric vehicles, digital electronics, portable appliances, etc. A battery comprises three components: cathode, anode and electrolyte. An electrolyte is the heart of the battery and plays a crucial role in the overall performance of the battery. In order to make the review more focused, all-solid-state Li-ion batteries (ASSLIBs) have been considered. This review covers the architecture of ASSLIBs, advantages, and characteristics of the solid polymer electrolytes. The important preparation methods are summarized, followed by the characterizations for testing the suitability of electrolytes for solid-state batteries. The discussion is focused on the 'state of the art' in the field of solid-state batteries, device fabrication, and comparison in terms of capacity, energy density, and cyclic stability. In the last section, the ion conduction mechanism in different solid polymer electrolytes is discussed. Finally, it is tried to give a possible outlook for developing future hybrid and multifunctional electrolytes which can act as a bridge for developing solid-state batteries covering a broad range of applications.

Introduction

Energy requirements are always being on top priority in any society across the globe. Continuous consumption, rapid growth in population, and depletion of traditional resources (such as fossil fuels, coal, and biomass) push the scientists working in this field for some better alternative. At the same time, the conventional source of energy is not well appropriate to provide us back up in the near future. In contemporary period, they are rapidly polluting the environment (global warming and air pollution), resulting in the implementation of environmental norms at national/international forums. The only alternative that seems to be feasible is to switch from conventional/traditional to renewable/clean-green sources of energy. The alternative renewable sources of energy are hydro energy, solar energy, wind energy, and tidal energy. These alternative steps certainly fulfill the need of energy, but unable to store

---

Address correspondence to E-mail: alsharma@cup.edu.in

https://doi.org/10.1007/s10853-020-04434-8

the energy without memory loss. In order to eliminate these issues of storage, the best players are batteries and supercapacitors (as they can deliver the energy as per need and can be moved from one place to another as per requirement [1–4].

In order to store energy without memory effect, Li-ion batteries seem to be the best. The lithium-ion batteries have been developed in various forms (liquid/gel/semi-gel) since their existence. The development of Li-ion batteries in a solid state is a major breakthrough in this line. Batteries are generally classified into two categories depending on their charging/discharging performance. The primary batteries are called the disposal batteries, which means once used then dispose of. It leads to manifold complications in the environment (soil, animal, and human). The limited energy density, capacity, and large size prevent their use in the broad range of the applications only. It is, therefore, recommending most of the time for the development of secondary/rechargeable batteries until its very essential that could be able to eliminate these issues. Conventional, secondary batteries have the ability to bring charges again after being used once and provide again the energy as per the number of cycles. So, secondary batteries (especially Li-ion) are the most attractive candidate due to associated high energy density and capacity. The first Li-ion battery (LIB) was commercialized by SONY in 1991, and thereafter, it becomes the most efficient and necessary source of energy. LIBs are tremendously used in a broad range of applications such as portable electronics, grid energy, electric vehicles, space vehicles, and entire electronic industries. The basic working principle of the battery is that it stores the energy in the chemical form and converts/delivers it in the electrical form without any exhaustion of the pollutants/effluent. The important parameters of the battery that determine the performance are specific capacity, cyclic stability, capacity retention, energy density, and life span [5–7].

A general LIB has four components: cathode (+ ve), anode (− ve), electrolyte, and separator (Fig. 1i) [8]. The most common cathode materials are transition metal oxide-based materials ($LiCoO_2$, $LiFePO_4$, etc.), and the most common anode that dominates graphite. The electrolyte may be in liquid/solid/semi-solid form and provides the conductive medium for ion migration. Another important component is the separator that separates the electrodes and prevents short-circuiting of the battery. The key point in the battery mechanism is the exchange of electrons that occurs via the redox reaction (oxidation/reduction) [9, 10].

The common issues that are faced by the research community in the batteries are summarized in Fig. 1ii. The enhancement of the overall cell performance depends on the active materials of electrodes, electrolyte material, and the design architecture [11]. Some of the generally used cathode materials that can be used for the fabrication of the cell are summarized in Table 1. The important parameters such as voltage, capacity, crystal density, specific energy, and volumetric energy are shown [12].

The electrolyte is one of the most crucial components of the battery and participates in both charging and discharging operations. Electrolyte acts as a carpet for ion migration in the battery. The electrolyte must have high ionic conductivity, negligible electronic conductivity, broad voltage stability window, being inert toward other cell components, and good thermal/mechanical stability [15]. The existing battery systems are using organic solvents for that electrolyte, and this raises many serious issues such as the possibility of leakage, flammable nature, explosion issue, bulky in size, and complex transportation process. So, the research focus is toward the development of safe and stable electrolytes that can eliminate the above-said issues and may serve as the ideal electrolyte in the battery's systems [2, 16, 17].

Several reviews have focused on the developments of different types of electrolytes (solid/gel) for Li-ion battery applications. Prof. Goodenough reviewed the progress in solid electrolytes and gel polymer/oxide composites for low-cost and highly efficient electrochemical cells [18]. The interfacial behavior effect has been examined on the ionic conductivity that is linked with electrode–electrolyte contact [19]. The effect of nanofiller (carbon nanotube, graphene, and clay montmorillonite platelet) on the properties of polymer nanocomposites has been reviewed by Mrinal Bhattacharya [20]. Xue et al. [21] reviewed the progress in the PEO-based polymer electrolytes for Li-ion batteries. Various types of polymer electrolytes (block, grafted, hyperbranched, etc.) have been summarized for the efficient LIB based on PEO [22]. Saito et al. [23] investigated the influence of morphology on the separator membrane for LIB. The control of morphology allows the control of microviscosity of ions and facilitates the development of an efficient storage system. Review by Xia et al. [24]

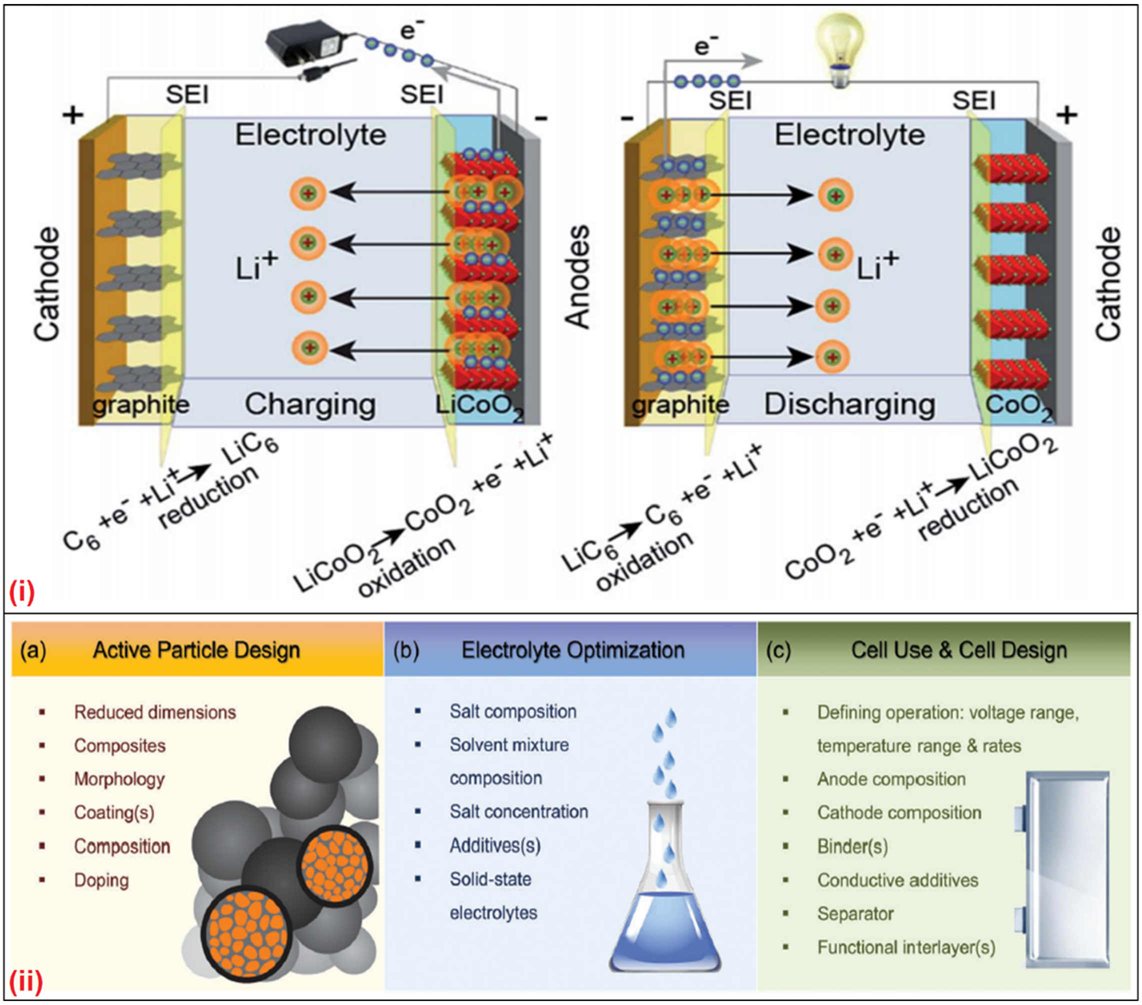

Figure 1 **i** Charge–discharge process of a lithium-ion cell using graphite and $LiCoO_2$ electrodes [Reproduced with permission from Ref. [8] © Royal Society of Chemistry 2016], and **ii** general strategies for enhancement of the performance of cells comprising conversion-type cathode materials: (a) optimization of the architecture, microstructure, size, and composition of active particles to achieve enhanced rate performance and stability, while minimizing undesirable interactions with electrolytes; (b) optimization of the electrolyte composition in order to prevent or mitigate cathode dissolution and minimize formation of undesirable species upon electrolyte decomposition; (c) specification of safe battery operation regimes and optimization of the cell construction, such as the tuning properties of electrodes to achieve the desired ionic and electronic conductivities as well as mechanical stability at the electrode level and introduction of additional functional elements (such as use of interlayer or separator barrier coatings or neutralizing species, etc.) that mitigate negative impacts of undesirable reactions (Reproduced with permission from Ref. [11] © RSC Publishing 2017).

highlighted the progress in the electrolytes (aqueous, organic) for batteries and supercapacitor applications. Many reviews focused on the polymer electrolyte benefit for solid-state batteries, also the strategies for ionic migration enhancement, and energy chemistry between the electrolyte and anode/cathode [25–28]. Schnell et al. [29] reviewed the progress and challenges for the development of all-solid-state lithium-ion and lithium metal batteries with the main purpose to fill the gap between laboratory and industry. Tong et al. [30] summarized the compatibility of various Li salts with the $LiFePO_4$ cathode. Famprikis et al. [31] explored the progress in the inorganic solid electrolytes for fulfilling the ASSB concept. The enhancement in ion transport, mechanical and electrochemical properties have been reviewed followed by the challenge in coming future in the path of commercialization of ASSB.

Figure 2 shows the progress in the electrolyte, starting from solid ionic conductor to polymeric

Table 1 Best-case (low rate), practically achievable, working voltages and capacities versus Li/Li$^+$ for various cathode materials (Reproduced with permission from Ref. [12–14], © Cambridge University Press 2014)

Material	Voltage (Ave. vs. Li/Li$^+$)	Capacity (mAh/g)	Crystal density (g/cm^{-3})	Tap density (g/cm^{-3})	Sp. En. (Wh/Kg)	Vol. En. (Wh/l)
$LiCoO_2$	3.8	150	5.10	2.9	570	2907
$LiNi_{1/3}Mn_{1/3}Co_{1/3}O_2$ (NMC)	3.7	170	4.75	2.5	629	2988
$LiNi_{0.8}Co_{0.15}Al_{0.05}O_2$ (NCA)	3.7	185	4.85	2.5	685	3322
$LiMn_2O_4$	4.0	110	4.31	2.5	440	1896
$LiFePO_4$	3.4	160	3.0	1.5	544	1958
$0.5Li_2MnO_3{\cdot}0.5LiMO_2$*	3.6	230	4.30	1.8	828	3560
$LiMn_{1.5}Ni_{0.5}O_4$	4.7	135	4.40	2.0	635	2794

Crystal densities are theoretical values, while tap densities represent typical, practical values, determined experimentally as the actual weight per unit volume occupied by a given material. Volumetric energy densities are calculated using the crystal densities for comparison as the optimum, final electrode densities will vary among materials

*Not yet commercialized. Capacity and voltage targets for 0.5 Li_2 $MnO_3{\cdot}0.5$ $LiMO_2$ are based on the US Department of Energy's end-of-life goals for composite materials. 13 Crystal density is calculated as an average of Li_2MnO_3 and $LiMn_{0.5}Ni_{0.5}O_2$

electrolytes in 1973, followed by composite polymer electrolyte, garnet type electrolyte, and NASCION type electrolyte. Then, the development and strategies adopted to develop all-solid-state LIBs (ASSLIBs) based on solid-state electrolyte (SSE) are still an attractive research area [32].

Architecture of ASSBs

Another most crucial point regarding ASSBs is their architectures, and one of the most promising is shown in Fig. 3. Three possible configurations are: (1) all three components (cathode, anode, electrolyte) in solid form, (2) liquid/polymer-based cathode along with solid electrolyte and anode, and (3) cell with cathode and separator only (here anode formation occurs after the first charge) [33].

All-solid-state Li-ion battery (ASSLIBs) performance parameters and advantages

Some of the important parameters that are used to characterize the battery performance are shown in Fig. 4a, b. The development of the future energy need motivates us to develop an all-solid-state battery that can eliminate the issues associated with the existing commercial batteries. The solid electrolyte will provide some unique advantages such as smaller size and high energy density. So, the advantages associated with the ASSBs are summarized in Fig. 4b to highlight their potential to fulfill this gap of the energy storage/conversion devices. Figure 5 compares the voltage w.r.t. size for present LIB and ASSBs.

Table 2 shows the important parameters used to examine the performance of the cell [8].

Key parameters for electrolyte optimization

To fulfill the need of ASSB's with long-term cyclic stability and performance, the electrolyte is a crucial part. The key properties of electrolytes need to be examined: ionic conductivity, cation/ion transport number, voltage stability window, and stability properties. The following section highlights the details of key properties and how they are influenced by the host polymer matrix or additives. Some of the important parameters which are summarized are crystallinity and morphology, ionic conductivity, cation transport number, ion transference number, electrochemical stability window, and stability (thermal/chemical/mechanical) properties [34–36].

Crystallinity and morphology Degrees of crystallinity (X_C) from XRD and DSC are determined using the following expression:

$$X_C = \frac{A_C}{A_C + A_A} \quad (1)$$

where A_C and A_A refer to the area of crystalline and amorphous regions, respectively.

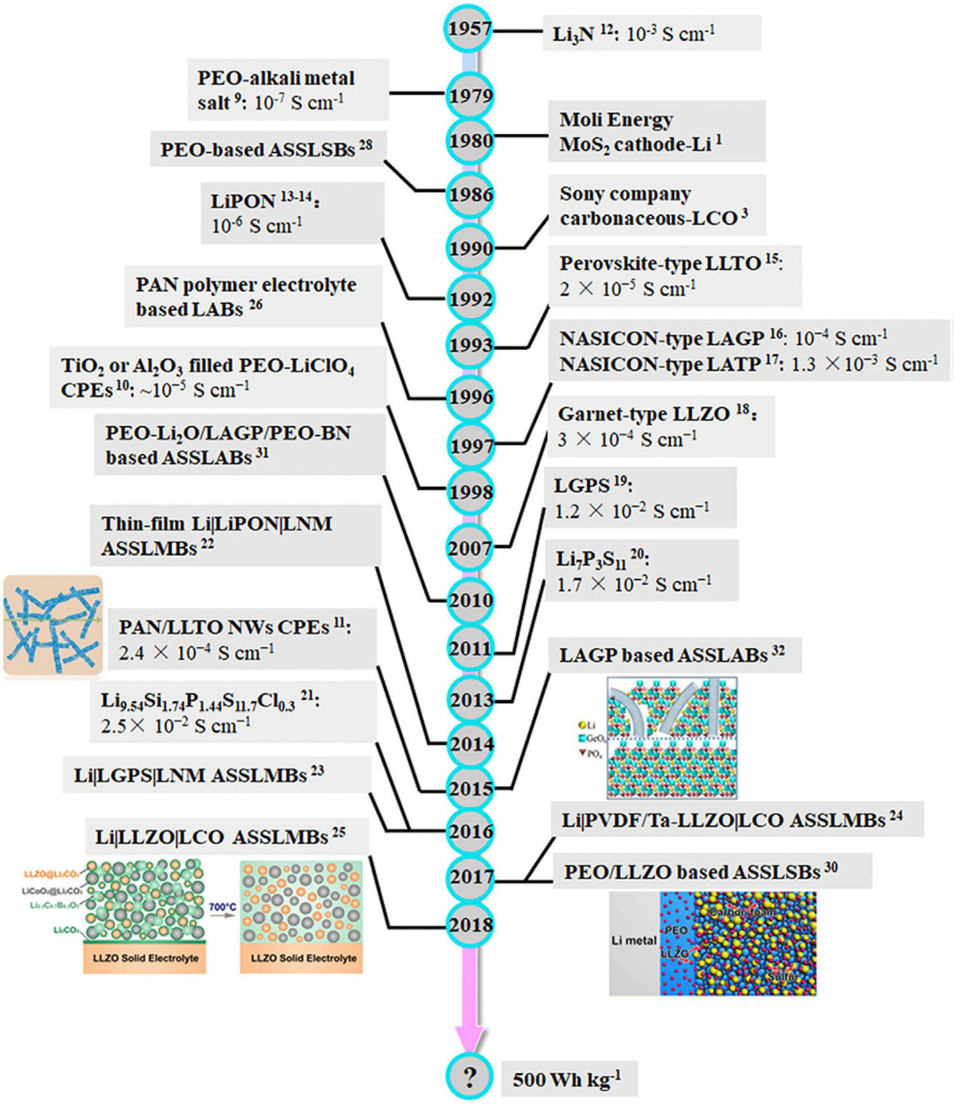

Figure 2 A brief chronology of the development of typical SSEs toward ASSLMBs (Reproduced with permission from Ref. [32] © Elsevier 2018).

The percentage of crystallinity (X_C) was calculated using

$$X_c = \frac{\Delta H_m}{\Delta H_m^o} \times 100 \tag{2}$$

where ΔH_m is the melting enthalpy obtained from the DSC measurement and ΔH_m^o is the melting enthalpy of pure 100% crystalline host polymer.

Ionic conductivity The conductivity of polymer electrolyte is directly proportional to the number of free charge carriers available in the polymer matrix and mobility as expressed by the equation:

$$\sigma = \sum n_i z_i \mu_i \tag{3}$$

where n_i, z_i, and μ_i refer to the number of charge carriers, ion charge, and ion mobility, respectively. Two important parameters are mobility (μ) and diffusion coefficient (D) expressed by the Nernst–Einstein relation.

$$\mu = \frac{|z|eD}{k_B T} \tag{4}$$

$$n = \frac{\sigma k_B T}{(|z|e)^2 D} \tag{5}$$

where k_B is the Boltzmann constant and T is the absolute temperature.

The ionic conductivity is determined by the impedance spectroscopy technique in a certain frequency range (generally 1 Hz–1 MHz). The polymer electrolyte is sandwiched between the two stainless steel (SS) electrodes and a weak ac signal (usually 10–

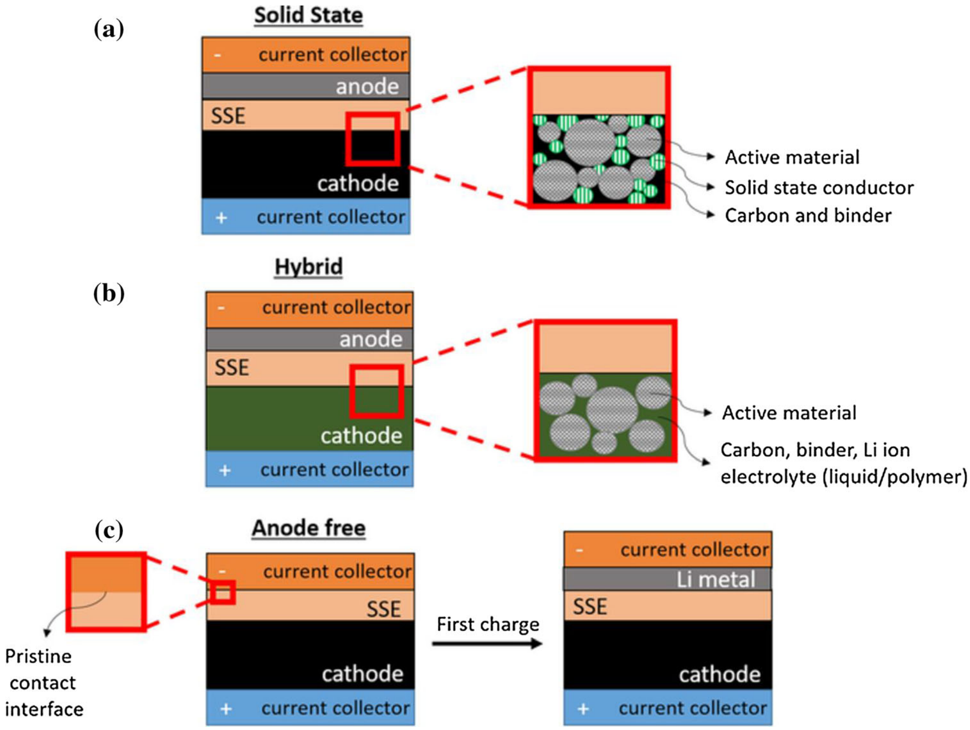

Figure 3 An illustration of main cell architectures utilized in solid-state battery research to date. **a** All-solid-state configuration utilizing a solid state cathode interfaced with a solid electrolyte and high energy density solid anode; **b** a hybrid approach using a liquid or polymer-based cathode interfaced with a solid electrolyte and high energy density anode; and **c** anode-free design wherein the cell is constructed with only a cathode and separator, while the metal anode is formed upon the first charge [Reproduced with permission from Ref. [33] © Electrochemical Society 2017].

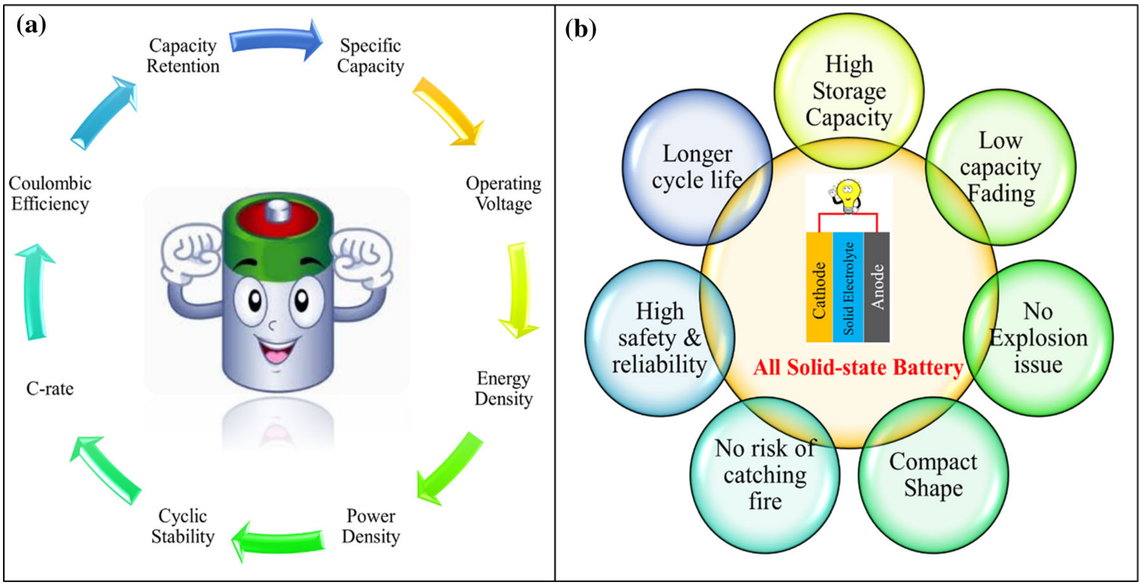

Figure 4 **a** Battery performance parameters, and **b** advantages of all-solid-state battery (ASSBs).

20 mV) is applied across the cell. The ionic conductivity may be evaluated from the equation expressed:

$$\sigma = \frac{t}{R_b A} \quad (6)$$

where 't' is the thickness of the polymer electrolyte films, A is the area of the SS electrodes, and R_b is the bulk resistance extracted from the intercept on the real axis of the Nyquist plot (Z'' vs. Z'). As electrical conductivity is linked with the number of the charge carriers as well as the flexibility of the polymer chain. So, temperature also plays an effective role in enhancing the ionic conductivity owing to the increase in the flexibility of the polymer chains that activate the faster migration of charge carriers.

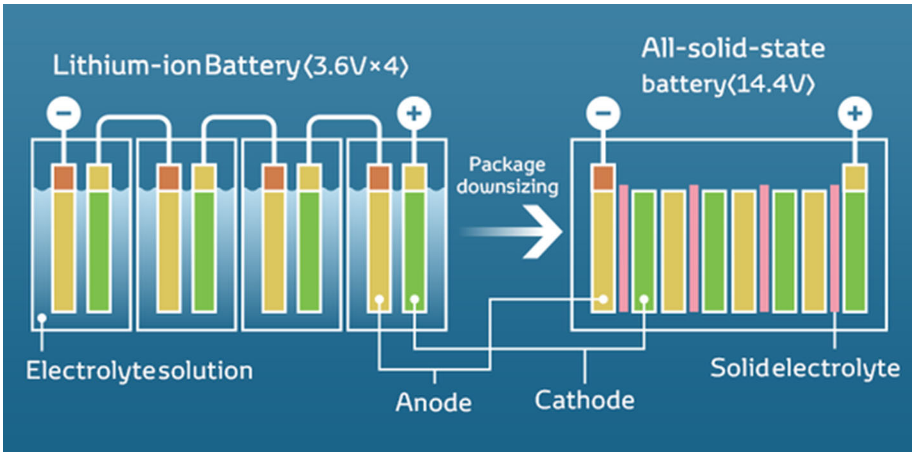

Figure 5 Comparison of traditional battery and all-solid-state battery in terms of voltage https://www.machinedesign.com/motion-control/solid-state-batteries-evs-key-long-distance-driving.

Table 2 Essential parameters for testing the performance of a lithium-ion cell (Reproduced with permission from Ref. [8], © Royal Society of Chemistry 2016)

Parameters	Measuring unit	Measuring formula	Information
Operating voltage	Volts (V)	Instrumental	Energy density and safety
Current density	mA g^{-1}	Instrumental	For testing rate capabilities
Theoretical capacity	mAh g^{-1}	$\mathrm{TC} = \frac{F \times x}{3.6 \times M.M \times y}$	Lithium-ion storage capability
Gravimetric capacity	mAh g^{-1}	$C = \frac{I(\mathrm{mA}) \times t(\mathrm{h})}{m(\mathrm{g})}$	Li^+ storage capability measured per unit mass
Areal capacity	mAh cm^{-2}	$C = \frac{I(\mathrm{mA}) \times t(\mathrm{h})}{A(\mathrm{cm}^2)}$	Li^+ storage capability measured per unit area
Volumetric capacity	mAh cm^{-2}	$C = \frac{I(\mathrm{mA}) \times t(\mathrm{h})}{V(\mathrm{cm}^3)}$	Li^+ storage capability measured per unit volume
Energy density	Wh g^{-1} or Wh cm^{-2} or Wh cm^{-3}	$E = C \times V$	How much energy can be extracted
Power density	W g^{-1} or W cm^{-2} or W cm^{-3}	$P = I \times V$	How fast the energy can be extracted
C_{rate}	h^{-1}	$C_{\mathrm{rate}} = \frac{J(\mathrm{mAg}^{-1})}{C(\mathrm{mAhg}^{-1})}$	Rate of charging/discharging
Coulombic efficiency	N/A	$\%E = \frac{C_{\mathrm{charging}}}{C_{\mathrm{dishcarging}}} \times 100$	Reversible capacity

Cation transference number The ionic conductivity of the polymer electrolytes is linked with the number of cations contributing to the ion dynamics. Therefore, cation transference number (t_+) is evaluated to obtain information about ion transport and also to correlate with ionic conductivity. In the case of polymer electrolytes, the cation is supposed to contribute to ion dynamics, while anion remains in the immobilized state with a polymer backbone. The anion hanging is the key to eliminate the cell polarization issue for better cyclic stability. For an ideal polymer electrolyte, t_+=1. The anion migration can be blocked by using anion receptors and using bulky anion. The cation transference number is determined by a combination of two techniques, i.e. ac impedance and d.c. polarization technique. The equation used to obtain t_+ is Bruce–Vincent equation and is expressed as:

$$t_{\mathrm{Li}^+} = \frac{I_s(V - I_i R_i)}{I_i(V - I_s R_s)} \tag{7}$$

here V is the applied voltage across cell configuration, I_i and I_s are the initial and steady-state currents, respectively, and R_i and R_s are the interfacial resistance before and after polarization, respectively.

Electrochemical stability window (ESW) The energy density and capacity of the battery is a crucial parameter and is linked with the voltage window of the battery electrolyte. ESW allows the user to operate the battery in a safe range and also gives insights about the interfacial resistance with the electrodes. ESW is defined as the difference between the oxidation and reduction potential. So, before fabricating the cell ESW is examined. As recharge-ability (reversibility) is fundamental characteristics of the Li-ion battery, so the oxidation and reduction must be within this voltage limit [37]. The ESW is obtained by performing the linear sweep voltammetry (LSV) technique, and at a particular voltage onset of current occurs. This breakdown voltage is known as the electrochemical stability window of the electrolyte.

Thermal runway issue

One of the most fundamental drawbacks faced by the traditional electrolyte-based battery is that they are flammable and often explode too. This is the key reason that threats the safety of the battery. This process is coined as a “thermal runaway” and arises when there is the uncontrolled reaction inside the battery system. This results in the continuous generation of heat and gas release during these reactions increases the internal pressure that ultimately results in the explosion of the battery [38, 39]. Figure 6 shows the detailed thermal runway process from initial heating to the final explosion.

The onset of overheating (stage 1) This is the initial stage, and here three important factors that threat safety are overcharging, exposure to high temperature, and cell architecture defects (poor wiring, short-circuit). The most important is the internal short-circuiting owing to the dendrite growth formation, collision of EV, and high current rate. Now, there is a transition from *stage 1* (initial heating) to *stage 2* (accumulation of heat).

Table 3 summarizes the fire and explosion issues faced by users of the LIB system in the last 5 years. It may be concluded from the table that the key reason is the thermal runaway process (TRP). TRP is the result of the electrolyte nature, high charge–discharge rate and poor battery packaging [40]. Since 1991, the birth year of Li-ion battery, 191 lithium battery incidents have been reported.

Heat accumulation and gas release process (stage 2) At this stage, there is a rapid increase in the heating inside the battery pack. Some of the important reactions that take place are: (1) overheating decomposes the solid electrolyte interphase (SEI), (2) flammable gases are released due to reaction of anode with electrolyte, (3) melting of separator at high temperature leads to short-circuiting, and (4) breakdown of cathode due to heat leads to exothermic reaction which results in the release of oxygen. In brief, a lot of oxygen gets accumulated inside the battery and transition from *stage 2* to *stage 3* occurs.

Combustion and explosion (stage 3) This is the final stage; here the explosion of the battery occurs due to favorable conductions provided to the liquid electrolyte by the accumulated oxygen. This self-heating of the battery system results in high pressure inside the battery pack and an explosion occurs.

As it is well known that the electrolyte/separator is placed between the electrodes and plays an effective role in both the charging and discharging process. The role of the electrolyte is to provide a medium for the shuttling of ions, while the separator keeps away the electrode for the safe operation of the battery [41, 42]. So, this component can be a key player in preventing the thermal runway (TR) issue in the electrolyte and the separator. The most promising alternative is the ceramic/polymer/glass electrolyte and has the potential to eliminate the issues that result in TR. The use of these electrolytes will eliminate the issue of electrolyte melting that leads to additional reactions in the battery and finally battery shutdown due to short-circuiting [43]. So, we need to focus on increasing the thermal stability range of the electrolyte and the above-said separator has the potential to bridge this gap.

Dendrites: growth mechanism and prevention strategies

One of the major factors that threats battery safety is the formation of dendrites growth on the anode which results in a decrease in capacity, short-circuiting issue, and capacity fading. When dendrite grows, out of many only one reaches the opposite electrode first and short-circuits the battery, while high-current density melts the dendrite. This first dendrite acts as a fuse before other dendrites reach [44]. Along with this, the Li becomes fractured as shown in Fig. 7i(a), and with cycling process aggregation occurs (Fig. 7i(b). Then there originates the possibility of growth of fractured Li on the fresh anode surface as shown in Fig. 7i(c). Finally, after a long cycling process, a number of dendrites reach the cathode and damage the battery (Fig. 7i(d) [45].

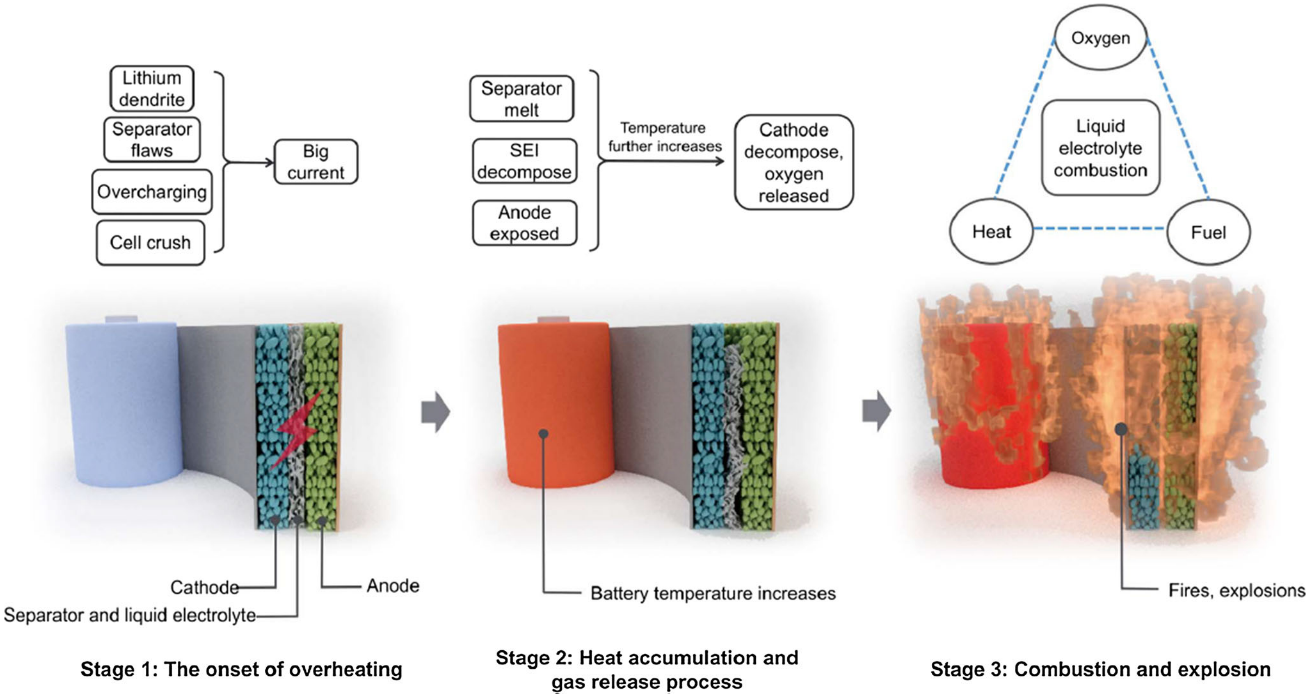

Figure 6 Three stages for the thermal runaway process. Stage 1: The onset of overheating. The batteries change from a normal to an abnormal state, and the internal temperature starts to increase. Stage 2: Heat accumulation and gas release process. The internal temperature quickly rises, and the battery undergoes exothermal reactions. Stage 3: Combustion and explosion. The flammable electrolyte combusts, leading to fires and even explosions (Reproduced with permission from Ref. [39] © AAAS 2018).

Table 3 Some lithium-ion battery fire and explosion accidents in the past few years (Reproduced with permission from Ref. [40], © Elsevier 2012)

No.	Date	Accidents replay	Fire causes
1	June 2017	Samsung Galaxy Note 7 battery fires and explosions	Caused by overheating due to irregularly sized batteries
2	July 2011	EV bus catch fire, Shanghai, China	Caused by overheated $LiFePO_4$ batteries
3	April 2011	Hangzhou, China	EV taxi catch fire, caused by 16 Ah $LiFePO_4$ battery
4	September 2010	A Boeing B747-400F cargo plane catch fire, Dubai	Caused by overheated lithium batteries
5	April 2010	Acer recalled 2700 laptop batteries, as Dell, Apple, Toshiba, Lenovo and Sony done in 2006	Potential overheating and fire hazards
6	March 2010	Two iPod Nano music player overheating and catching fire, Japan	Caused by overheated lithium batteries
7	January 2010	Two EV buses catch fire, Urumqi, China	Caused by overheated $LiFePO_4$ batteries
8	July 2009	Cargo plane catch fire before fly to USA, Shenzhen, China	Caused by spontaneous combustion of lithium-ion batteries
9	June 2008	Laptop catch fire in a conference, fire burning 5 min, Japan	Caused by overheated battery
10	June 2008	Honda HEV catch fire, Japan	Caused by overheated $LiFePO_4$ batteries

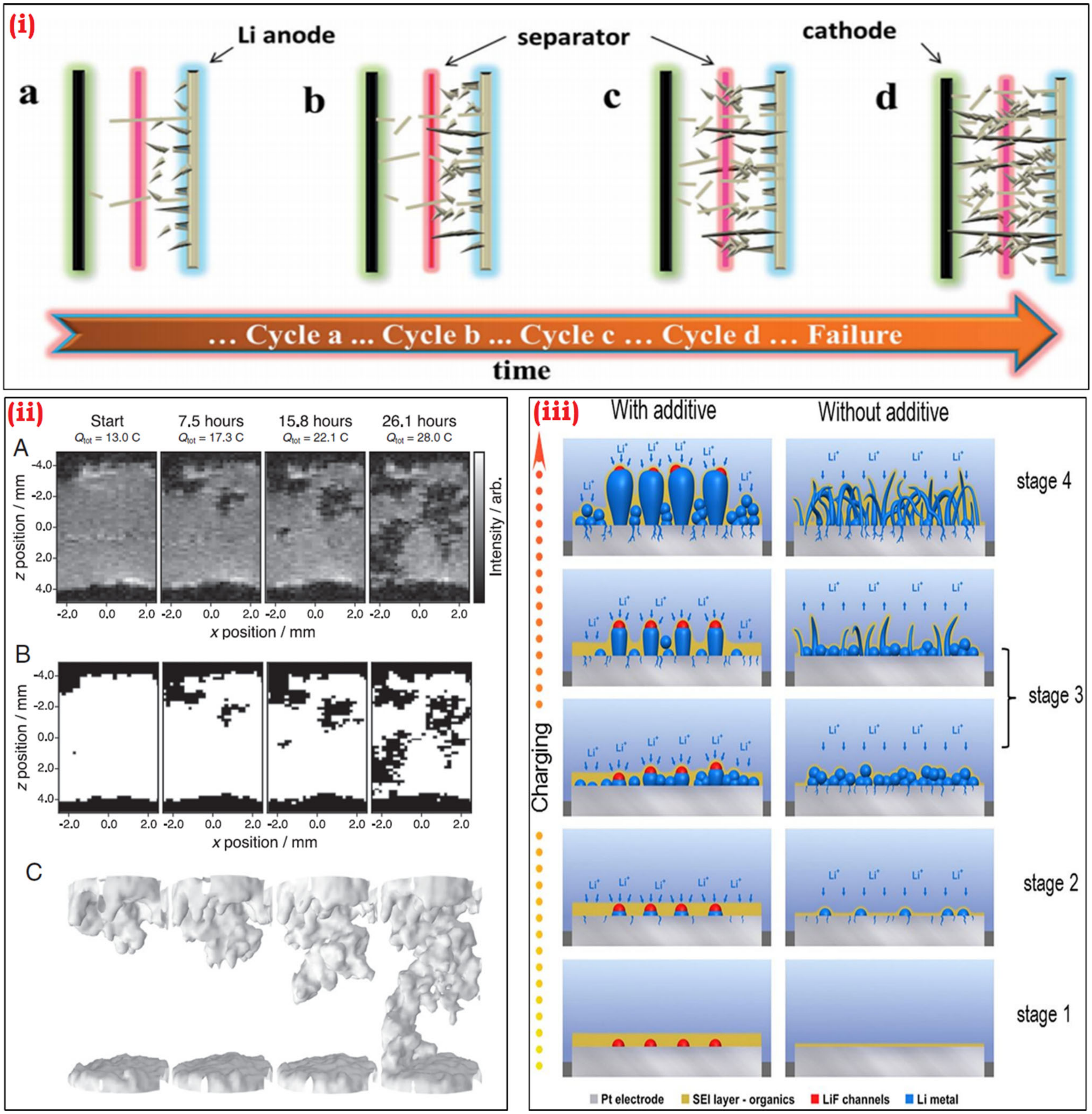

Figure 7 **i** The scheme of the Li dendrite growth during cycling process (Reproduced with permission from Ref. [45] © RSC Publishing 2016), **ii** in situ 1H 3D FLASH imaging results from the electrochemical cell, with each 3D image acquired in 16 min 40 s. The cell was charged at 50 μA (0.16 mA cm^{-2}) for 72 h before these measurements and then charged at 160 μA (0.51 mA cm^{-2}) for the times specified, with the total charge applied also given in coulombs. (A) Two-dimensional slices from four time points. (B) Segmented images of the results from A, where $I_{threshold} = 0.2\ I_{max}$ (C) Three-dimensional segmented images of the same time points with an additional Gaussian filter applied to smoothen the visualization (Reproduced with permission from Ref. [47] © National Academy of Sciences 2016), and **iii** Schematic model illustrating the formation of two distinct forms of Li dendrite structures in the presence (left) and absence (right) of additives (Reproduced with permission from Ref. [38] © MDPI 2018).

The origin of dendrite growth in liquid electrolytes is also explained in terms of a current limit. When the current density is less than limiting current, then Li deposition starts on dendrite protrusion that results in the growth of Li. When the current density is higher than limiting current, Li-ions from the electrolyte starts depositing on the tips of dendrite protrusions. This leads to the growth of dendrite (thread-like structures) which finally short-circuits or may explode the cell [46]. So, this needs to be resolved to develop a battery system with long cycle stability. Recently, Ilott et al. [47] have observed the growth of dendrites using the in situ MRI by examining the changes in the intensities and frequencies of the Li-metal signals. Here, interactions of the dendrite with electrolytes are observed. Figure 7ii(a) shows the 3D images of dendrite growth on anode using ^{1}H FLASH. The growth of dendrite microstructure is clearly observed with the passage of time, and the segmented image is shown in Fig. 7ii(b). Figure 7ii(c) shows the final geometry in 3D using the MRI image.

Recently, Mehdi et al. [48] have examined the role of Li grain size on the dendrites. Figure 7iii compares the dendrite structure in the presence (left) and absence (right) of additives. The figure is divided into four stages for clarity.

Stage 1 Thin film formation in the absence of additive, while large thickness with additive,

Stage 2 Initial nucleation followed by the large Li grain growth (with additive),

Stage 3 Growth of long rods without additive,

Stage 4 Uniformly sized grain growth (left) and a mossy Li deposit (right).

During charging, fast cation diffusion results in Li deposition on the electrode surface, while during discharging rapid stripping of Li occurs which results in high Coulombic efficiency. This ease of Li deposition/stripping facilitates the formation of the Li layer on the surface, which effectively suppresses the dendrite growth formation. Some of the Li dendrite issues are summarized in Table 4.

Prof. Cui group developed a '*smart battery*' based on new technology, which gives a warning before it bursts in flame or overheats using a bifunctional flexible/porous separator (a conducting layer sandwiched in between conventional separators). The third electrode (copper layer of about 50 nm on polymer separator) detects the formation of dendrites and informs before the short-circuiting of the battery. The dendrite alarm mechanism is confirmed by in situ observations. Figure 8i(a) shows the electroplated Li on the Li electrode during the charging process. During this process, growth of dendrite occurs and is examined by monitoring the voltage between the copper layer and the lithium tip ($V_{\mathrm{Cu-Li}}$) on the separator (Fig. 8ii). Initially, it is 3000 mv and drops to zero when dendrite makes contact with the copper layer (near 6–8 min) [57]. Now, it's time to remove the battery to prevent short-circuit.

The same group proposed a new approach to suppress dendrite growth [58]. They used *two additives*: (1) lithium polysulfide and (2) lithium nitrate ($LiNO_3$) for the ether-based electrolyte. Figure 8 iii shows the formation of a weak SEI layer that results in crack formation and growth of dendrites occurs. But, when polysulfide (Li_2S_8) is added to the electrolyte, there is a lowering of the surface area. This pancake-type morphology results in the formation of a stable SEI interface and effectively suppresses the dendrite growth. Zhao et al. [59] in 2017 proposed a new flexible anion-immobilized *ceramic-polymer composite electrolyte* to suppress the dendrite growth formation on Li anode. Figure 8iv shows the dendrite growth suppression mechanism with the use of composite polymer electrolyte as compared to the conventional liquid electrolyte. Kim et al. [60] examined the dendrite growth by fabricating two cells with gel polymer electrolyte (GPE) and composite polymer electrolyte (CPE). It may be noticed from Fig. 8v that the CPE effectively suppresses the dendrite growth and the uniformly dispersed Al_2O_3 nanoparticle acts as a protective barrier.

As electrolyte provides medium for ion migration. The anisotropic distribution of Li-ions on the anode surface results in dendrite growth formation. A number of methods have been reported to resolve the issue of anisotropic distribution [61, 62]. Still, there is no proper mechanism to suppress dendrite formation. So, a new approach to control the Li-ion diffusion and distribution has been proposed by Zhao et al. [63]. They prepared ion distributor by coating commercial polypropylene (PP) separators with solid-state fast ionic conductors [Al-doped $Li_{6.75}La_3Zr_{1.75}Ta_{0.25}O_{12}$ (LLZTO)]. Figure 8vi shows the role of LLZTO as an ion distributor which effectively suppress the dendrite growth as compared to PP separator. The ion conductive channels in the LLZTO make it easier to facilitate uniform distribution and occurrence of the smooth deposition of lithium.

Another important task in the case of battery technologies is to identify the failure (physical/electrical/mechanical/chemical) cause. So, *FMMEA* (failure modes, mechanisms, and effects analysis) methodology is adopted to find out the failure mechanism as shown in Table 5. It provides details of cell components, mode, and cause of failure [64].

Emerging polymerization techniques for polymer electrolytes

To develop the novel polymer electrolyte with enhanced ionic conductivity and mechanical properties, polymerization techniques have grabbed the attention of researchers. The polymerizing of polymer electrolyte is effective in enhancing the ion dynamics and contact of electrolyte with electrodes [65]. Many researchers tried to prepare polymer electrolytes using different polymerization techniques. Khan et el. [66] prepared the block copolymer PPME-b-PSt via the living anionic polymerization technique. But, this technique restricts the block polymerizable sequence and also it is difficult to

Figure 8 **i** A lithium anode and separator-wrapped lithium ▶ counter electrode with copper conductive layer facing the lithium anode housed in a glass cell for in situ optical microscopy observation. During charging of the cell, non-uniform deposition of lithium onto the lithium electrode leads to mossy dendrite formation and growth on the surface. **ii** Voltage profile of the device (Reproduced with permission from Ref. [57] © Springer Nature 2014). **iii** (a) Schematic of the morphologies of lithium deposited on the substrate in different electrolytes. Schematic illustration showing the morphology difference of lithium deposited on the stainless steel substrate in the two electrolytes (both contain lithium nitrate), but (a) without lithium polysulfide (b) containing lithium polysulfide (Reproduced with permission from Ref. [58] © Springer Nature 2015). **iv** Schematic of the electrochemical deposition behavior of the Li metal anode with (A) the PLL solid electrolyte with immobilized anions and (B) the routine liquid electrolyte with mobile anions [Reproduced with permission from Ref. [59] © National Academy of Sciences 2017]. **v** Illustrations explaining the advantageous effect of CPE on the suppression of lithium dendrite growth (Reproduced with permission from Ref. [60] © Royal Society of Chemistry 2013). **vi** Schematic illustration of the electrochemical deposition behaviors of the Li metal anodes using (A) a routine PP separator and (B) a composite separator with the LLZTO layer as an ion redistributor to uniform Li-ion distribution (Reproduced with permission from Ref. [63], © AAAS 2018).

Table 4 Different phenomena of Li dendrite in SSBs using different solid-state electrolytes (Reprinted with permission from Ref. [49], © Elsevier 2018)

Battery	Current density (mA cm^{-2})	Temperature (°C)	Li dendrite	Morphology of Li/electrolyte interface	References
Li/PEO–LiTFSI/Li	0.2	80	Yes	Needle-like Li dendrite	[50]
Li/PEO–LiTFSI/Li	0.7	80	Yes	Tree-like Li dendrite	
Li/PEO–LiTFSI/Li	1.3	80	Yes	Bush-like Li dendrite	
Li/PEO–LiTFSI/Li	0.05, 0.1	80	Yes	Needle-like Li dendrite	[51]
Li/PEO–LiTFSI/Li	0.7	80	Yes	Arborescent like Li dendrite	
V$_2$O$_5$/PEO–LiTFSI/Li	0.22	90	Yes	Moss-like Li dendrite, delaminating and blisters at the Li/electrolyte interface.	[52]
V$_2$O$_5$/PEO–LiTFSI/Li	0.50	90	Yes	Needle-like Li dendrite, delaminating and blisters at the Li/electrolyte interface.	
Li/PEO–LiTFSI/Li	0.175	90	Yes	Needle-like Li dendrite, thermo-fusible effect	[53]
Li/PEO–LiTFSI/Li	0.175	90	Yes	Filamentous Li dendrite lies within the electrode, underneath the polymer/electrode interface	[54]
LiFePO$_4$/Li$_{1.3}$Al$_{0.3}$ Ti$_{1.7}$(PO$_4$)$_3$–PEO–BPEG^a/Li	0.2	60	No	Smooth Li surface	[55]
LiFe$_{0.2}$ Mn$_{0.8}$ O$_4$/Li$_{1.5}$Al$_{0.5}$Ge$_{1.5}$ (PO$_4$)$_3$–PEO(500000)–LiTFSI/Li	–	50	No	–	[56]
LiFe$_{0.2}$Mn$_{0.8}$PO$_4$/PEO (500000)–LiTFSI/Liw	–	50	Yes	Li dendrites piercing the PEO film, dead Li	

[a] BPEG is boronized polyethylene glycol

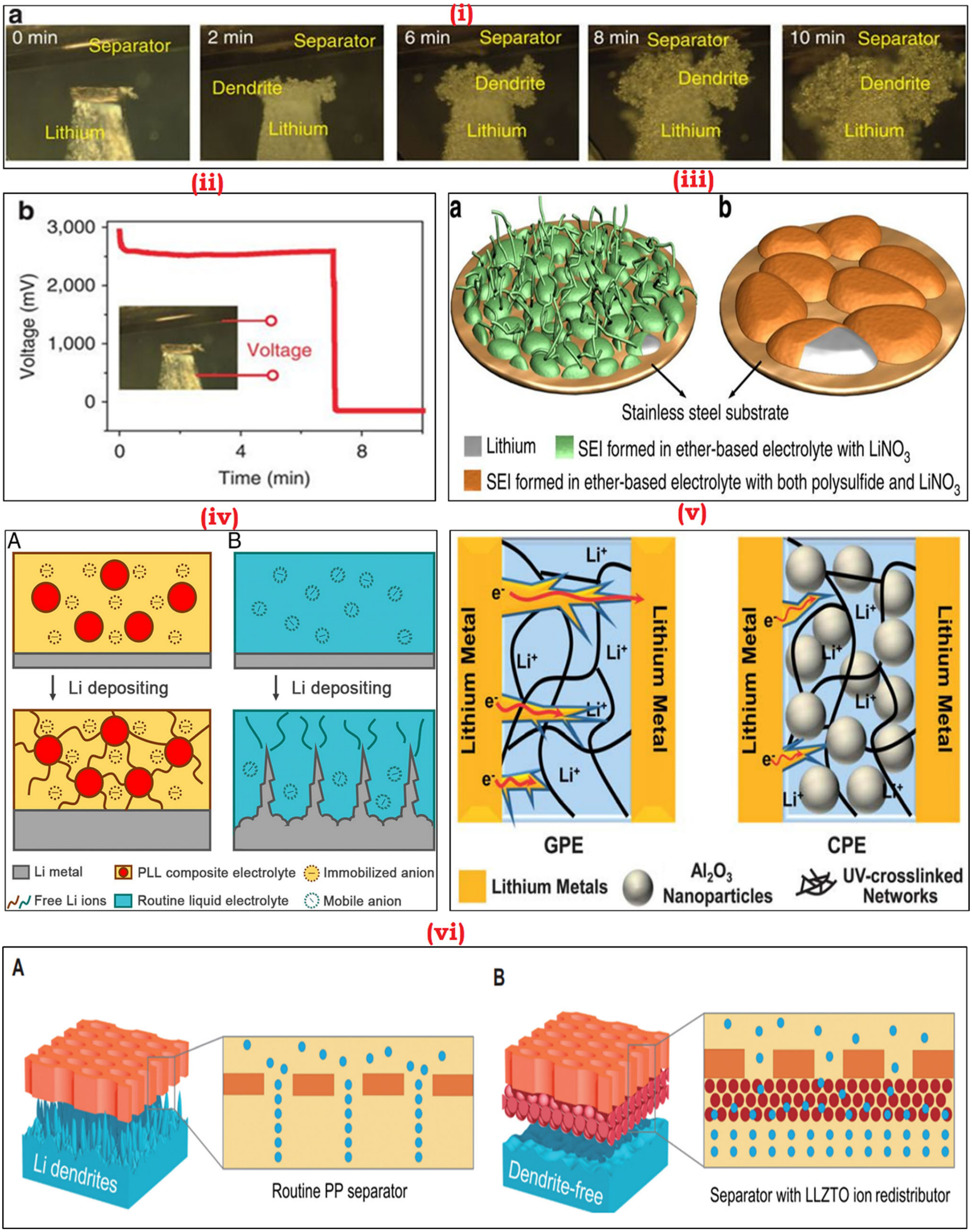
(i)
a
0 min
Separator
Lithium
2 min
Separator
Dendrite
Lithium
6 min
Separator
Dendrite
Lithium
8 min
Separator
Dendrite
Lithium
10 min
Separator
Dendrite
Lithium
(ii)
b
3,000
2,000
1,000
0
Voltage (mV)
Voltage
0
4
8
Time (min)
(iii)
a
b
Stainless steel substrate
Lithium
SEI formed in ether-based electrolyte with LiNO3
SEI formed in ether-based electrolyte with both polysulfide and LiNO3
(iv)
A
B
Li depositing
Li depositing
Li metal
PLL composite electrolyte
Immobilized anion
Free Li ions
Routine liquid electrolyte
Mobile anion
(v)
Lithium Metal
Lithium Metal
Li+
e-
Li+
Li+
e-
Li+
e-
Li+
GPE
Lithium Metal
Lithium Metal
e-
Li+
Li+
Li+
e-
Li+
Li+
CPE
Lithium Metals
Al2O3 Nanoparticles
UV-crosslinked Networks
(vi)
A
B
Li dendrites
Routine PP separator
Dendrite-free
Separator with LLZTO ion redistributor

Table 5 FMMEA for lithium-ion batteries. [Reprinted with permission from Ref. [64], © Elsevier 2015]

Battery component	Potential failure mode(s)	Potential failure mechanism(s)	Mechanism type	Observed effect	Potential failure causes	Likelihood of occurrence	Severity of occurrence	Ease of detection
Anode (active material)	Thickening of solid electrolyte interphase layer	Chemical reduction reaction and deposition	Wearout	Increased charge transfer resistance, reduction in capacity, reduction in power	Chemical side reactions between lithium, electrode, and solvent	High	Low	High
	Particle fracture	Mechanical stress	Overstress	Reduction in capacity, reductiin of power	Intercalation stress	Moderate	Low	Low
	Reduced electrode porosity	Mechanical degradation	Wearout	Increased diffusion resistance, reduction in capacity, reduction in power	Dimensional changes in electrode	Moderate	Low	Low
	Lithium plating and dendrite growth on anode surface	Chemical reaction	Wearout	Can cause short circuit if dendrites puncture separator	Charging the battery at low temperatures or high rates	Low	High	Low
Anode (current collector)	Free copper particles or copper plating	Chemical corrosion reaction and dissolution	Wearout	Increased resistance, reduction in power, reduction in current density	Overdischarge of the battery	Low	High	Low
Cathode (Active Material)	Thickening of solid electrolyte interphase layer	Chemical reduction reaction and deposition	Wearout	Increased charge transfer resistance, reduction in capacity, reduction in power	Chemical side reactions between lithium, electrode, and solvent	High	Low	High
	Particle fracture	Mechanical stress	Overstress	Reduction in capacity, reduction in power	Intercalation stress	Moderate	Low	Low
	Reduced electrode porosity	Mechanical degradation	Wearout	Increased diffusion resistance, reduction in capacity, reduction in power	Dimensional changes in electrode	Moderate	Low	Low
	Gas generation and bloating of cell casing	Thermally driven Electrode decomposition	Overstress	Reduction in capacity	Overcharge of the battery or short circuit	Low	High	Low
Cathode (current collector)	Pitting corrosion of aluminum	Chemical corrosion reaction	Wearout	Increased resistance, reduction in power, reduction in current density	Overcharge of the battery	Low	Moderate	Low

Table 5 continued

Battery component	Potential failure mode(s)	Potential failure mechanism(s)	Mechanism type	Observed effect	Potential failure causes	Likelihood of occurrence	Severity of occurrence	Ease of detection
Separator	Hole in separator	Mechanical damage	Overstress	High heat generation due to joule heating, bloating of cell casing, drastic voltage reduction	Dendrite formation, external crushing of cell	Low	High	Moderate
	Closing of separator pores	Thermally induced melting of Separator	Overstress	Inability to charge or discharge battery	High internal cell temperature	Low	High	High
Lithium ions	Reduction in lithium ions, thickening of solid electrolyte interphase layer	Electrolyte reduction and solid product formation	Wearout	Reduction in capacity	Chemical side reactions between lithium, electrodes, and solvent	High	Low	High
Electrolyte salt	Decrease in lithium salt concentration	Chemical reduction reaction and deposition	Wearout	Increased diffusion resistance	Chemical side reactions between lithium, electrodes, and solvent	Low	High	Low
Organic solvents	Gas generation and bloating of cell casing	Chemical decomposition of Solvent	Overstress	Increased diffusion resistance, and may lead to thermal runaway	High external temperature, overcharging of the cell	Low	High	Low
	Thickening of solid electrolyte interphase layer	Chemical reduction reaction and deposition	Wearout	Increased charge transfer resistance, reduction in capacity, reduction in power	Chemical side reactions between lithium, electrodes, and solvent	High	Low	High
Terminals	External corrosive path between positive and negative leads	Chemical corrosion reaction	Wearout	High heat generation due to joule heating, bloating of cell casing, drastic voltage reduction	Inadvertent shorting of the terminals	Low	High	Moderate
	Solder cracking	Thermal fatigue mechanical vibration fatigue	Wearout	Loss of conductivity between battery and host device	Circuit disconnect	Low	Moderate	High
Casing	Internal short circuit between anode and cathode	Mechanical stress	Overstress	High heat generation due to joule heating, bloating of cell casing, drastic voltage reduction	External load on cell	Low	High	Moderate

prepare high molecular weight copolymer. So, Kamigaito et al. [67] reported the preparation of PPME-b-PSt via a living radical polymerization technique.

Another important technique is the atom transfer radical polymerization (ATRP) technique. Holmberg et al. [68] investigated the atom transfer radical polymerization (ATRP) of styrene onto poly-(vinylidene fluoride)-*graft*-poly(vinylbenzyl chloride) (PVDF-*g*-PVBC) membranes. Also, the PS-grafted membrane shows improved conductivity. Recently, Grewal et al. [69] have prepared the cross-linked network polymer electrolyte membrane composed of bifunctional PEG, PEMP, and LiTFSI using a facile one-pot reaction and the concept of "click chemistry." The prepared polymer electrolyte exhibits high ionic conductivity and improved mechanical property. Another important technique is in situ polymerization technique and is preferred as it reduces the contact impedance [70]. The selection of initiators is important as it may lead to the formation of the undesirable solid–electrolyte interface (SEI) [71]. Recently, Huang et al. [72] have demonstrated the preparation of the PTHF-based polymer electrolyte (PTSPE) by in situ polymerization of THF using BF_3 as initiator. The present SPE demonstrates improved interfacial stability and contact features.

Recently, Nair et al. [73] have highlighted the advantage of thermal and UV-induced polymerization technologies (simple and eco-friendly) for the preparation of polymer electrolytes [74–76]. Another important technique is cationic ring-opening polymerization (CROP) and is effective in forming the novel SPE based on target-specific polymers, also better for developing industrial polymer (polytetrahydrofurans, polysiloxanes, etc.). In CROP, both initiating and propagating species are positively charged intermediate and CROP is fast and no solvent is required. The CROP can be thermally induced or UV-irradiated [77–79]. Zaheer et al. [80] reported the preparation of the comb-like PLA/PEG copolymer-based SPE via photoinitiated radical polymerization. The obtained SPE shows high ionic conductivity and good interfacial contacts with electrodes.

Modification strategies in polymer electrolyte

As it is well known that the low glass transition temperature is the key behind the increased ionic transport in the case of polymer electrolytes. Along with this, some other factors need to be considered such as low crystallinity, the suppression of crystallization, and the promotion of polymer segmental motions. So, various modification strategies have been adopted to achieve balanced properties. Some recent attempt using a different class of electrolyte has been discussed in detail [81, 82]. Figure 9 shows the important types of polymer electrolytes that are recently gaining the attention of the energy community for application in ASSBs and their commercial aspects.

Ceramic polymer electrolyte

Ceramic polymer electrolyte is of great interest due to the ability to provide improved conductivity as compared to solid polymer electrolyte. The addition of nanoparticles enhances the conductivity and thermal and mechanical properties. The Lewis-acid-based interaction of the surface group of nanofiller with a polymer and salt enhances the ion transport phenomenon. The surface group of nanofiller also restricts the migration of anion. The addition of nanofiller enhances the segmental motion of the polymer chain [83]. Another advantage with

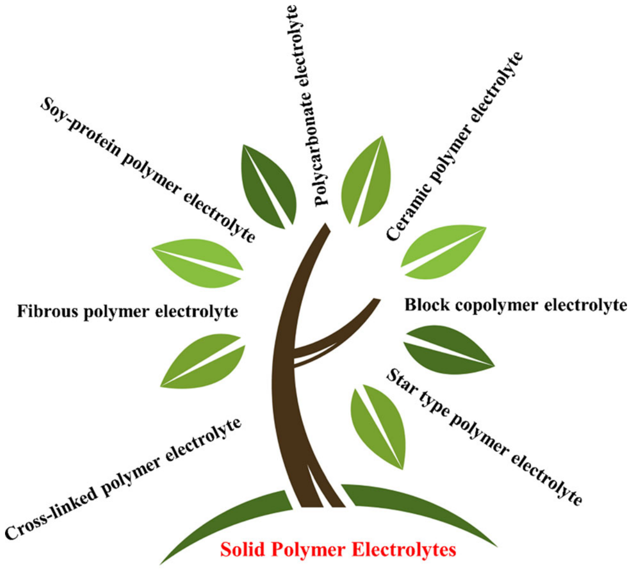

Figure 9 Important types of solid polymer electrolytes.

nanoparticle addition is that the nanoparticle disrupts the polymer chain arrangement and indicates the enhancement of more free volume or amorphous content for ion migration [84].

Block copolymer electrolyte

An alternative approach to tailor the architecture of the SPE is the development of the block copolymer (BCP) electrolyte. In general, BCP comprises covalently bound polymers with characteristic properties and overall improved properties are obtained as compared to the individual polymer. One unique feature is that BCP enables us to synthesize PE with good conduction pathways (from any electron-rich group in polymer, e.g., PEO, PVC, polyethylene oxide, etc.) and better mechanical property (from block copolymer; e.g., siloxanes, PS) [85–87]. The ionic conductivity and the mechanical property of BCP are influenced by the complexation of salt with solvating blocks of BCP [88].

Polycarbonate polymer electrolyte

Polycarbonates (PC)-based SPE are new emerging candidates that grabbed the attention of researchers due to their unique feature amorphous nature, chain segmental flexibility, and high dielectric constant. These properties result in improved thermal stability, high voltage stability window, and cation transference number. For high conductivity and flexibility, most deserving PC are made up of aliphatic backbones and few are poly (vinylene carbonate) (PVC), poly(propylene carbonate) (PPC), poly(trimethylene carbonate) (PTMC), and poly(ethylene carbonate) (PEC) [89, 90].

Star-type polymer electrolyte

The enhanced polymer structure is the star polymers and has improved physical and topological properties. The outer spheres of arms in star polymer enhance the ion mobility and the ionic conductivity. The star polymer possesses improved properties as compared to a linear polymer. The connection of covalent bonds between the core and arms enhances the stability of the external environment [91]. The star polymer electrolyte having various branching points disrupts the polymer crystallization and enhances the free volume for segmental motion. Along with this, it allows more salt dissociation and some rigid framework may be introduced to achieve mechanical stability [92, 93].

Fibrous polymer membrane-based polymer electrolyte

Fibrous polymer membrane-based polymer electrolyte shows improved performance as compared to the traditional polymer electrolytes. The high surface area of nanofiber effectively enhances the ion conduction by creating the continuous ion conduction pathways in the polymer matrix [94]. In fiber, the energy barrier of particle–particle junctions is low as compared to nanofiller that will enhance ion transport. Along with this, the 1D fiber may disrupt the crystallinity of polymer and promotes the faster segmental motion associated with fast ion mobility. One unique advantage is that better interfacial contact between polymer and fiber results in improved electrochemical stability [95–97].

Cross-linked polymer electrolyte

Polymer structure plays an important role to influence the transport properties of the polymer electrolyte. So, cross-linking of polymer electrolytes is an attractive strategy to prepare new polymer electrolytes. The cross-linking approach enhances dimensional stability and dynamic storage modulus [98, 99]. The chemical cross-linking of polymer needs to be done in such a way that balanced ionic conductivity and mechanical strength may be achieved. The cross-linker prevents polymer crystallization and facilitates faster segmental mobility [100].

Soy protein-based polymer electrolyte

These are newly advanced polymer electrolytes that show enhanced properties as compared to the existing polymer electrolytes. The soy protein (SP) is denatured before use. The denaturation process results in unfolding the chain, and the negative acid group present in the SP results in Li-ion adsorption. Here, the polymer chains are surrounded by the PEO. The electron-rich site of polymer absorbs Li-ions as well as interacts with the ammonium group having a positive charge. It disrupts the crystalline arrangement of PEO, and an amorphous phase is formed [101].

Comparison of characteristics properties of salt

In principle, electron-rich polymer always has insulating nature, and it becomes conducting due to the dissociation of salt in it. Therefore, salt can be considered as one of the important additives in the polymer electrolyte system who directly influences the overall ion dynamics. There are some of the important parameters that are used as a basis for the selection of salt for the synthesis of new polymer electrolyte system. The ion dynamics are linked with molecular weight, ion conductivity, donor number, thermal stability, toxicity, anion size, anion mobility, dissociation constant, and lattice energy of salt. Figure 10 shows the structures of some of the dominating salts in the R&D sector, and their key properties are compared [101–104]. Another foremost important parameter is the conductivity of the salt, and it may be noticed from Fig. 10 that the conductivity of the salt is influenced by the anion size [105–109]. Another important term for salt is Gutmann donor number (DN). It is a quantitative measure for the tendency to

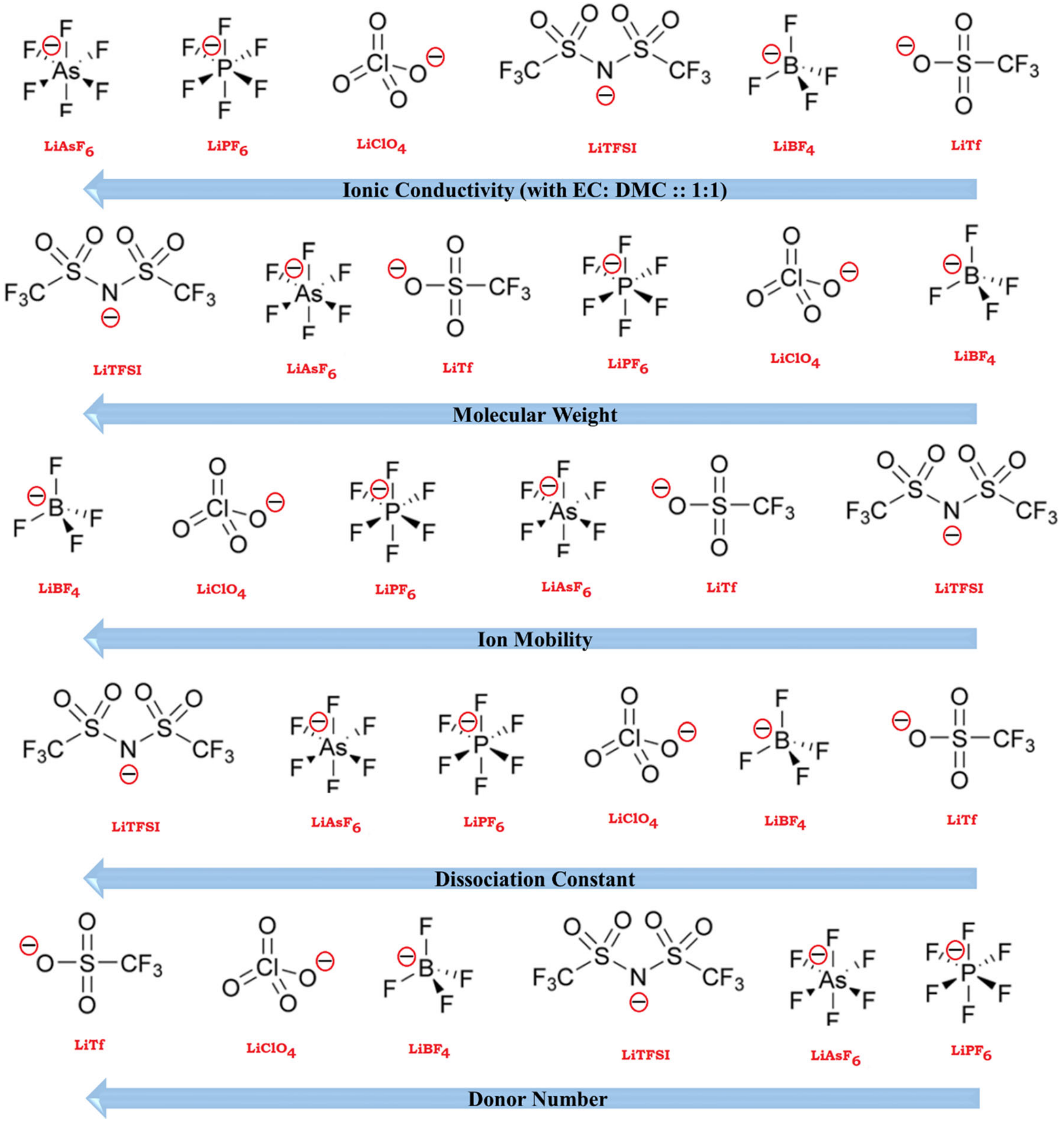

Figure 10 Comparison of different characteristics of lithium salt.

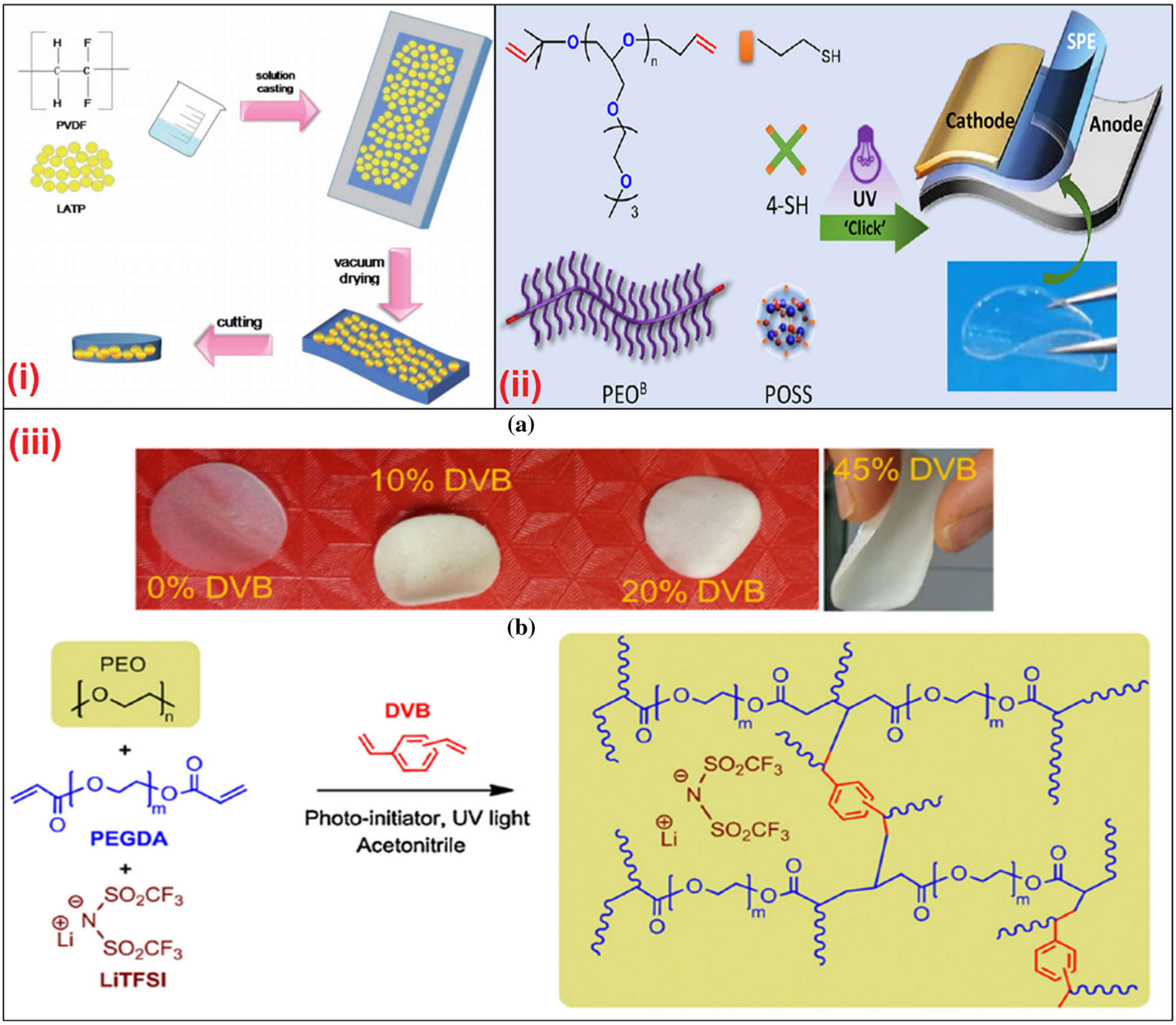

Figure 11 **i** Schematic presentation of the preparation of the composite polymer electrolyte (Reproduced with permission from Ref. [84] © AAAS 2018). **ii** Schematic Illustration of the End-Functionalized PEOB, Cross-Linkers, and the Resulting SPEs (The photograph represents the typical SPE film.), (Reproduced with permission from Ref. [113] © American Chemical Society 2018). **iii** (a) Photograph of the as-prepared self-standing SPEs with different DVB concentration and (b) schematic of UV-induced preparation of semi-interpenetrated network based on PEO matrix (Reproduced with permission from Ref. [114] © Elsevier 2016).

donate electron pairs to acceptors (cation). For all lithium salts, DN is close enough [110–112]

Experimental procedure and methodology

The solution cast technique is a simple and cost-effective technique. Figure 11i shows the flowchart of the solution cast technique. Here, first of all, the polymer is mixed in a solvent of high dielectric constant and stirred till a homogenous polymer solution is obtained. After that, stoichiometric ratio of salt is added in the polymer solution and again stirred to obtain a homogenous solution. After that, polymer solution is cast in petri dishes (Glass/PP/Teflon) and kept in a vacuum oven for complete removal of the solvent. In the case of ceramic-polymer electrolyte, the nanoparticle is added after sonication, in the polymer salt solution followed by casting [84]. Then, the film is peeled off from the petri dish. Cross-linking is an effective approach, i.e. photochemical cross-linking, to improve the properties of a polymer. Recently, Wei et al. [113] have reported the preparation of non-crystalline poly (ethylene oxide) (PEO) with highly mobile EO branches (PEOB) and end functionalities. The three advantages with this approach are: (1) there is suppression of the crystallinity of the polymer, (2) EO oligomers improve salt solubility, and EO brushes enhance cation migration, and (3) end functionality of PEO acts as cross-linker and increases the mechanical strength (Fig. 11ii–iii).

Youcef et al. [114] prepared the semi-interpenetrated cross-linked polymer electrolyte by UV-induced photoinitiated polymerization of PEGDA and DVB mixed with PEO/LiTFSI. Here, fits of all polymer and salt were dissolved in an appropriate solvent followed by stirring. Then, the homogenous solution is poured in a petri dish and irradiated (about 1 h) under UV light (365 nm) which results in excitation of n–p* transition in 2-hydroxy-2-methylpropiophenone [115]. This results in the free-standing polymer electrolytes.

Another important and new polymer electrolyte is soy protein-based polymer electrolyte. The detailed preparation of SP-based PE is in the coming section. SPI is a mixture of soy proteins, which comprises glycinin and β-conglycinin. Figure 12 shows the schematic illustration and SEM and TEM images of SP and denatured SP. For the preparation of the soy protein isolate (SPI)-based polymer electrolytes. First of all, the SP is denatured in a mixed solvent of acetic acid and water (80:20) along with stirring at 95 °C for 1 h to get a semitransparent yellowish solution. The denaturation of the SP reduces its particle size, and protein structure–activity is increased. Then appropriate salt is added in the SP solution followed by the addition of polymer. Then the final solution is cast on the aluminum film, and a desirable film is obtained [116, 117].

The subunits in the SPI are associated via hydrophobic and hydrogen bonding as shown in Fig. 12a. So, denaturation of the SPI is done to enhance the protein activity owing to the presence of more functional groups on the protein surface. This process disrupts the bonding interactions between the secondary and tertiary structure, and protein chain unfolds [101]. Figure 13b shows the adsorption of cation on the negative sites on SPI. Now, on the addition of PEO, the protein chains have a higher tendency to surround themselves by PEO chains. The presence of ether group in PEO has two possible

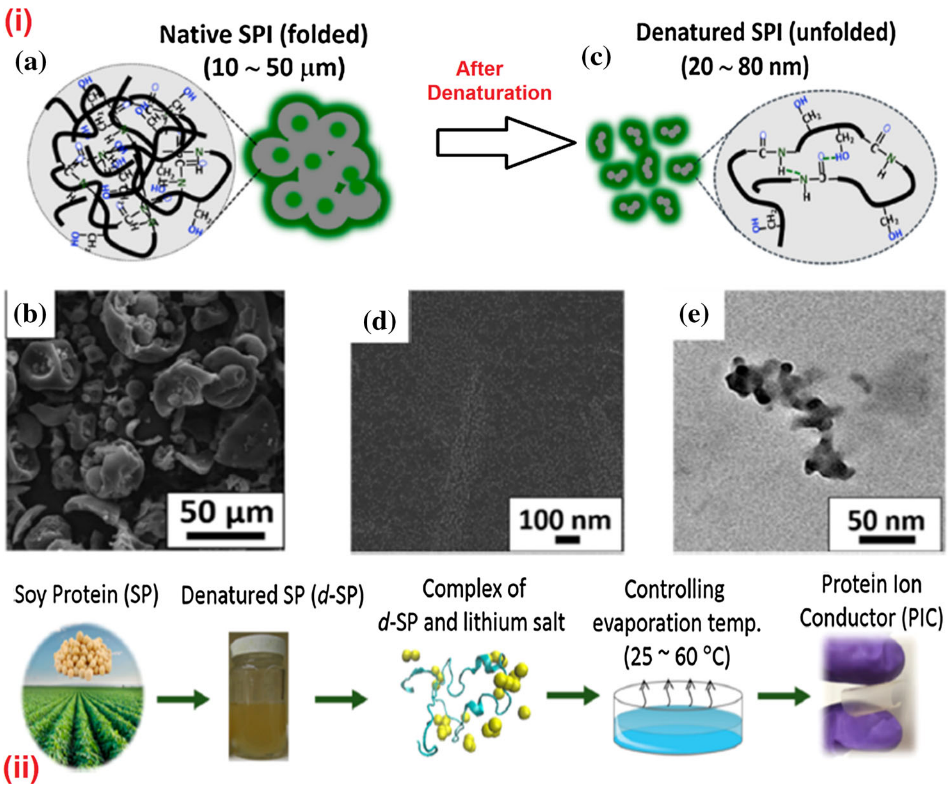

Figure 12 (i) Denaturation of soy protein. (a) Schematic illustration of pristine SPI powder, (b) SEM image of pristine SPI powder, (c) schematic illustration of denatured SPI particles, and (d) SEM and (e) TEM images of denatured SPI particles (Reproduced with permission from Ref. [116] © American Chemical Society 2016). (ii) The fabrication process of protein-based ion conductor (Reproduced with permission from Ref. [117] © American Chemical Society 2016).

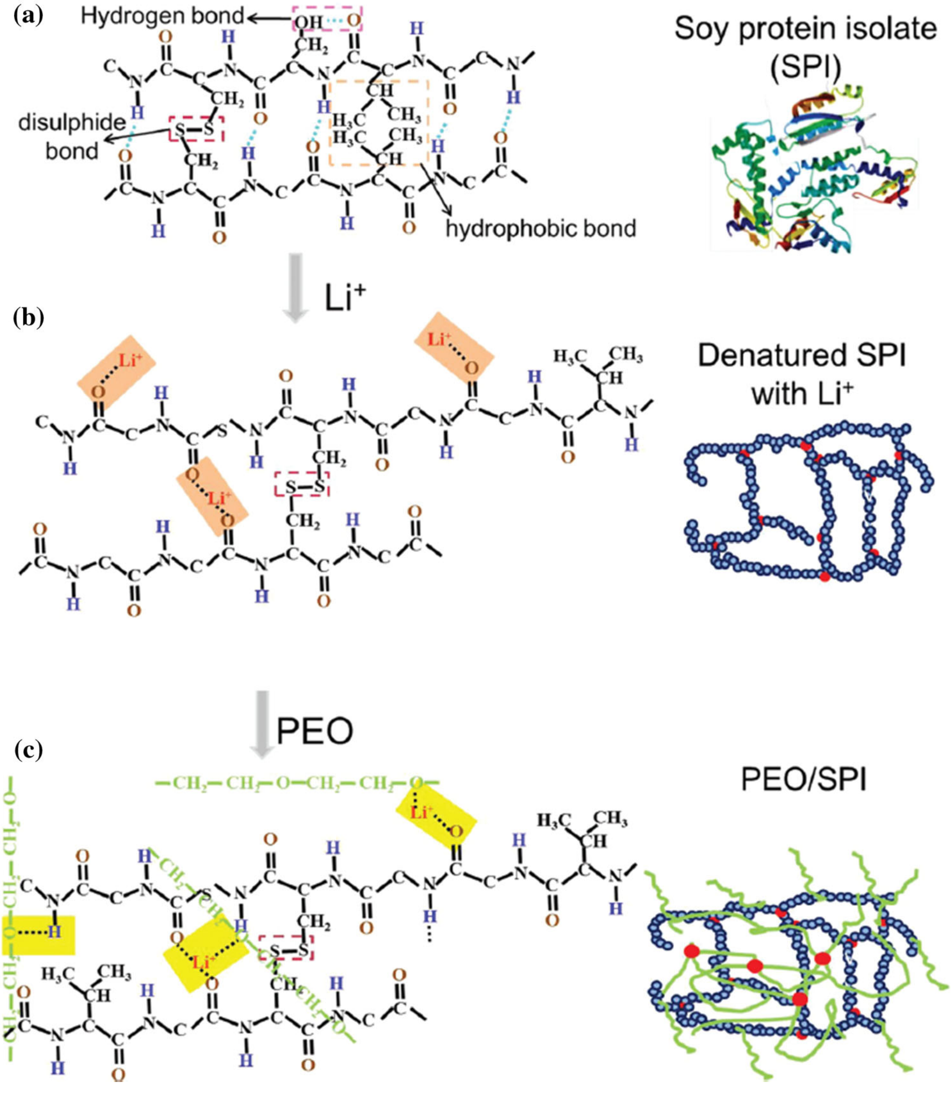

Figure 13 Structure of **a** received SPI, **b** denatured SPI, and **c** PEO/SPI (Reproduced with permission from Ref. [101] © American Chemical Society 2012).

interactions: (1) with cation and (2) with positive ammonium group. The simultaneous presence of both disrupts the polymer chain structure, and amorphous phase is obtained (Fig. 13c).

Another important technique is polymerization-induced self-assembly (PISA) to prepare SPE. One advantage is that no volatile organic solvent is used in this method. Recently, Yuan et al. [118] have prepared the SPE using via polymerization-induced self-assembly method. Here, the carbonate-terminated poly(ethylene glycol) (CH_3O-PEG-IC), poly(ethylene glycol)-block-polystyrene (PEG-b-PS) block copolymer nanoparticles containing a conductive PEG corona, fumed SiO_2 and LiTFSI salt are used. Figure 14a shows the synthesization of PEG containing an isopropyl carbonate terminal (CH_3O-PEG-IC). Figure 14b shows the schematic of the SPE in detail. In this process, the carbonate group in CH_3O-PEG-IC increases salt dissociation, while PEG enhances the segmental motion and ion mobility.

The star polymer electrolyte is synthesized via cation template-assisted cyclo-polymerization. The star polymer comprises cross-linked cores containing pseudo-crown ether cavities and PEO arms. The unique feature here is that the ether cavities coordinate with the cation and promotes its migration. First of all, the star polymer is synthesized by the cation template-assisted atom transfer radical cyclo-polymerization. The details of the process are shown in Fig. 15 [119]. For the preparation of the polymer electrolyte, the star polymer is dissolved appropriate salt in a suitable solvent.

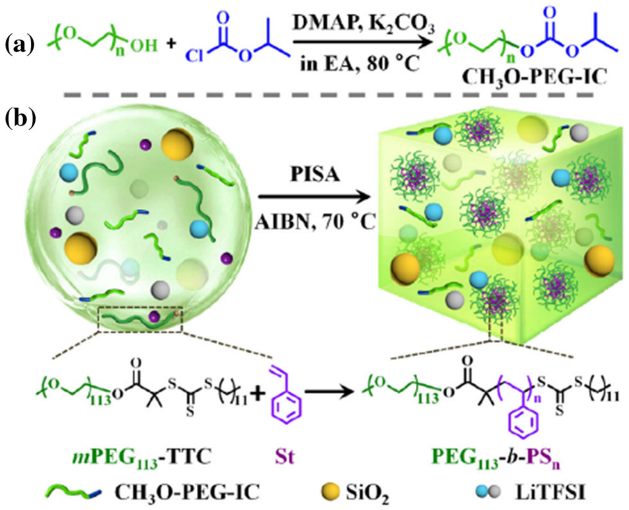

Figure 14 Synthesis of CH$_3$O-PEG-IC (**a**) and PISA-SPEs (**b**) (Reproduced with permission from Ref. [118] © Elsevier 2019).

Electrode preparation and cell assembly

The first step involves the preparation of the electrodes for the battery. The active material for the cathode is metal oxide materials (LiCoO$_2$, LiFePO$_4$, LiCoMnO$_2$, Li$_2$FeSiO$_4$, etc.), and for anode most feasible candidate is graphite. The particle size of the active material is kept minimum for better interfacial processes owing to the availability of maximum surface area. The detailed full coin cell fabrication is given by Murray et al. 2019 [120]. Two important cell construction designs are shown in Fig. 16.

The active electrode materials slurry is coated on the metallic foils (Cu foil for the anode, and Al foil for cathode). Here, metallic foils act as current collectors. For positive electrode slurry preparation, the active material is mixed with poly (vinylidene fluoride) (PVdF) and carbon black (80:10:10 by weight) into N-methyl pyrrolidone (NMP) and the obtained slurry is coated on the aluminum foil followed by drying at high temperature (~ 100–150 °C) for 12–20 h. The negative electrode materials graphite is mixed with poly (vinylidene fluoride) (PVdF) and carbon black (80:10:10 by weight) into N-methyl pyrrolidone (NMP), and the obtained slurry is coated on the copper foil followed by drying at high temperature (~ 100–150 °C) for 12–20 h. Then, the lithium-ion cell is assembled in the glove box by sandwiching the solid polymer electrolyte between two electrodes. A detailed cell fabrication process for the prismatic and

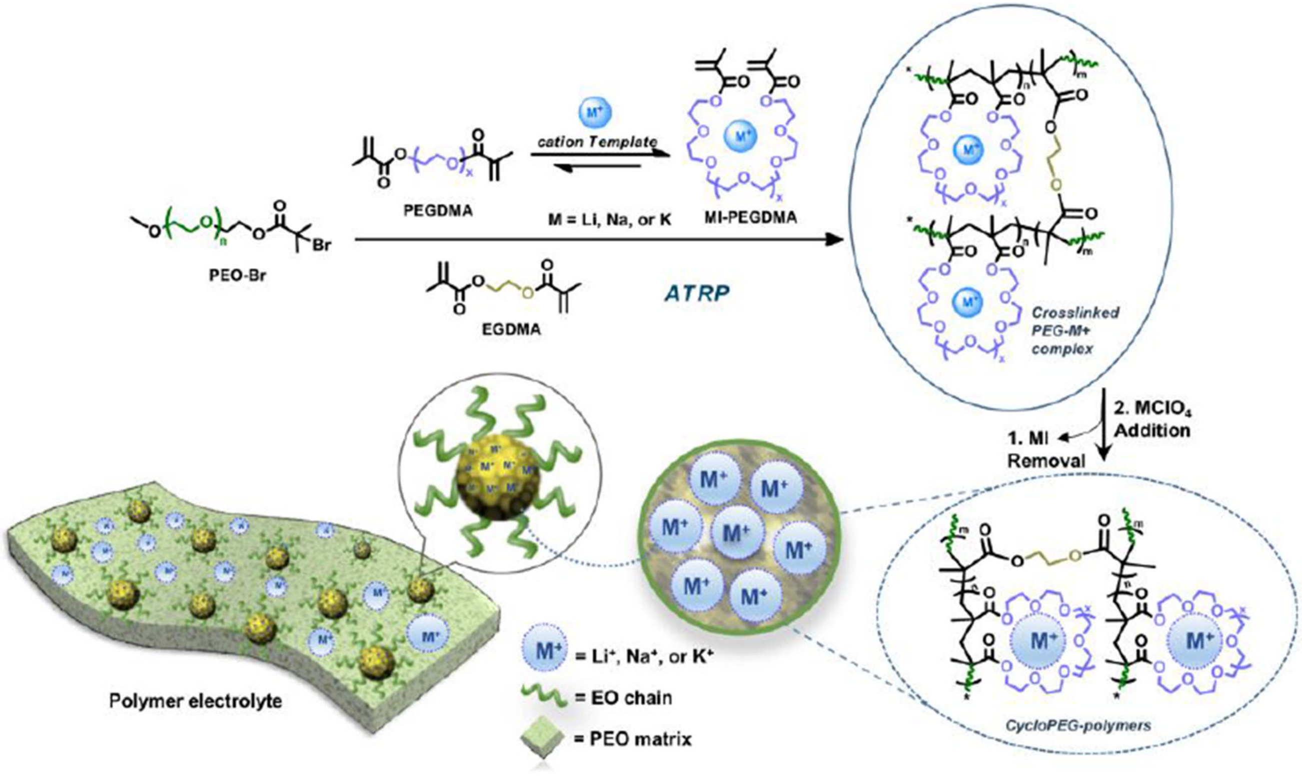

Figure 15 Schematic illustration on the star polymer with pseudo-crown ether cavities and PEO arms (Reproduced with permission from Ref. [119] © Elsevier 2019).

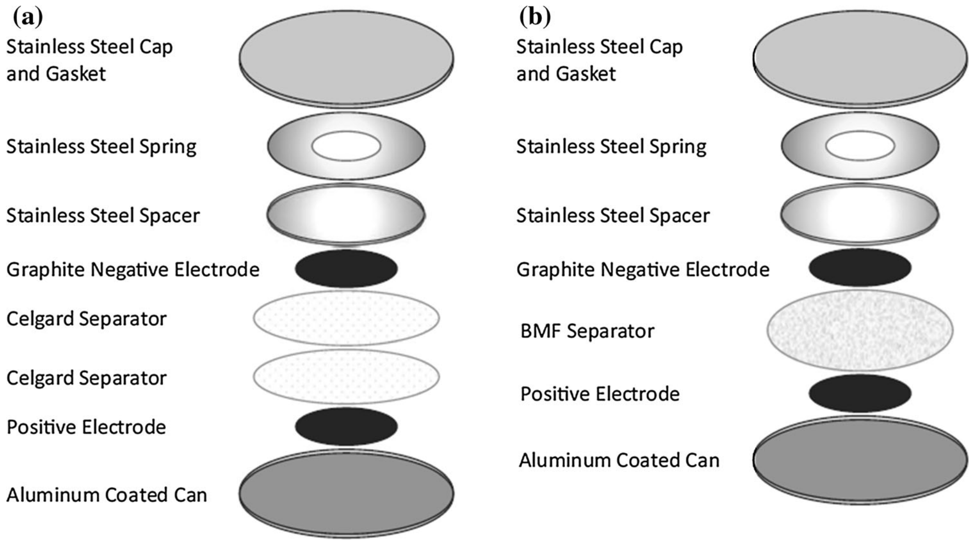

Figure 16 Diagram of full cell with **a** two Celgard separators or **b** One BMF Separator (Reproduced with permission from Ref. [120] © The Electrochemical Society 2019).

cylindrical cells is shown in Fig. 17 [https://www.mpoweruk.com/battery_manufacturing.htm].

Characterization techniques

Some of the important characterization techniques are summarized by classifying them into the imaging and non-imaging techniques as shown in Table 6 [121].

Recent updates in solid polymer electrolytes-based batteries

Ceramic (LATP/LLTO/LLZTO/Li_3PS_4)-based polymer electrolyte

The addition of nanofiller in the polymer matrix is a striking approach to enhance the electrochemical properties by suppressing the crystalline part. The large surface area associated with the nanofiller, strong Lewis acid–base interaction, and formation of conducting pathways results in the faster ion migration owing to better salt dissociation.

Nowadays, the addition of active fillers is gaining interest to further improve the electrical and electrochemical stability properties. So, to understand the role of the following section highlights some of the interesting results. One major drawback of ceramic-based polymer electrolyte system that hinders the electrochemical performance is dendrite growth. Dendrite growth is one of the dominating factors that decides the battery life and is the result of poor interfacial contact. So, to tackle the said issues a new assembly (polymer (I)/ceramic (II)/polymer (I) sandwich electrolyte; PCPSE) was demonstrated. The role of the middle part, i.e., ceramic (II) is to eliminate the electrolyte decomposition by blocking the anion transportation, while the role of polymer (I) is to prevent dendrite growth formation that improves the operating range of battery [122].

A remarkable approach has been suggested by the J. B. Goodenough and group that explores a new structure, i.e. sandwich structure (polymer/ceramic/polymer electrolyte), and shows the improved properties [123]. Recently, Li et al. [124] have proposed an SPE with sandwiched structure (PVDF/LLTO-PEO/PVDF) and shows superior electrochemical properties.

The main focus of the investigation was to resolve the issue of the low ionic conductivity and chemical instability of Ti_4^+ ions in LLTO against lithium metal. The LLTO nanowire (average diameter $\sim$ 290 nm) filled PEO provides high ionic conductivity, while the PVDF layer suppresses the dendrite growth. The 10 wt% LLTO-based system (interlayer-II) shows the highest ionic conductivity of 2.1×10^{-4} S cm^{-1} (@RT). Figure 18a, b shows the sandwiched PVDF fibers (average diameter = 0.7 µm.). The thermal stability of the film was about 343 °C. The ionic conductivity possessed by the sandwiched structure is $\sim 3.01 \times 10^{-3}$ S cm^{-1} and is comparable to gel electrolytes and the lowest activation energy. The voltage stability window was close to 5 V. The enhancement of the voltage stability window was suggested due to the prevention of PEO

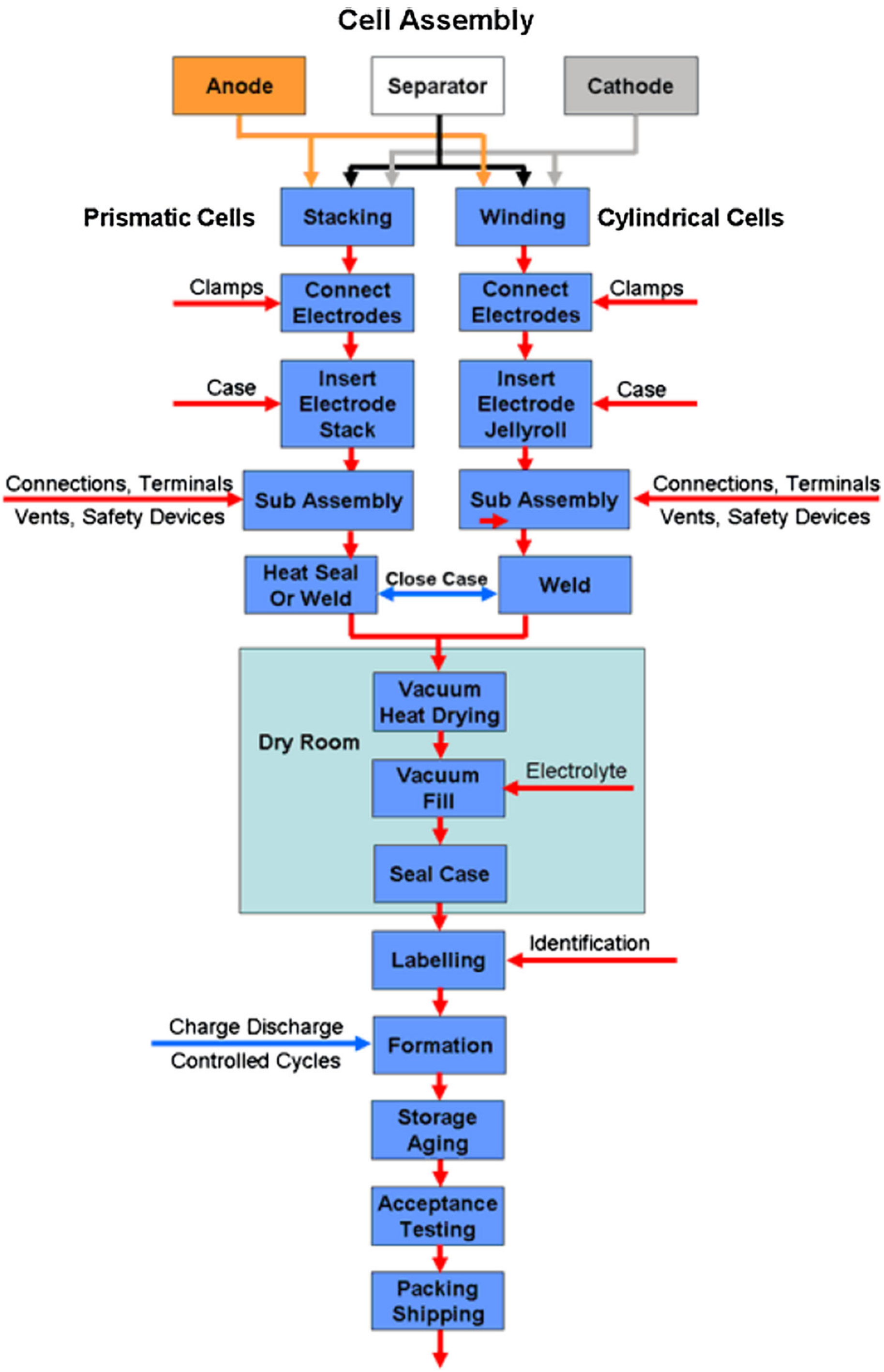

Figure 17 Assembly process for prismatic and cylindrical cells.

decomposition by PVDF layer and LLTO nanowire. Another key point was that the functional sites of the LLTO NW increase the polymer chain stability. The ion transference number shows the trend, 0.54 [PEO (8)] < 0.67 [PEO(8) + 15% LLTO NWs; Interlayer-III] and 0.70 [PVDF/Interlayer-III/PVDF; SWE-III]. The enhancement was attributed to the anion trapping ability of LLTO NW. The charge–discharge was performed of the cell $LiCoO_2$/SWEs-III/Li in the voltage range 2.7–4.2 V. The discharge capacity is as 144 mAh g^{-1} (@ 1 C), 132 mAh g^{-1} (@ 2 C), 122 mAh g^{-1} (@ 3 C), 110 mAh g^{-1} (@ 4 C) and 98 mAh g^{-1} (@ 5 C). The cyclic performance was tested at a 2 C rate and shows specific capacity

Table 6 Selected separator characterization techniques with examples for extracted parameters (Reprinted with permission from Ref. [121], © Springer Nature 2019)

	Type of analysis	Parameters extracted
Imaging techniques	Tomographic analysis	Morphology Porosity Tortuosity Pore dimensions
	FIB-SEM tomography	Porosity Tortuosity Pore dimensions
Non-imaging techniques	*Electrochemical analysis*	
	Linear sweep voltammetry and cyclic voltammetry	Electrochemical stability
	Electrochemical impedance spectroscopy	Mac Mullin number via bulk electrolyte conductivity σ and effective electrolyte conductivity σ_{sep} Transport parameters (diffusion coefficient, ion mobility, viscosity)
	Potentiostatic polarization combined with electrochemical impedance spectroscopy	Lithium-ion transference number according to Bruce–Vincent method
	Spectroscopic and diffractive methods (OR may be considered basic characterizations)	
	NMR	Transport properties Diffusion coefficients Conductivity Transference number
	X-ray diffraction	Structural composition Degree of crystallinity Crystallite size/interchain separation
	Thermomechanical analysis	
	Compressive loading	Effective membrane moduli Young's modulus Flow stress
	Thermo-gravimetric analysis and differential scanning calorimetry	Brittleness and stability Ductile-to-brittle transition temperature Melting temperature Glass transition temperature Crystallinity

retention above 91.8% after 100 cycles. Figure 18c, d displays the demonstration of glowing LED using the fabricated cell.

As in the polymer electrolytes, both cation and anion are active species contributing to conduction. This develops the concentration polarization that slows down the cation migration. The approach to bind or trap the anion with polymer chain is interesting to achieve the single-ion conduction. By considering this strategy to enhance the cation migration, Lian et al. [125] reported the preparation of the oxalate-chelated borate-grafted PVFM-based single-ion conductor polymer (SCP) membranes. XRD diffractograms evidenced the decrease in crystallinity, and TGA displays improved thermal stability. The stress–strain curve indicates the maximum tensile strength of 34 MPa for SCP-1.0 and is attributed to the cross-link formation between oxalate-chelated borate structure and PVFM domains. The temperature-dependent ionic conductivity follows the VTF behavior and lies in the range 10^{-6}–10^{-5} S cm^{-1}. Although it was lower than the dual ion-conducting system. The authors predicted the dependence of the ionic conductivity on the number of mobile charge carriers (dominates at high T) and the segmental motion (dominates at low T). The voltage stability window of all systems was more than 5 V versus Li/Li^{+}. The charging–discharging of the fabricated cell was

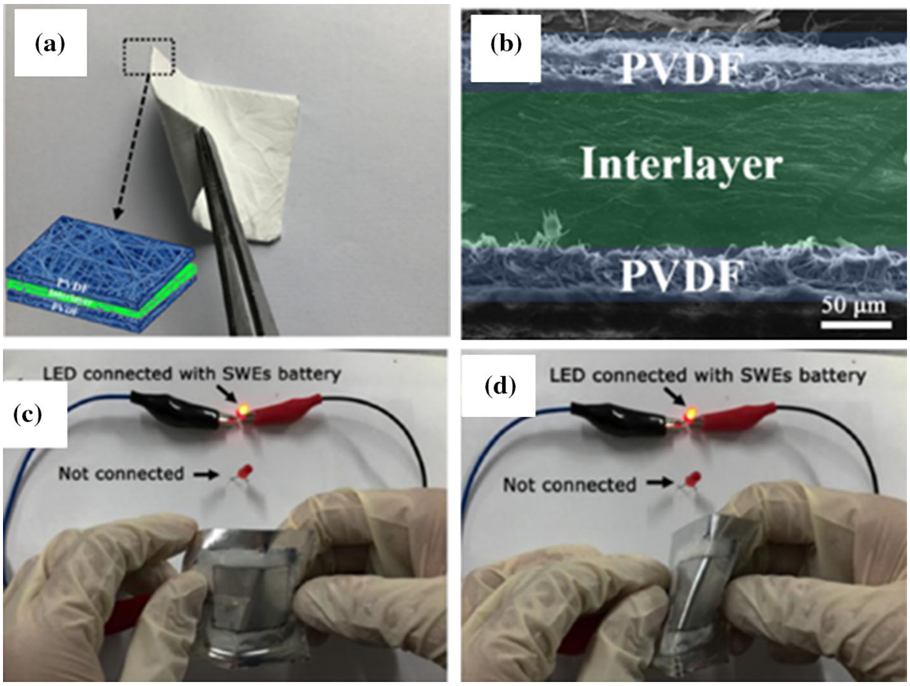

Figure 18 **a** Sandwich structure composite electrolytes and 3D model diagram. **b** SEM image demonstrating cross-section of the sandwich structure composite electrolytes, **c**–**d** Illustration of flexible SWEs full battery for lighting LED under different deformation at room temperature (Reproduced with permission from Ref. [124] © Elsevier 2018).

observed in the range of 2.5–4.25 V. The initial discharge capacity was 139 mAh g^{-1} with Coulombic efficiency of about 82.7% which decreases to 137 mAh g^{-1} with Coulombic efficiency of about 99.7% after 20 cycles. It indicates the use of the present system for safe Li-ion batteries due to good electrochemical reversibility.

As it is well known that the addition of nanofiller enhances the electrical properties of the polymer electrolytes and is owing to the high aspect ratio. But, one serious drawback is the agglomeration at high filler content that lowers the ionic conductivity. So, it becomes important to resolve the issue of the nanofiller aggregation to achieve the desired conductivity via the percolation path for ion migration and one alternative is the development of nanofiller having percolated structure. Recently, Bae et al. [126] have developed a flexible composite polymer electrolyte by a novel strategy using the 3D nanostructured hydrogel (LLTO) frameworks as nanofiller. The effect of PVA addition on the LLTO network was investigated further. FESEM analysis evidenced the formation of interconnected percolation branches. The ionic conductivity was 8.8×10^{-5} S cm^{-1} (@ 25 °C) and increased to 1.5×10^{-4} S cm^{-1} (@ 30 °C) for 3.0 g PVA. The thermal stability was about 400 °C. The voltage stability window was larger for the LLTO-based CPE, i.e. 4.5 V and is higher than of PEO (3.9 V). It is important to note that the conductivity with the LLTO framework was higher than the active (LLTO particles at 10 wt%; 1.9×10^{-5} S cm^{-1} (@ 25 °C) and passive (SiO_2 nanofiller at 15 wt%; 5×10^{-6} S cm^{-1} (@ 25 °C) and is attributed to the pre-percolating structure of LLTO. The increase in conductivity is attributed to the formation of continuous conducting paths for the LLTO framework and a 3D interconnected structure. Also, the LLTO framework provides vacant sites for Li migration and it results in continuous ion migration via hopping, proving hence the enhanced conductivity.

As it is well known that the dispersion of nanofiller is a crucial approach to enhance conductivity by reducing the reorganization tendency of the polymer china and suppressing the crystalline content as well as an increase in free volume. Two types of nanofiller are mostly used: (i) active ($Li_{1.4}Al_{0.4}Ge_{1.7}(PO_4)_3$; LAGP), $Li_{0.33}La_{0.557}TiO_3$; LLTO) and $Li_{1.3}Al_{0.3}Ti_{1.7}(PO_4)_3$; LATP, etc.) and (ii) passive (TiO_2, ZrO_2, SiO_2, $BaTiO_3$, etc.). Former one acts as a source of charge carriers, while latter one indirectly supports the ion migration [127–129].

One point kept to be in mind is that nanofiller dispersion must be uniform to effectively enhance the electrical and mechanical properties. Nanofiller dispersion affects the interactions between polymer—salt, polymer—nanofiller and salt—nanofiller. The most common method is the physically mixing of the nanofiller, but it results in the agglomeration and reduces the polymer—nanofiller interaction. To obtain the uniform dispersion of nanofiller, a new approach "in situ synthesis of Li_3PS_4 nanoparticles within PEO matrix" was reported by Chen et al. [130]. XRD analysis indicates the destruction of the crystalline nature of the PEO and the amorphous region is enhanced.

Homma et al. [131] reported that the β-type PS_4 creates migration tunnels for Li-ion in the Li_3PS_4 particles and provides a conductive path. The nanoparticle diameter was 400–700 nm as obtained by FESEM and exhibits the electrical conductivity 4.03×10^{-4} S cm^{-1} ($E_a = 120.4$ kJ/mol). The prepared films were semitransparent, flexible and 100–150 μm thickness. Further, the comparatively ionic conductivity @ 60 °C was higher for the in situ prepared system (8.01×10^{-4} S cm^{-1}) than prepared by the mechanical-mixing method (6.98×10^{-4} S cm^{-1}). This corresponds to the highest ionic conductivity and attributed to the plasticizer role played by the Li_3PS_4 that increases free volume and an amorphous phase. It may be noted that conductivity increase was more for the in situ prepared system due to a better distribution of Li_3PS_4 nanoparticles which increase the effective surface area of nanoparticle in the polymer matrix. The Li-ion transference number was highest for the in situ prepared system, i.e. 0.33, and is higher than the pure PEO (0.14) and the electrolyte prepared by the mechanical-mixing method (0.28). This increase was attributed to the proper distribution of the sulfhydryl groups that promote the interaction between TFSI and Li_3PS_4, and only cation remains active species. The voltage stability window as obtained by LSV was 5.1 V and is superior to the PEO (4.6 V) and the mechanical-mixing prepared electrolyte (4.9 V). Then, the applicability of hybrid polymer electrolyte (PEO-2% vol Li_3PS_4) was checked by fabricating the Li-ion battery. The initial charge–discharge capacity is as given (@ 60 °C), 153 mAh g^{-1} (@ 0.1 C), 143 mAh g^{-1} (@ 0.2 C), 139 mAh g^{-1} (@ 0.5 C) and 127 mAh g^{-1} (@ 1 C). Even after 100 cycles, the discharge capacity was 125 mAh g^{-1} (86.1% of initial capacity), while for pure PEO only 58.9% capacity was retained (Fig. 19a–d). Further at 0.5 C, the cycling capability was performed and the first discharge capacity was 133 mAh g^{-1} and after the 325th cycle was 116 mAh g^{-1} with 80.9% capacity retention. The stress–strain curve analysis displayed the reliable/improved properties for the in situ prepared hybrid electrolyte as follows, Young's modulus; 12.46 MPa, tensile strength; 2.73 MPa and elongation-at-break; 1897%. In conclusion, the new strategy in situ may be adopted for the commercial preparation of hybrid polymer electrolyte for ASSBs applications.

As solid polymer electrolytes are attractive candidates for application in solid-state battery and various approaches such as dispersion of nanofiller, nanoclay intercalation is adopted to increase the ionic conductivity and other properties. Chen et al. [132] prepared the composite solid polymer electrolyte based on the PEO as host polymer, garnet $Li_{6.4}La_3Zr_{1.4}Ta_{0.6}O_{12}$ (LLZTO) as the ceramic, and lithium bis(trifluoromethanesulfonyl)imide (LiTFSI) as the salt. XRD pattern evidenced the poly-crystalline nature of LLZTO particles, and after embedding them in the PEO matrix, no change was observed that indicates the stability of LLZTO. DSC analysis indicates the shift of melting peak toward lower temperatures with the addition of LLZTO. The highest ionic conductivity was 1.17×10^{-4} S cm^{-1} (@ 30 °C) and 1.58×10^{-3} S cm^{-1} (@ 80 °C) for 10 wt% LLZTO particles. The increase in the conductivity was due to the increased free volume and faster chain movement which results from the uniform dispersion of LLZTO particles as evidenced by FESEM. The voltage stability window was about 5.0 V (vs. Li/Li +) and is in the safe limit of battery operation. The assembled cell displays a discharge capacity of 149.1 mAh g^{-1} at 0.1 C (@ 55 °C) and is 87.7% of the theoretical value (Fig. 20a, b). Further, charge–discharge indicates a decrease in discharge capacity from 149.3 → 80 mAh g^{-1} (for PEO_8-LiTFSI) and 149.3 → 139.1 mAh g^{-1} (for PEO_8-LiTFSI-10 wt% LLZTO) after 100 cycles at 0.2 C. It provides sufficient evidence of the increase cyclic stability after the dispersion of LLZTO particles. Another important point to be noted is that LLZTO-based solid polymer electrolytes effectively prevent dendrite growth formation as compared to LLZTO free. The cycling stability was investigated further by fabricating a cell ($LiFePO_4$ | Li) using PEO-LLZTO-PEG-60 wt% LiTFSI in voltage range 2.6–4.0 V (@ 0.2 C; T = 55 °C). Figure 20b displays the charge–discharge curve, and Fig. 20c shows the plot of discharge capacity and Coulombic efficiency against cycle number. The charge–discharge capacity is 123.4 and 122.5 mAh g^{-1} (Coulombic efficiency (CE) = 99.2%) and

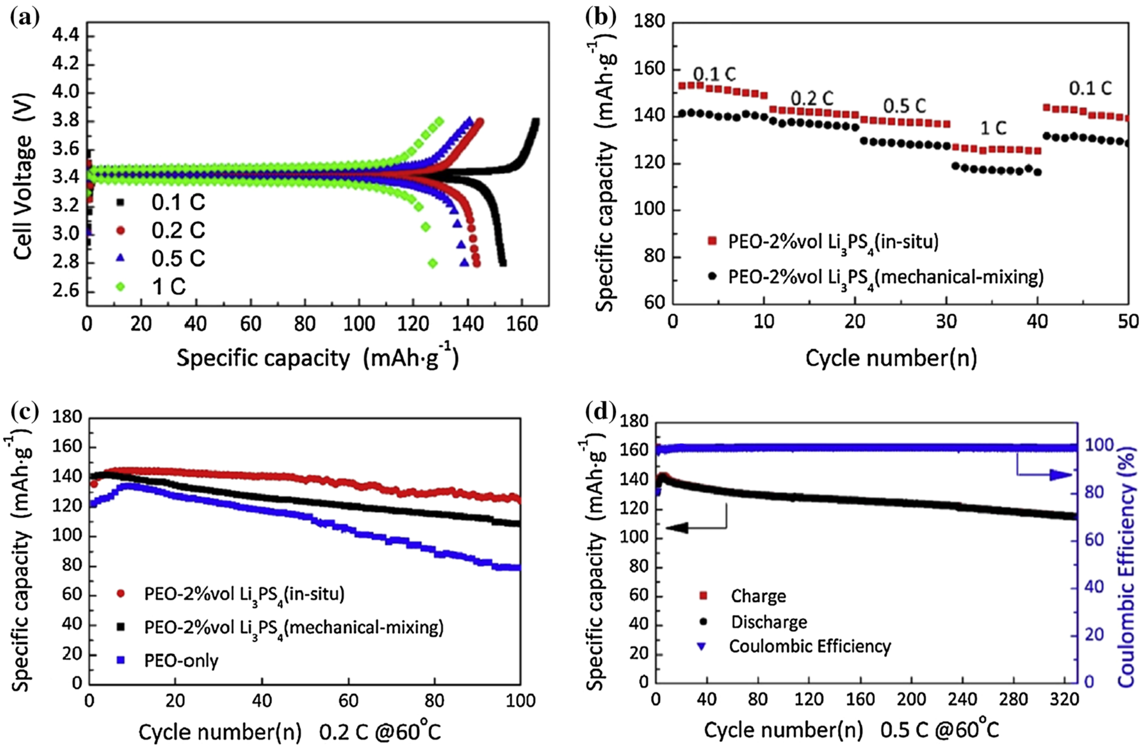

Figure 19 **a** The galvanostatic charge/discharge curves at varied current densities of cell LFP/PEO-2%vol Li_3PS_4(in situ)/Li. **b** Rate performance of varied current densities of cell LFP/PEO-2% vol Li_3PS_4 (in situ)/Li and cell LFP/PEO-2% vol Li_3PS_4(mechanical-mixing)/Li at 60 °C. **c** Specific discharge capacity of cell LFP/PEO-2%vol Li_3PS_4(in situ)/Li, cell LFP/PEO-2% vol Li_3PS_4 (mechanical-mixing)/Li and cell LFP/PEO/Li according to cycles at 0.2 C. **d** Cycling performance of cell LFP/PEO-2% vol Li_3PS_4(in situ)/Li at 0.5 C (Reproduced with permission from Ref. [130] © Elsevier 2018).

increases to 127 mAh g^{-1} (after 50 cycles; Coulombic efficiency = 100%). It confirms the stability of the electrode–electrolyte interface during cell operation. The charge–discharge capacity at different C-rates, and discharge capacity is as follows: 127.7 ((@ 0.2 C), 118.6 (@ 0.5 C), 103 (@ 1 C), 53 mAh g^{-1} (@ 2 C). Figure 20d displays the glowing LED that indicates the applicability of the "polymer-in-ceramic" electrolyte in batteries.

Recently, Liu et al. [133] have reported the preparation of the composite polymer electrolyte based on PEO as polymer matrix and $Li_{1.4}Al_{0.4}Ti_{1.6}(PO_4)_3$ (LATP) as nanoparticles with average size ~ 140 nm. The main motto was to examine the Li-ion conduction and effect on the cell capacity. It was observed from the FTIR spectra that LATP nanoparticles are dispersed in the polymer matrix with any interaction with the PEO evidenced by the absence of any shift in peak position. The highest ionic conductivity was observed for the PEO-LATP01 CPE which is about 6.17×10^{-6} S cm^{-1} (at 20 °C), 1.15×10^{-5} S cm^{-1} (at 30 °C) and reaches 7.03×10^{-4} S cm^{-1} (at 80 °C). The voltage stability window increases after LATP addition to 4.8 V, and mechanical properties were also improved. (Tensile stress increased from 0.35 to 0.95 MPa, and strain decreased from 1572% to 1244%.) The cycling performance of the $LiFePO_4$/LATP01/Li structured coin cells was examined to check the applicability of prepared electrolyte for commercial applications. The capacity was 118.3 mAh g^{-1} (initially it was 98.7 mAh g^{-1} with CE 84.2%) with Coulombic efficiency after 20 cycles. There was an increase in the capacity with temperature also and is 151.6 mAh g^{-1} (at 60 °C), which was 89.2% of the theoretic capacity of $LiFePO_4$. However, with further increase in a temperature decrease in capacity was observed owing to the low ionic conductivity and adhesive issues.

Another important approach is to control the architecture of the polymer electrolyte that plays two effective roles: one part supports the faster ion migration, while another provides mechanical strength. Recently, Wei et al. [113] have prepared the novel type of "centipede-like" PEO with short EO

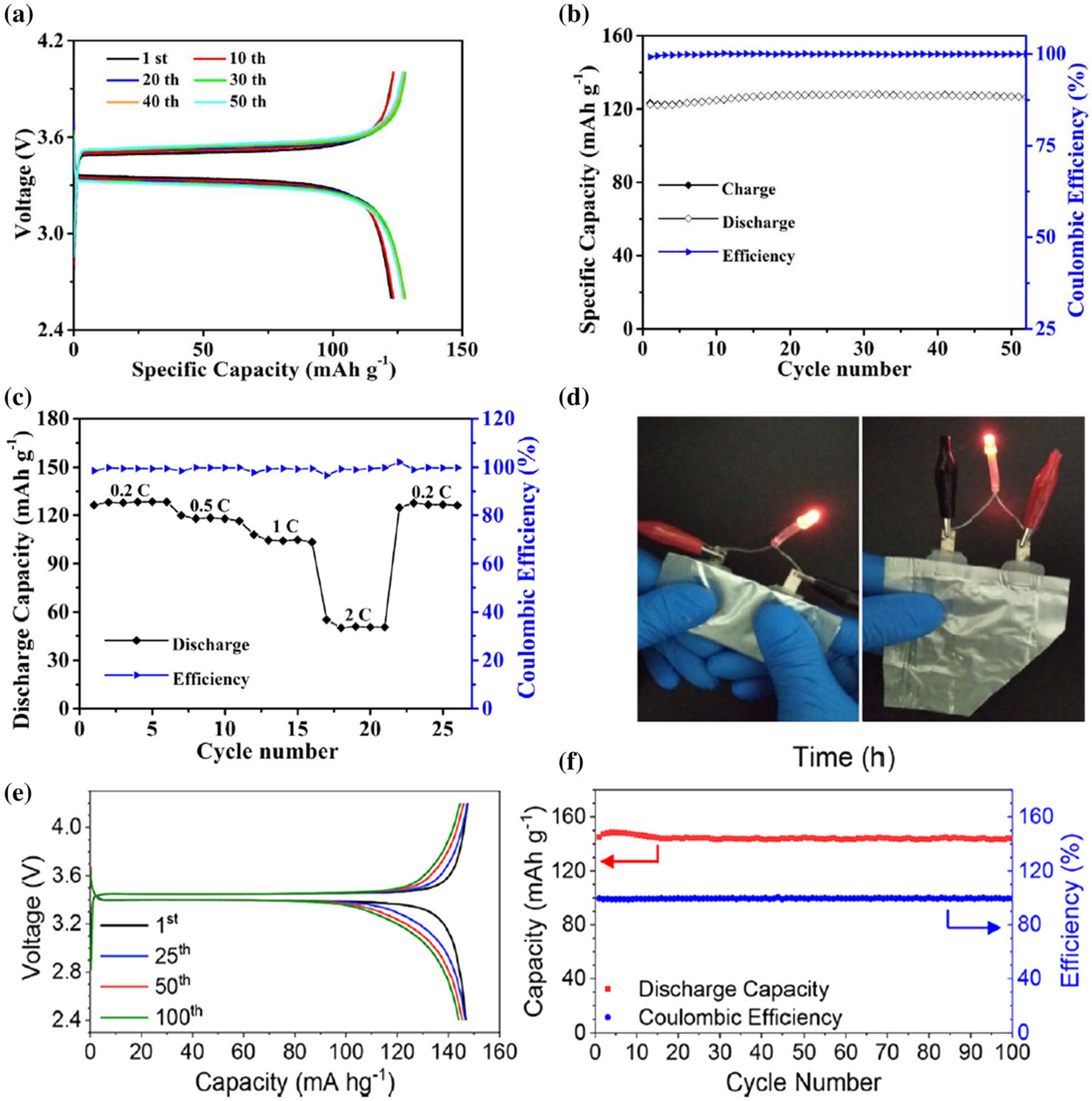

Figure 20 Electrochemical performance of "polymer-in-ceramic" electrolyte: The $LiFePO_4$|Li cells based on PEO-LLZTO-PEG-60 wt% LiTFSI with cutting-off 2.6–4.0 V and 55 °C: **a** charge–discharge voltage profiles at 0.2 C; **b** cycling performance at 0.2 C; **c** rate performance; **d** illustration of solid-state pouch Li metal cell showing well-running under folding and safety with being cut a corner (Reproduced with permission from Ref. [132] © Elsevier 2018), **e** Charge–discharge curves and **f** cycle performance of the Li/PEO^B12K-POSS/LFP batteries at 0.2 C and 30 °C (Reproduced with permission from Ref. [113] © American Chemical Society 2018).

branches (PEOB) [comb-like structure] and end functionalities. The mechanical strength is increased by the end functionality of the PEO^B, and the prepared film is transparent and flexible. The SPE with code PEO^B2K-POSS has the highest modulus, i.e., 4.1 MPa, and is effective in suppressing the dendrite growth. The highest ionic conductivity was 0.16 mS cm^{-1} (at 30 °C) and 0.7 mS cm^{-1} (at 60 °C) for the EO^B12K-4SH prepared by reaction of end-functionalized PEO^B with a thiol-containing tetrafunctional 4SH molecule. This enhancement in the conductivity was attributed to the unique architecture of PEO^B which results in low cross-link density and faster segmental motion of the polymer chain. The electrochemical stability window of the prepared electrolyte was 4.3 V. The electrochemical performance of the present SPE was examined by fabricating the symmetric cell Li/PEO^B12KPOSS/Li (Fig. 20e, f). The initial discharge capacity was 146.5 mAh g^{-1} with CE of about 99% (@ 0.2 C), and capacity is quite well even after 100 cycles

(144.5 mAh g^{-1} with CE > 99.7%). Authors conclude that the present polymer electrolyte has good cyclic stability as well as prevents dendrite growth effectively.

Block copolymer electrolyte

Block copolymer-based electrolytes are attractive due to their ability to combine ionic and mechanical properties. As most of the SPE operate efficiently only at an elevated temperature range ($\sim$ 70 °C) and for the better performance of the cell, the operational temperature range must be at room temperature due to advantages such as safety, low price, and good Li compatibility. To reduce the operating temperature range, Aldalur et al. [134] reported the development of a new solid polymer electrolyte. A new type of comb polymer matrix grafted with soft and disordered polyether moieties (Jeffamine®) and a popular salt, lithium bis (fluorosulfonyl) imide (LiFSI) was prepared by the solution cast technique. FESEM micrographs evidence the comparatively higher entanglement for Jeffamine polymer matrix as compared to PEO and are attributed to the EO and PPO disordered distribution. FTIR spectra confirmed the chemical stricture of SPE and DSC analysis evidences the increased degree of flexibility of the flexibility for Jeffamine-based SPE. The prepared system displays thermal stability up to 200 °C. Now, the ionic conductivity is also higher for the Jeffamine-based SPE and is 5.6×10^{-4} S cm^{-1} (@ 70 °C), 2×10^{-4} S cm^{-1} (@ 40 °C) and cation transference number is 0.16 (@ 70 & 40 °C). The voltage stability window for the Jeffamine-based SPEs is 4 V and is lower than PEO due to the presence of PPO segment which has a high possibility of oxidation. But, the voltage window lies in the range for practical applications (3.5 V vs. Li°/Li^{+}). The cycling performance evidences the increase in the initial capacity for LiFSI/Jeffamine-based SPEs, i.e., 160 mAh g^{-1} @ C/20, and then decreases to 120 mAh g^{-1} at C/10 (Fig. 21a, b). It was concluded that the LiFSI/Jeffamine-based SPE battery displays a Coulombic efficiency for 50 cycles owing to the high ionic conductivity and broad stability window.

Another report by Aldalur et al. [135] explored the new self-standing SPE using block copolymers having Jeffamine-based blocks and mechanically stable polystyrene moieties (Jeffamine®-PS,). All the SPE shows a decomposition temperature higher than 300 °C with the overall thermal stability of about 350 °C. The ionic conductivity value is highest for BCP70 matrix and is about 5.6×10^{-4} S cm^{-1} (@ 70 °C) and 7.9×10^{-5} S cm^{-1} (@ 40 °C). With further increase in PS block content decrease in conductivity is attributed to the reduction in conductive volume and increase in glass transition temperature (as supported by DSC result).

The cation transference number was low for BCP70 matrix, i.e., 0.08, and is due to the enhanced tortuosity in the cation path in the Jeffamine chain along with PS blocks. The electrochemical performance of the cell shows a discharge capacity of about 140 mAh g^{-1}, and good compatibility of the Jeffamine-based electrolyte with Li-metal is evidenced (Fig. 21c–e). The voltage stability window was higher than 5 V for BCP70 (Fig. 21f).

Another important approach to achieve the desirable properties of SPE is the modulation of properties preparing semi-interpenetrating network polymer electrolytes. Recently, Duan et al. [136] have reported the preparation of the in situ plasticized solid-state polymer electrolyte with double network (DN-SPE) via facile polymerization. The DN-SPE demonstrates a decrease in crystallinity, and FESEM confirms the smooth morphology. The highest ionic conductivity obtained was 5.3×10^{-5} S cm^{-1} (PEGDE-PEGDA-1000) and is attributed to the mutual plasticization of the double network (PEGDE:PEGDA). The high value of cation transport number (0.44) and broad voltage stability window (4.7 V) confirms the suitability of the SPE for Li-ion battery applications. The electrochemical properties were tested by fabricating the LFP/PEGDE-PEGDA-1000/Li cell and shows specific capacity (162 mAh g^{-1}) and decreases to 125 mAh g^{-1} after 125th cycle with a CE > 99.5%. Along with this, the dendrite growth suppression was checked and it was found that DN-SPE effective suppresses the dendrites. This is owing to the good interfacial contact that favors smooth cation transport.

Another approach to achieve the single-ion conduction (SIC) in SPE is the development of block copolymer electrolytes that is based on the fact that the anion gets linked with the immobilized polymer backbone. The cation migration is via the microphase-separated polymer hots block. Nguyen et al. [137] prepared a multi-block aromatic structure (SI) that provides improved ionic conductivity, good mechanical stability, and ion mobility. The highest ionic conductivity is 3.2×10^{-4} S cm^{-1}, and the voltage stability window is 4.9 V. The

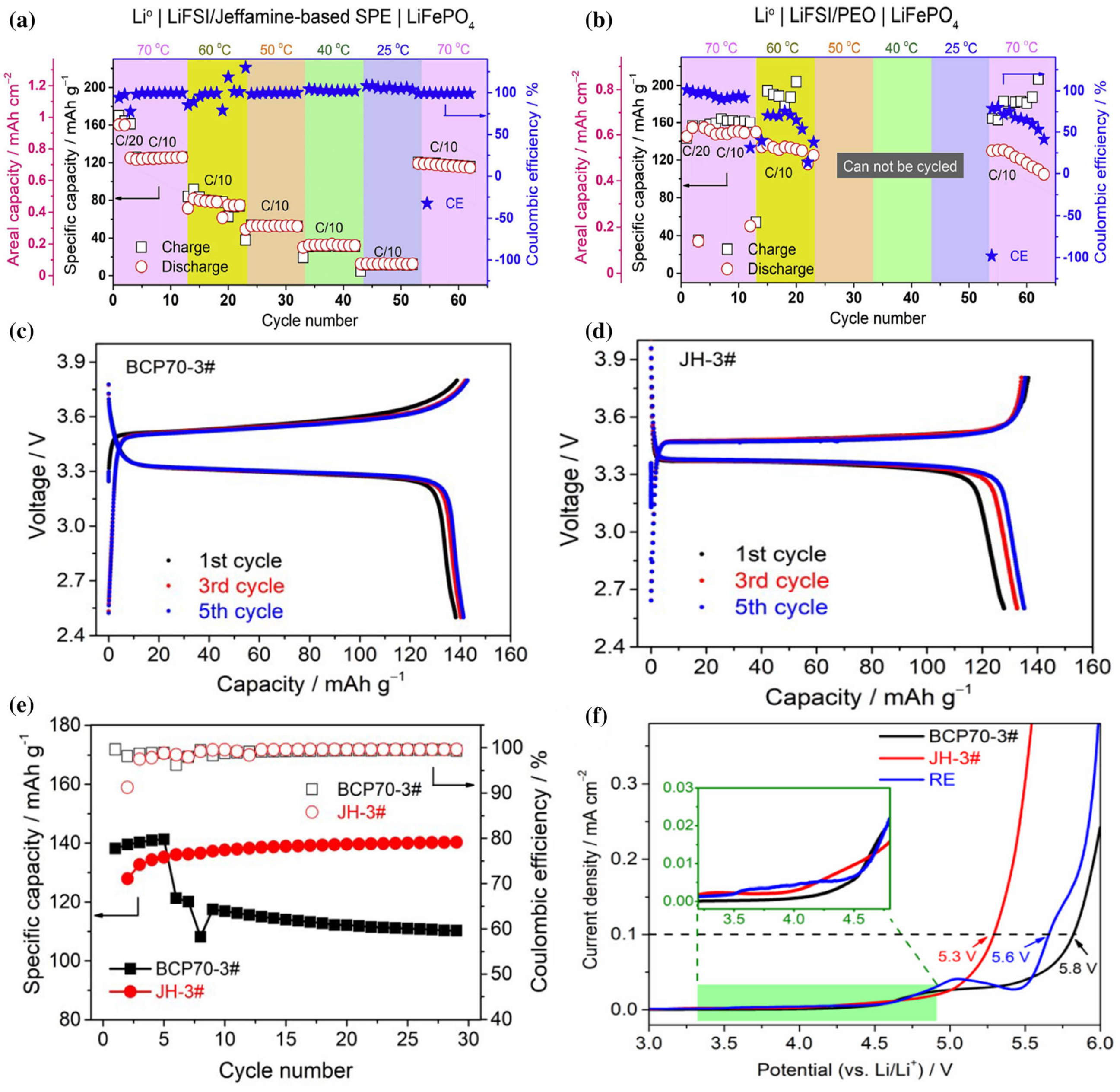

Figure 21 Specific/areal capacity and Coulombic efficiency versus cycle number for the Li°|LiFePO$_4$ cells using **a** LiFSI/Jeffamine-based and **b** LiFSI/PEO-based SPEs at various temperatures.(Reproduced with permission from Ref. [134] © Elsevier 2018), Charge/discharge profiles of the Li | SPEs | LFP cells using **c** BCP70-3# and **d** JH-3# electrolytes at 70 °C. Charge/discharge rate: 0.05/0.05 C. **e** Specific discharge capacity and Coulombic efficiency versus cycle number for the cells using BCP70-3# and JH-3# electrolytes cycled at 70 °C. Charge/discharge rate: 0.05/0.05 C (the first five cycles) and 0.1/0.1 C (the following cycles), **f** Linear sweeping voltammetry profiles of Li || stainless steel (SS) cells using the as-prepared BCP70-3#, JH-3# and RE at 70 °C (Reproduced with permission from Ref. [135] © Wiley 2018).

electrochemical performance of cells fabricated using this electrolyte was tested by GCD. The initial discharge capacity is about 150 mAh g^{-1} (at C/20) with CE about 86%. The CE increases to 99.5% after 230 cycles (Fig. 22a, b).

Polycarbonate-based electrolyte

Another interesting candidate that may replace the solid polymer electrolyte is polycarbonate (PC)-based SPE (PTMC-PCL, PEC, PPC, PPCAGE, IPN-PDEC)

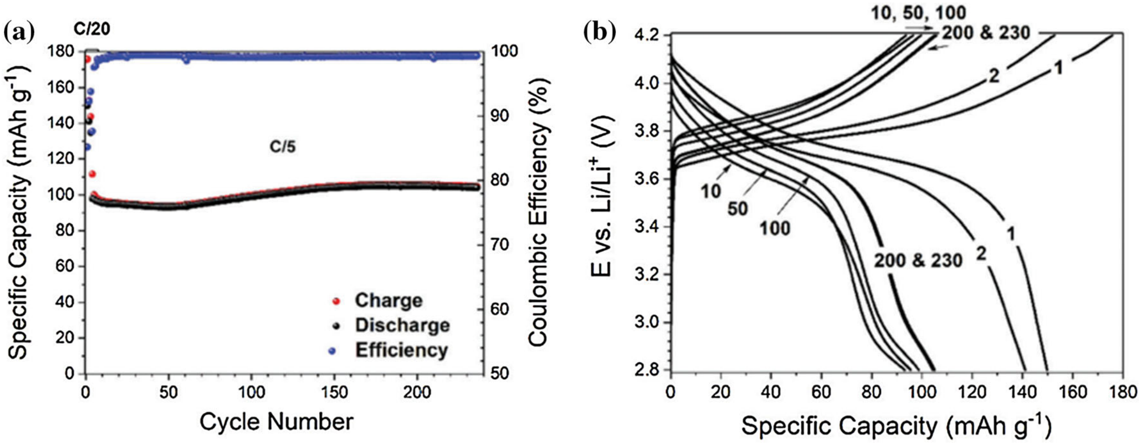

Figure 22 Investigation of SI-S55 in Li/NCM cells via galvanostatic cycling: **a** discharge/charge capacities and Coulombic efficiency as a function of cycle number; the first three cycles were conducted at C/20—all following ones at C/5; **b** the corresponding potential profiles for selected cycles. The cutoff potentials were set to 2.8 and 4.2 V versus Li/Li$^+$, and the cells were kept at a constant temperature of 40 1 C (Reproduced with permission from Ref. [137] © RSC Publishing 2018).

and has advantageous such as good salt solubility due to the presence of highly polar carbonate group (–O–(C=O)–O–) [105]. PC-based SPE also provides high ionic conductivity, higher ion transference number, broad voltage stability window, and good compatibility with the Li anode. Another attractive polymer is polyurethane (PU) and comprises two segments: (1) soft segment (SS) and (2) hard segment (HS). The former one (SS) makes PU stretchable and flexible which supports ion migration, while latter one improves the mechanical property of electrolyte. This unique structure promotes its use in developing polymer electrolytes with balanced electrical and mechanical properties [138–140].

Recently, Bao et al. [141] have investigated the effect of the soft and hard segments of PU on the polycarbonate-based polyurethanes (PCPU) with different contents of polycarbonate diol (PCDL), 1,6-hexamethylene diisocyanate (HDI), and diethylene glycol (DEG) prepared by an addition polymerization reaction and LITFSI was used as salt. Firstly, the polycarbonate-based polyurethane (PCPU) formations were evidenced by FTIR and NMR. DSC analysis displays the two T_g: one associated with a soft segment ($T_{g,s}$ = – 40–50 °C) and another with a hard segment ($T_{h,s}$ = 42–48 °C). Also, the $T_{g,s}$ decreases with the increase in hard segment content. All PCPU is thermally stable up to 300 °C. The mechanical analysis indicates the increase in the tensile strength with an increase in hard segment. The improved mechanical strength on the addition of the hard segment is due to two reasons: (i) interaction via hydrogen bonding between neighboring units of 1,6-hexamethylene diisocyanate (HDI) units, and (ii) HS acts as reinforcing filler [142, 143]. The improved mechanical properties hold the key to prevent dendrite growth formation and proper cell packaging. The highest ionic conductivity was 2.2×10^{-6} S cm^{-1} (@ 25 °C), 1.58×10^{-5} S cm^{-1} (@ 60 °C) and 1.12×10^{-4} S cm^{-1} (@ 80 °C) for 20 wt% salt content. The most of contribution to the conductivity was from the soft segments. The voltage stability window was 4.5 V @ 80 °C and is in the required limit for practical applications. The electrochemical performance was tested by fabricating the cell ($LiFePO_4$/SPE/Li) using the prepared SPE. The discharge capacities are 128 mAh g^{-1} (@ 0.2 C), 92 mAh g^{-1} (@ 0.5 C) and 41 mAh g^{-1} (@ 1 C) as shown in Fig. 23a, b (@ 60 °C). Figure 25c shows the cycling performance for PCPU10-20% electrolyte and shows 128 mAh g^{-1} (1st cycle @ 0.2 C) and 127 mAh g^{-1} after the 100th cycle with capacity retention 99% and Columbic efficiency about 100%. The improved performance is attributed to the PCPU electrolyte which prevents dendrite growth formation, and improved mechanical properties played an effective role in enhancing the electrochemical stability. Figure 23d, e shows the charge–discharge curves at different C-rates (@ 80 °C), and cell delivers discharge capacity about 161 mAh g^{-1} (@ 0.2 C), 158 mAh g^{-1} (@ 0.5 C), 134 mAh g^{-1} (@ 1 C), 93 mAh g^{-1} (@ 2 C), and 46 mAh g^{-1} (@ 3 C). Figure 23f shows the cycling performance for the

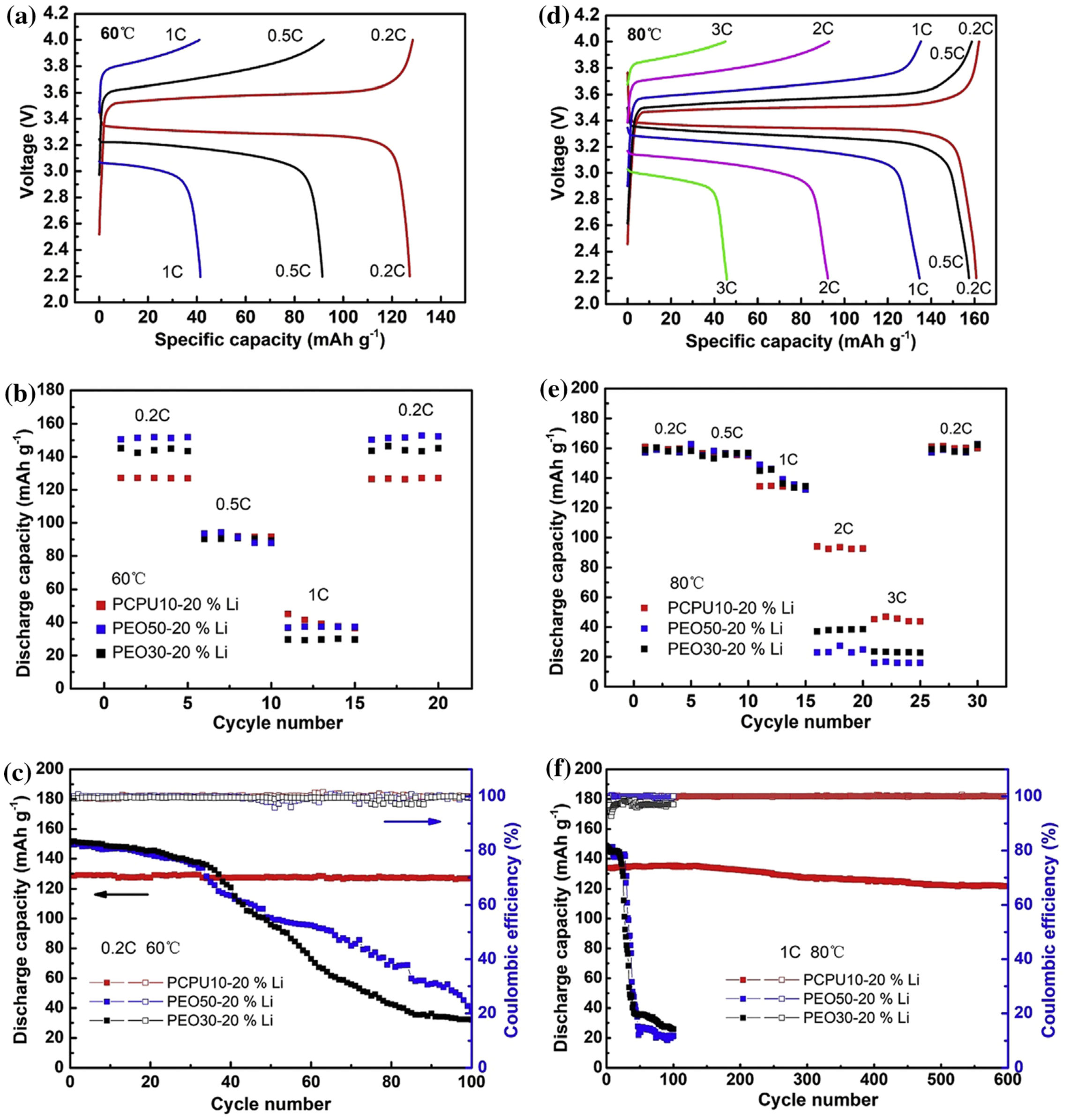

Figure 23 **a** The charge/discharge curves and **b** C-rate capability and **c** cycling performance at 0.2 C for $LiFePO_4$/SPE/Li all-solid-state batteries at 60 °C; **d** the charge/discharge curves and **e** C-rate capability and **f** cycling performance at 1 C for $LiFePO_4$/SPE/Li all-solid-state batteries at 80 °C (Reproduced with permission from Ref. [141] © Elsevier 2018).

PCPU 10–20% electrolyte (@ 1 C and 80 °C), and after 600 cycles capacity retention is 91%. This stability was verified by the FESEM images which shows stable cathode and SPE interface after 600 cycles. In conclusion, it may be adopted as a solid polymer electrolyte for the solid-state Li-ion batteries.

As solid polymer electrolytes are the fascinating candidate for solid-state batteries, however, some issues remain attached to practical aspects associated with the preparation method. As the standard technique to prepare the solid polymer electrolyte is the solution cast technique that uses volatile organic solvents (DMF, CAN, etc.) that may harm the environment. One alternative is the waterborne polyurethane (WPU) that possesses the properties as required for the separator cum electrolyte and can be tailored based on the soft/hard segments [140].

To check the applicability of WPU as a separator, Cong et al. [144] reported the preparation of the WPE as polymer matrix by polymerization of polyethylene glycol (PEG), hexamethylene diisocyanate (HDI), diethylene glycol (DEG), dimethylol propionic acid

(DMPA) with LiTFSI as salt, and water was used as a solvent. The structure of WPU was confirmed by the ^{1}H NMR and FTIR spectra. FTIR spectrum showed the peak broadening and shift toward the high wavenumber side of –NH peak (At 3327 cm^{-1}) of WPU. This promotes the cation coordination with the carbonyl group of WPU and ether oxygen of PEG segments, as evidenced by the lower wavenumber shift in the stretching of –C=O and –COC– bond. Further XRD analysis suggested the increase in the amorphous content and reduction in the crystallization of WPU after salt addition, also supported by the DSC analysis. SEM analysis evidenced the smooth morphology and uniform distribution of salt. After the addition of the salt, the film becomes more transparent and flexible. TGA analysis indicates the increase in thermal stability after salt addition, owing to the formation of a transient cross-link between the cation and oxygen of the soft/hard segments. The stress–strain curve evidenced the increase in the mechanical properties after salt addition, the tensile strength of 0.5 MPa with an extended elongation-at-break value of 300% for WPU-20% Li. For the same system, further activation energy was in the range of 0.25–0.27 eV and lowering of activation energy suggests the presence of transient dynamical coupling between cations and polymer chain segmental motion in SPE. The same has been reported earlier also [145].

The voltage stability window was about 4.8 V (@ 60 °C) and is sufficient for the solid-state Li-ion battery applications. Then, $LiFePO_4$/WPU-20% Li/Li cells were fabricated and charge–discharge of the cell shows discharge capacity (@ 60 °C) as 151 mAh g^{-1} (@ 0.1 C), 145 mAh g^{-1} (@ 0.2 C), 114 mAh g^{-1} (@ 0.5 C), 102 mAh g^{-1} (@ 1 C), and 25 mAh g^{-1} (@ 2 C). It was noticed that at a low rate high capacity was obtained while at a high rate rapid capacity fading was observed (Fig. 24a, b). This was attributed to the presence of hard segments that prevents cation migration at operating temperature. Further cycling

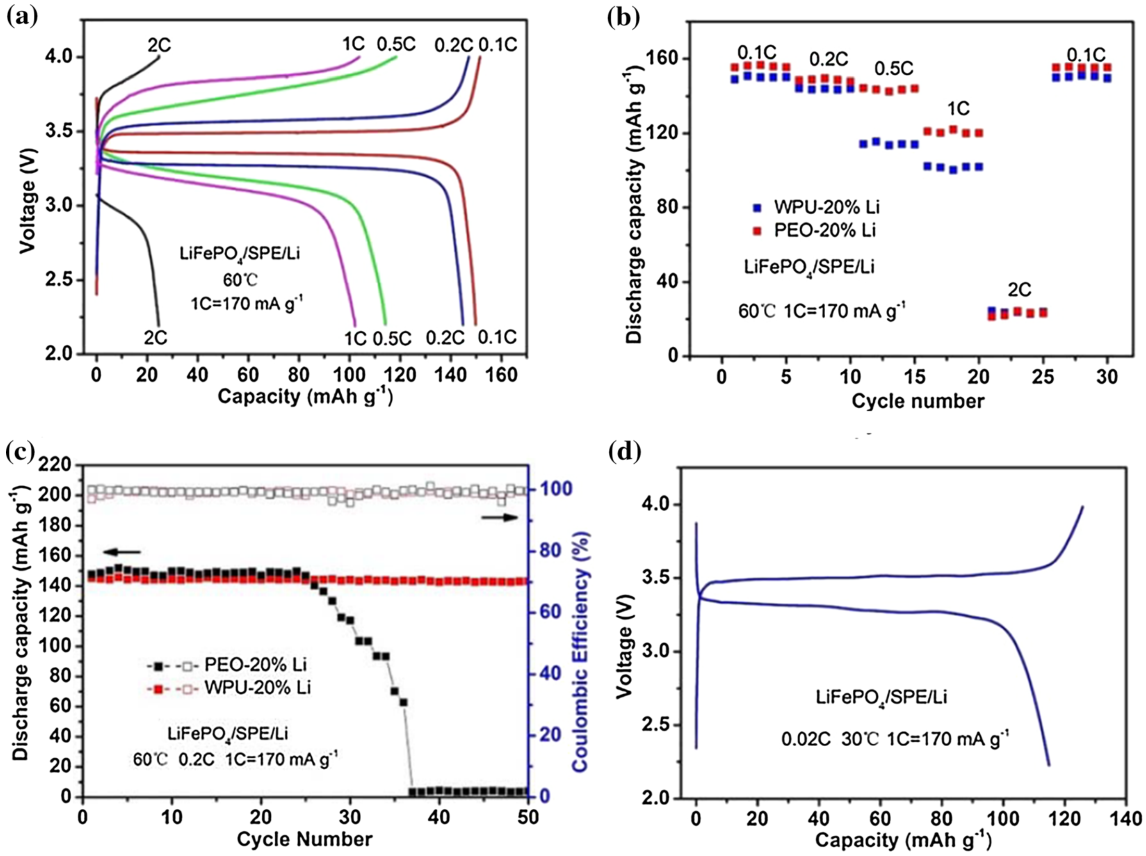

Figure 24 **a** The charge and discharge curves of $LiFePO_4$/SPE/Li battery usingWPU-20%Li as electrolyte at different rates and **b** C-rate capability and **c** cycling performance of the batteries at 60 °C, where the electrolytes were WPU-20% Li and PEO-20% Li; **d** the initial charge and discharge curves of the battery usingWPU-20% Li SPE at 0.02 C at 30 °C (Reproduced with permission from Ref. [144] © Elsevier 2018).

stability was checked and fabricated cell delivers. The discharge capacity of 141 mAh g^{-1} with a capacity retention of 97% after 50 cycles (Fig. 24c, d). It was concluded that the WPU may be adopted as an environmental friendly candidate for solid-state Li-ion batteries.

Recently, Zhang et al. [146] have reported the preparation of poly(propylene carbonate)/$Li_{6.75}La_{3}Zr_{1.75}Ta_{0.25}O_{12}$ composite solid electrolyte. The highest conductivity was 5.2 × 10^{-4} S cm^{-1} (@ 20 °C) and is attributed to the decrease in crystallinity and increased the segmental motion of polymer chains. Another reason may be the formation of conductive paths owing to the PPC matrix and LLZTO bulk interface. The voltage stability window is about 4.6 V, and high cation transference number 0.75 suggests the faster ion migration which is in correlation with high ionic conductivity value. The electrochemical performance has been examined using this electrolyte in Li/PPCL-SPE/Li cell. Even after the 200th cycle, 95% capacity is retained that confirms its good cyclic stability. The utility of PPCL-SPE is checked by fabricating LiFePO4/Li4Ti5O12 lithium-ion full cells (Fig. 25a–c). The cell shows 123 mAh g^{-1} at 0.1 C. The charge transfer resistance is about 70 Ω, and even after 800th cycle charge transfer resistance is about 90 Ω. The fabricated cell glows an LED as shown in Fig. 25d and evidences the suitability of PPCl-SPE for Li-ion battery applications.

Star polymer electrolyte

The star polymer electrolyte comprising star-shaped copolymers having POSS segments is an attractive candidate due to unique features such as a unique multiple-chain-ended structure. Zhang et al. [92] synthesized the SPE of star structure with octavinyl octasilsesquioxane (OV-POSS) and poly(ethylene glycol) methyl ether methacrylate (PEGMEM) by one-step free radical polymerization. One unique feature was that the POSS macromonomer has multifunctional corner groups. The star-shaped PE shows improved free volume and thermal stability as compared to the linear polymer. The star-shaped polymer electrolyte (SCP5.1) shows a higher conductivity of 1.13 × 10^{-4} S cm^{-1}, than the linear copolymer electrolyte (LCP5.1) which shows about 5.63 × 10^{-5} S cm^{-1} (At 25 °C). It is attributed to the availability for more free volume for star-shaped PE than linear PE. Also, the cation transference number was higher for SCP5.1 (t_{+}=0.35) than for LCP5.1 (t_{+}=0.19). The voltage stability window for SCP5.1 is about 5.31 and 5.04 V (vs. Li/Li^{+}) at 25 and 80 °C.

The electrochemical performance was examined by fabricating Li/SCP5.1/$LiFePO_4$ cells. The cell shows the initial discharge capacity of about 116.2 mAh g^{-1}, with a Coulombic efficiency of ~ 99% (Fig. 25e, f). Even at high temperature (At 80 °C) the SCP5.1 electrolyte-based cell shows an initial discharge capacity of about 163.8 mAh g^{-1} and after the 100th cycle decreases to 147.8 mAh g^{-1} with a capacity retention ratio of about 90.2% (CE; η = 100%), while for Li/LCP5.1/$LiFePO_4$ cell the initial discharge capacity was 72.6 mAh g^{-1} and 91.1 mAh g^{-1} after the 100th cycle. It was suggested that the star shape polymer architecture has the potential to become an alternative candidate for battery applications.

Recently, Xiao et al. [119] have reported the preparation of the star polymer electrolyte using poly(ethylene glycol) dimethacrylate (PEGDMA) as a monomer and ethylene glycol dimethacrylate (EGDMA) as cross-linker. The synthesized PE is flexible with a tensile stress of about 1.67 MPa with a strain of about 300%. The highest ionic conductivity is 1.48 × 10^{-5} S cm^{-1} (at 20 °C) for $PEGDMA_{550}$ (Li-SPE550-Li) and is attributed to the favorable topological architecture that promotes the fast ion migration. The voltage stability window of cell Li|SPE|SS is about 5.4 V, and the cation transference number of cell Li|SPE|Li is 0.3. The electrochemical performance of the cell Li|K-SPE750-Li|LFP is examined using CV. The cell shows an initial discharge capacity of about 137.7 mAh g^{-1} and after 150 cycles is 130.5 mAh g^{-1} with a capacity retention of 95% (Fig. 26a–d). The CE is 97% for the first cycle and after 150 cycles is 98%. The charge–discharge curve for the Li|K-SPE750-Li|LFP cell shows the initial discharge capacity of about 127.1 mAh g^{-1} at a rate of 0.2 C. It was concluded that the tailor-made star polymer possesses desirable properties and can be adopted as a candidate for energy storage/conversion devices.

The fibrous membrane as the electrolyte

Gopalan et al. [147] reported the preparation of the PAN electrospun fibrous membranes (PVDF–PAN–ESFMs) using the electrospinning technique. The 1 M $LiClO_4$–PC solution was used as the electrolyte. The prepared membraned shows desirable dimensional stability after electrolyte uptake even after swelling.

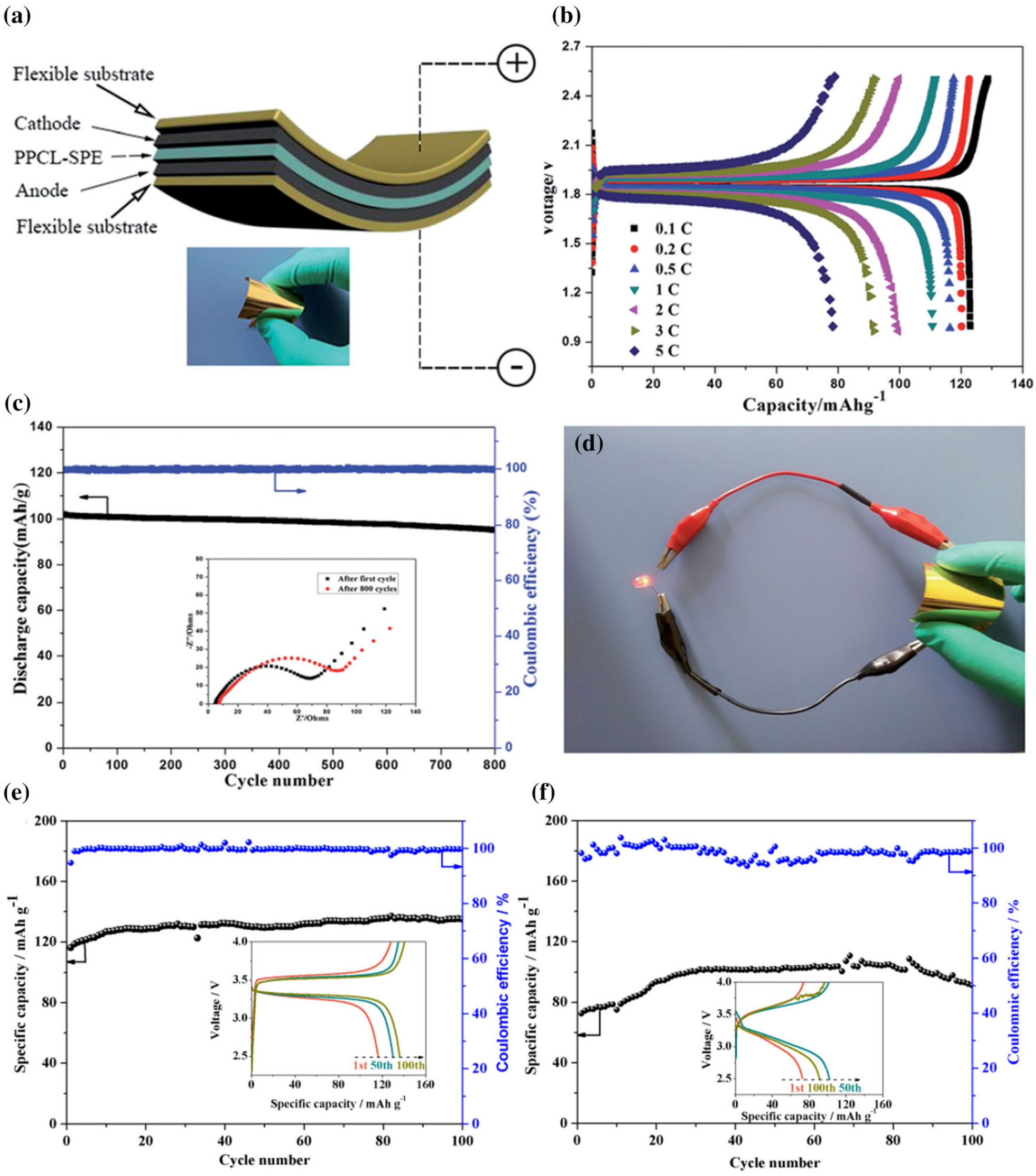

Figure 25 **a** Schematic of flexible solid state $LiFePO_4/Li_4Ti_5O_{12}$ lithium-ion full cell. **b** Typical charge/discharge curves and **c** cycle performance of solid state $LiFePO_4/Li_4Ti_5O_{12}$ lithium-ion full cell. The inset is the impedance spectrum for the cell using PPCL-SPE after the first cycle and 800 cycles. **d** Illustration of flexible solid state $LiFePO_4/Li_4Ti_5O_{12}$ lithium-ion full cell for lighting LED lamp in a bent state. Temperature: 20 °C (Reproduced with permission from Ref. [146] © Royal Society of Chemistry 2017), cycling performance of the $Li/LiFePO^4$ cell with **e** SCP5.1 and **f** LCP5.1 solid electrolyte at 25 °C with a current density of 0.5 C. The inset: the corresponding charge/discharge curves at different cycles (Reproduced with permission from Ref. [92] © Elsevier 2016).

FESEM analysis evidenced the formation of PVdF-ESFM fibers interconnected with a large number of voids, and uniform diameter was 600 nm. The interconnected morphology was due to the presence of the probable molecular level interactions between C–F (in PVdF) and –CN (in PAN) groups. The DSC analysis depicts the single glass transition temperature, and it indicates the proper miscibility of the

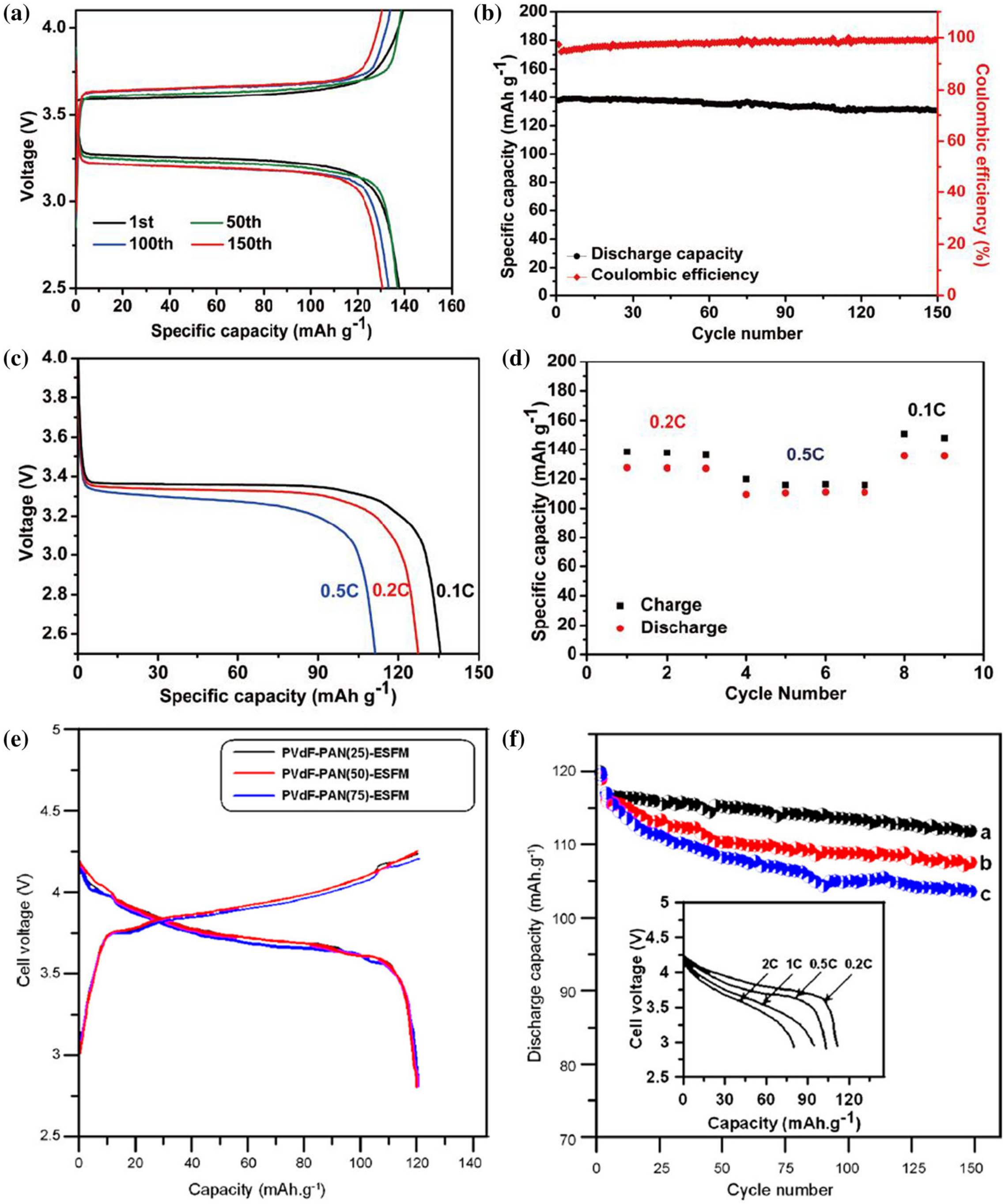

Figure 26 **a** Charge–discharge profiles, **b** cycle performance of Li|K-SPE750-Li|LFP cell with a certain current density of 0.1 C at 60 °C, **c** charge–discharge curves of Li|K-SPE750-Li|LFP cell at different rates, **d** specific capacity of Li/LFP|Li cells at different current densities at 60 °C (Reproduced with permission from Ref. [119] © Elsevier 2018), **e** Initial charge–discharge curves for the pouch cells with PVdF–PA–ESFMs as electrolytes; cells were cycled at 0.1C rate between 2.8 and 4.25 V, **f** Discharge capacity versus number of cycles of the pouch cells with **a** PVdF–PAN(25)–ESFM, **b** PVdF–PAN(50)–ESFM and **c** PVdF–PAN(75)–ESFM as an electrolyte: inset shows the discharge voltage profile at various rate for PVdF–PAN(25)–ESFM; anode, lithium; cathode, $LiCoO_2$; temperature, 25 °C. The cell was charged at 0.1 C rate (Reproduced with permission from Ref. [147] © Elsevier 2008).

PVdF-PAN. The highest ionic conductivity was 7.8×10^{-3} S cm^{-1} (@ 25 °C) and is higher than that of the PVDF-based electrolytes which is attributed to the elimination of crystalline domains after PAN addition [148]. The voltage stability window of the PVdF–PAN (25)–ESFM was 5.1 V and is much higher than the PVdF (i.e. 4.38 V) and PAN (i.e. 4.25 V) membranes. The electrochemical analysis was performed of cell $LiCoO_2$/PVdF–PAN–ESFM/Li between 2.8 and 4.25 V (@ 0.1 C). The discharge capacity was 120.4 mAh g^{-1} (@ 0.1 C) and after 150th cycle capacity retention was 93% (Fig. 26e, f).

In-gel polymer electrolytes, PVdF-co-HFP-based polymer electrolytes (electrospinning and non-woven) are a fascinating candidate due to the advantage associated with them: (1) desirable flexibility, (2) broad electrochemical stability window, (3) non-flammability, etc. But, their remains one issue that is leakage of electrolyte even after the addition of ionic liquid [149–151]. So, an oligomeric ionic liquid-type gel polymer electrolyte based on oligomeric ionic liquids, PVDF-co-HFP, and an electrolyte solution was reported by Kuo et al. [152]. The novel point was the synthesization of the oligomeric ionic liquid from phenolic epoxy resin based on a new approach to improve the conductivity, interfacial resistance, and the thermal properties. The prepared polymer membrane was flexible and semitransparent and possesses porous morphology. The ionic conductivity was higher (0.12×10^{-3} S cm^{-1}; @ RT) as compared to PVdF-HFP gel polymer electrolyte, and temperature dependence of conductivity follows Arrhenius's behavior for PVdF-HFP/30% OIL and PVdF-HFP/50% OIL. This indicates the decoupling of polymer chain segmental motion from ion transport and occurs via the pores, while PVdF-HFP/70% OIL system follows VTF behavior, due to the softening of the ionized oligomer with an increase of temperature, and hence faster ion migration. It is further evidenced by the low value of bulk (R_b = 6 Ω) and interfacial (R_i = 45 Ω) resistance for PVdF-HFP/70% OIL system, hence better interfacial stability. The electrochemical voltage stability window was about 4.5 V. The charge–discharge was performed for PVdF-HFP/70% OIL gel electrolyte, and the initial discharge capacity was 152 mAh g^{-1} (@ 0.1 C), 141 mAh g^{-1} (@ 1 C), 117 mAh g^{-1} (@ 3 C) (Fig. 27a). Figure 27b shows cyclic stability and depicts the CE of about 99% after 100 cycles. Then, the flame-retardant ability was checked by the limiting oxygen index (LOI) test that evaluates the minimum concentration of oxygen to support the combustion of the material (for non-flammable LOI = 22–27, for flame-retardant LOI > 27). In the present case, the LOI value was 31 (for a dry PVdF-HFP/70% OIL membrane) and 29 (for PVdF-HFP/70% OIL mixed liquid electrolyte solutions). This confirms the improved non-flammability along with cyclic stability and safety for the battery.

It is well known that the blending approach is an important approach to enhance the electrical and mechanical properties. But, one issue that remains there is the poor compatibility of blend polymer with the PEO that reflects the phase separation. So, a new approach was proposed to synthesize the solid polymer electrolyte. It comprises two chemically dissimilar polymer segments: (1) aromatic polymer segment and (2) host polymer matrix. The former one provides sufficient mechanical/thermal stability, while the latter one facilities us with flexibility and low crystallinity. So, Lu et al. [153] proposed a system in which polysulfone plays a role as a former one and PEO as the latter one. The self-standing solid polymer electrolyte membrane based on PSF–PEO matrix, with lithium bis-trifluoromethanesulfonimide (LiTFSI) and low content of SN was synthesized by one-step condensation copolymerization. A broad peak in the XRD diffractograms indicates the presence of large amorphous content and is due to the amorphous nature of the PSF block that prevents the PEO crystallization. The impedance analysis suggests that the role of PSF is to stabilize the solid polymer electrolyte structure framework only, while improvement in conductivity is enabled by the addition of SN. The highest ionic conductivity is 1.6×10^{-4} S cm^{-1} (At RT) and increases to 1.14×10^{-3} S cm^{-1} (@ 80 °C) for $PSF–PEO_{35}$-+ LiTFSI + SN system. The voltage stability window of the prepared system is 4.2 V vs. Li/Li^+ and is in a desirable range. A Li/$PSF–PEO_{35}$-+ LiTFSI + SN/$LiFePO_4$ full cell was fabricated to check the cyclic performance and displayed a discharge capacity of 152 mAh g^{-1} (@ C/3 rate) and after 30 cycles are ~ 125 mAh g^{-1} (Fig. 27c, d).

Another important approach to improve the properties of polymer electrolyte is the copolymerization technique. It improves the electrolyte uptake as well as the amorphous content. Recently, Shi et al. [154] have prepared a gel polymer electrolyte by blending the PEO & PMMA with copolymer P(VDF-

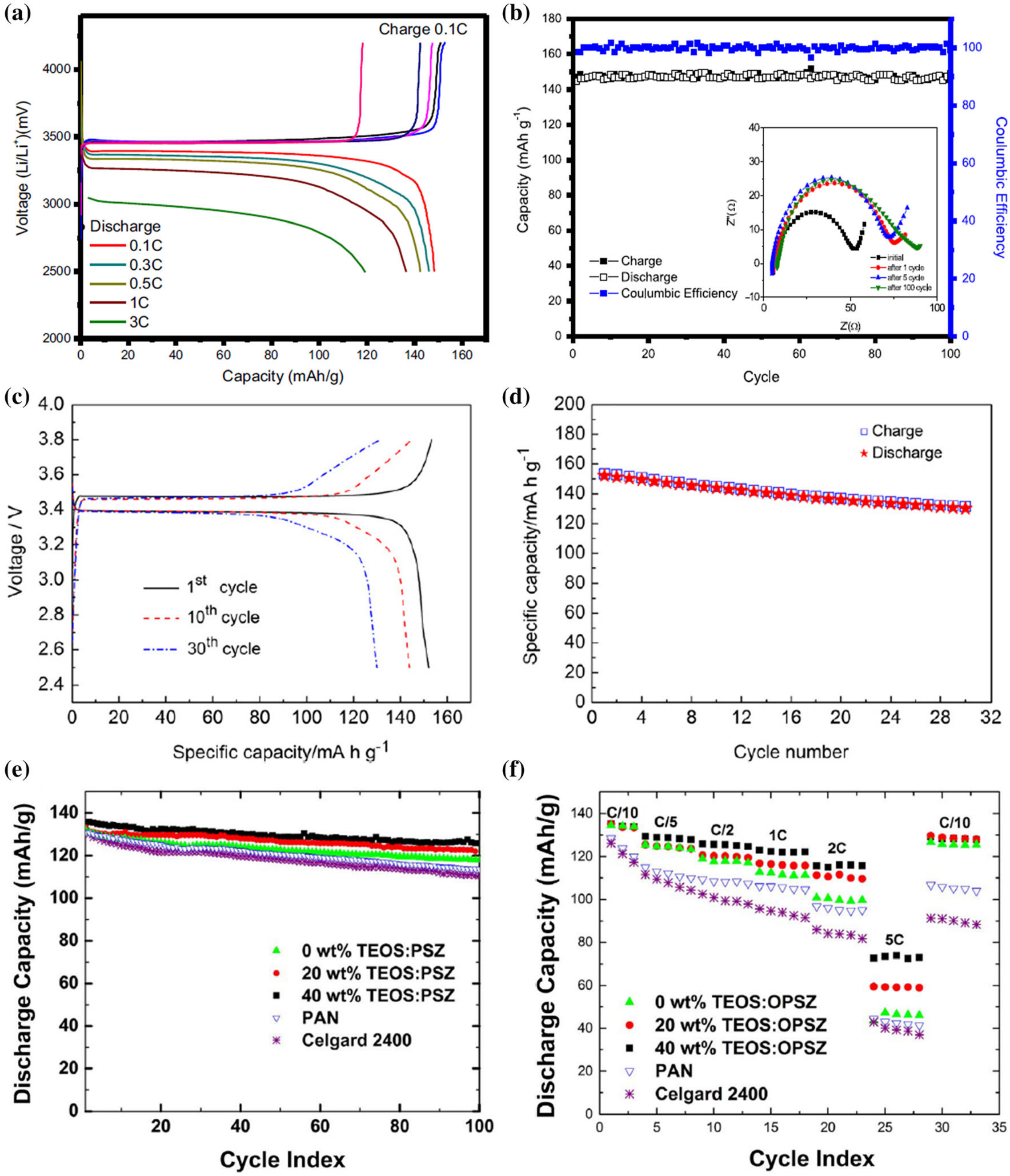

Figure 27 **a** Charge–discharge profiles of Li/PVdF-HFP/70% OIL/LiFePO$_4$ battery tests at various C-rates. LiFePO$_4$ has assumed a maximal theoretical capacity of 170 mAh g^{-1} for this study, and **b** cyclic performance of Li/PVdF-HFP/70% OIL/LiFePO$_4$ at a constant current density of 0.5 C (Reproduced with permission from Ref. [152] © Elsevier 2016), galvanostatic charge–discharge profiles **c** and cycling performance **d** for Li/PSF–PEO$_{35}$ + LiTFSI + SN/LiFePO$_4$ cell at 80 °C (Reproduced with permission from Ref. [153], © Elsevier 2013), **e** The cycle performances of LiCoO$_2$/graphite full cells with various separator membranes at 0.2 C, and **f** Results of rate capability tests for the LiCoO$_2$/graphite full cells with various separator membranes (Reproduced with permission from Ref. [154], © Elsevier 2017).

HFP) (PE-PM-PVH) by solution cast technique using liquid electrolyte of LiPF$_6$—EC + DMC (1:1 v/v) as the plasticizer. FESEM analysis evidenced the creation and growth of the pores after PEO-PMMA blending with P(VDF-HFP) (Porosity = 58%) as compared to pristine P(VDF-HFP) (porosity = 30%).

This increase in pore size may be due to the high absorbability of the PE-PM-PVH membrane. The thermal stability of the PE-PM-PVH polymer membrane was 200 °C and is sufficient for the application purpose. XRD and DSC analysis evidenced the reduction of crystallinity of the PE-PM-PVH polymer membrane. The ionic conductivity (σ) of the PE-PM-PVH membrane is 0.81 mS cm^{-1} and is higher than pristine P(VDF-HFP) which has 0.25 mS cm^{-1}. The temperature-dependent conductivity shows three regions: (1) 0–10 °C, (2) 10–50 °C, (3) 50–60 °C and shows Vogel–Tammann–Fulcher (VTF)/Arrehenius behavior. The first region shows a decrease in conductivity and is attributed to the slow segmental motion of polymer chain and poor ionic mobility. The second region shows the increase in conductivity and is due to the better salt dissociation. The third region (high-temperature region) displays the enhanced segmental motion of the polymer chain and reflects the enhanced conductivity. The Li^{+} transport number (t_{Li}^{+}) of PE-PM-PVH polymer membrane was higher (0.72) than the pristine P(VDF-HFP) membrane (0.29). The voltage stability window of the PE-PM-PVH polymer membrane was higher (~ 5.0 V) than the pristine P(VDF-HFP) membrane (~ 4.5 V). The PE-PM-PVH polymer membrane was used to fabricate the battery, and it displays the initial discharge capacity of about 152.7 mAh g^{-1} (and after 100 cycles discharge capacity remains 149.6 mAh g^{-1}). The capacity retention of 98% and Coulombic efficiency about 99% strengthens the suitability for commercial applications. It needs to be noted that the PE-PM-PVH polymer membrane-based battery shows improved cyclic stability than the pristine P(VDF-HFP) membrane-based battery. The rate performance of the PE-PM-PVH polymer membrane-based battery shows discharge capacity as follows: 149.5 mAh g^{-1} (@ 0.1 mA cm^{-2}), 148.7 mAh g^{-1} (@ 0.2 mA cm^{-2}), 146.9 mAh g^{-1} (@ 0.3 mA cm^{-2}), 144.7 mAh g^{-1} (@ 0.4 mA cm^{-2}), 143.1 mAh g^{-1} (@ 0.5 mA cm^{-2}), and 137.7 mAh g^{-1} (@ 1.0 mA cm^{-2}). The rate performance of the PE-PM-PVH polymer membrane-based battery was also superior to pristine P(VDF-HFP) membrane-based battery.

Recently, Smith et al. [155] have investigated the role of ceramics (OPSZ; organopolysilazanes) with having different morphologies (*same chemical backbone but differ on the ratios of the tetraethyl orthosilicate (TEOS) pendant chain attached to the polysilazane (PSZ) backbone*) in altering the properties of PAN polymer and electrospinning method was used for preparation. SEM analysis showed the decrease in fiber diameter with TEOS ratio (660 ± 81 nm → 490 ± 69 nm), pore size distribution (619 ± 76 nm → 463 ± 72 nm), and electrolyte uptake increases (801 ± 75%→1109 ± 32%). The mechanical properties were superior for the 40 wt% TEOS: PSZ system. Both DSC and XRD analyses indicate the reduction in crystallinity with TEOS content. The highest ionic conductivity was 1.04 ± 0.05 mS cm^{-1} for 40 wt% TEOS:PSZ system. The enhancement in the conductivity was attributed to the better salt dissociation and improved amorphous phase. It may be noted that the smaller pore size reflects the large electrolyte uptake and hence the highest ionic conductivity for the 40 wt% TEOS: PSZ system. All system displays a similar initial discharge capacity, 134 mAh g^{-1}, but after 100 cycles the capacity retention varies as follows: 93% for 40 wt% TEOS:PSZ, 91% for 20 wt% TEOS:PSZ and 88% for 0 wt% TEOS:PSZ (Fig. 27e, f).

A cross-linked GPE porous fabric membrane (XSAE) was introduced by Tsao et al. [156]. Here, XSAE (*x*–*y*) is, *x* represents the PDMS–hybrid membrane weight ratio, while y denotes the acrylonitrile–ethylene oxide molar ratio. They introduced the PDMS into the cross-linked PAN/PEO polymer electrolyte to improve the electrolyte uptake and cation transference number. DSC and FESEM analyses evidenced the phase separation of hybrid polymer and porous morphology. It is important to note that the pore size increases with the addition of PDMS and indicates large electrolyte uptake. The highest electrolyte uptake was 85.1% for XSAE (20–1.5). XRD analysis indicates the reduction in crystallinity and is attributed to the incorporation of the sterically hindered PAN moieties in the main chains. This disrupts the crystalline arrangement of chains and is responsible for the high ionic conductivity and cation transference number as discussed below. The highest ionic conductivity is 0.67 mS cm^{-1} at 30 °C and is attributed to the largest electrolyte uptake. The cation transference number was 0.58 and is attributed to the increases segmental motion of PAN with the addition of PDMS. The voltage stability window was close to 4.5 V. XSAE (20–1.5) hybrid membrane was selected to fabricate the cell and delivers a high discharge capacity of about 154 mAh g^{-1} (@ 0.1 C) and 145 mAh g^{-1} (@ 1 C). This cell displays higher energy density as compared to the XAE system (PDMS free). It was concluded that the above approach may be adapted to develop the electrolytes for high energy density batteries.

A number of strategies are adopted to enhance the characteristics parameters of the Li-ion battery, but still, the room is there to enhance them. The network structure of the LLTO may affect the ion dynamics parameters. So, a three-dimensional (3D) LLTO network is investigated by Wang et al. [157]. The unique feature of this approach is: (1) Interconnected LLTO effectively enhances the electrical and mechanical properties as well as suppresses the dendrite growth and (2) a Combination of hot press and quenching process results in the formation of dense and self-standing CPE. The composite polymer electrolyte comprises PEO as host matrix, LiTFSI as salt, and three-dimensional (3D) LLTO nanofiber network (synthesized the first time). The highest conductivity value was about 1.8×10^{-4} S cm^{-1} at RT, cation transport number (t_+) 0.33, and voltage stability window of about 4.5 V versus Li/Li^+. The addition of LLTO results in enhancement of mechanical properties (tensile strength = 16.18 MPa, Young's modulus = 0.98 GPa, elongation = 200%). A comparative constant current galvanostatic cycles are shown for the SPE and 3D-CPE. It may be noted that for Li | SPE | Li cell, fluctuating voltage of 2 V is observed, while for Li | 3D-CPE | Li cell only a small voltage is observed. The excellent stability is observed for the 3D-CPE-based cell up to 800 h (Fig. 28a). This evidences the superiority of the interconnected LLTO. Figure 28b, c shows the cyclic stability plot and charging/discharging profile for 30 cycles of cells operated at 25 °C.

LATP has gained the attention of researchers as a solid-state ionic conductor due to its high ionic conductivity (~ 1 mS cm^{-1}) and low sensitivity against an oxygen/moisture atmosphere [158]. But, one drawback with LATP is that it degrades with Li metal contact owing to the reduction from Ti_4^+ to Ti_3^+ which results in the formation of the resistive path for cation migration, i.e., Li^+. So, to resolve this one of the key interfacial issues, the LATP particle is coated with a polymer electrolyte. The advantages with this approach are: (1) Prevention of polymer electrolyte decomposition due to the blockage of anion by ceramic layer will be reflected in Coulombic efficiency also, (2) intrinsic ability of polymer to block electron transport will improve the voltage stability window, and (3) desirable interface is formed which also prevents external reaction [146, 159]. Recently, Yu et al. [160] have reported the preparation of a novel electrolyte by coating the $Li_{1.3}Al_{0.3}Ti_{1.7}(PO_4)_3$ (LATP) nanoparticle with polyphosphazene/PVDF-HFP/LiBOB, and it provides improved chemical, mechanical, interfacial and electrochemical

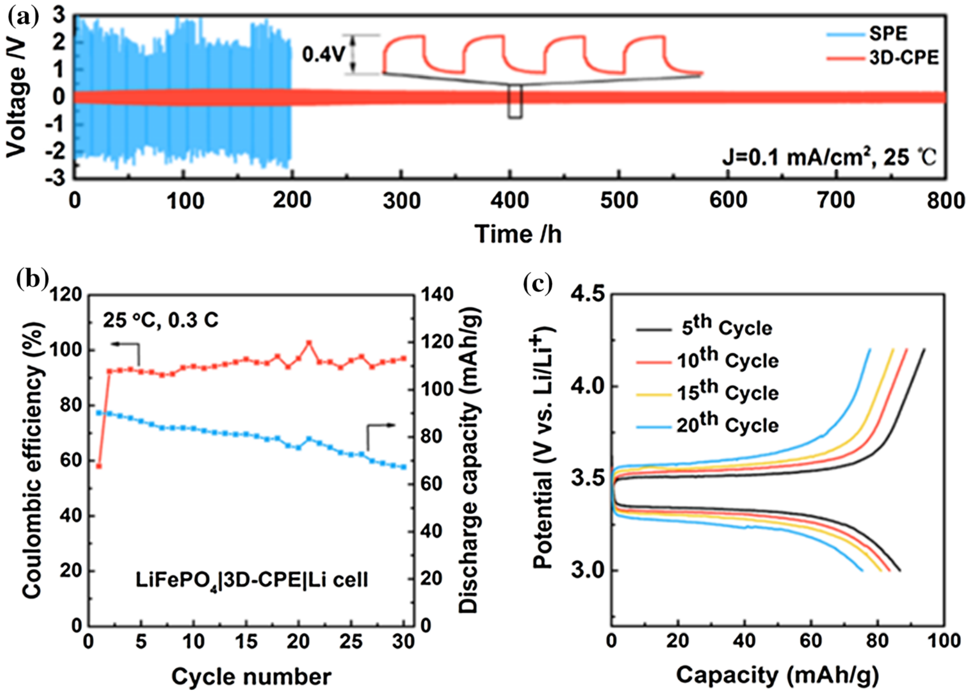

Figure 28 **a** Voltage profiles of Li plating and stripping cycling for the SPE and 3D-CPE. The inset shows four cycles for the Li|3D-CPE|Li cell, **b** cycling performance at 0.3 C-rate and, **c** typical charge–discharge curves of a coin-type cell $LiFePO_4$|3D-CPE|Li operated at 25 °C (Reproduced with permission from Ref. [157], © American Chemical Society 2018).

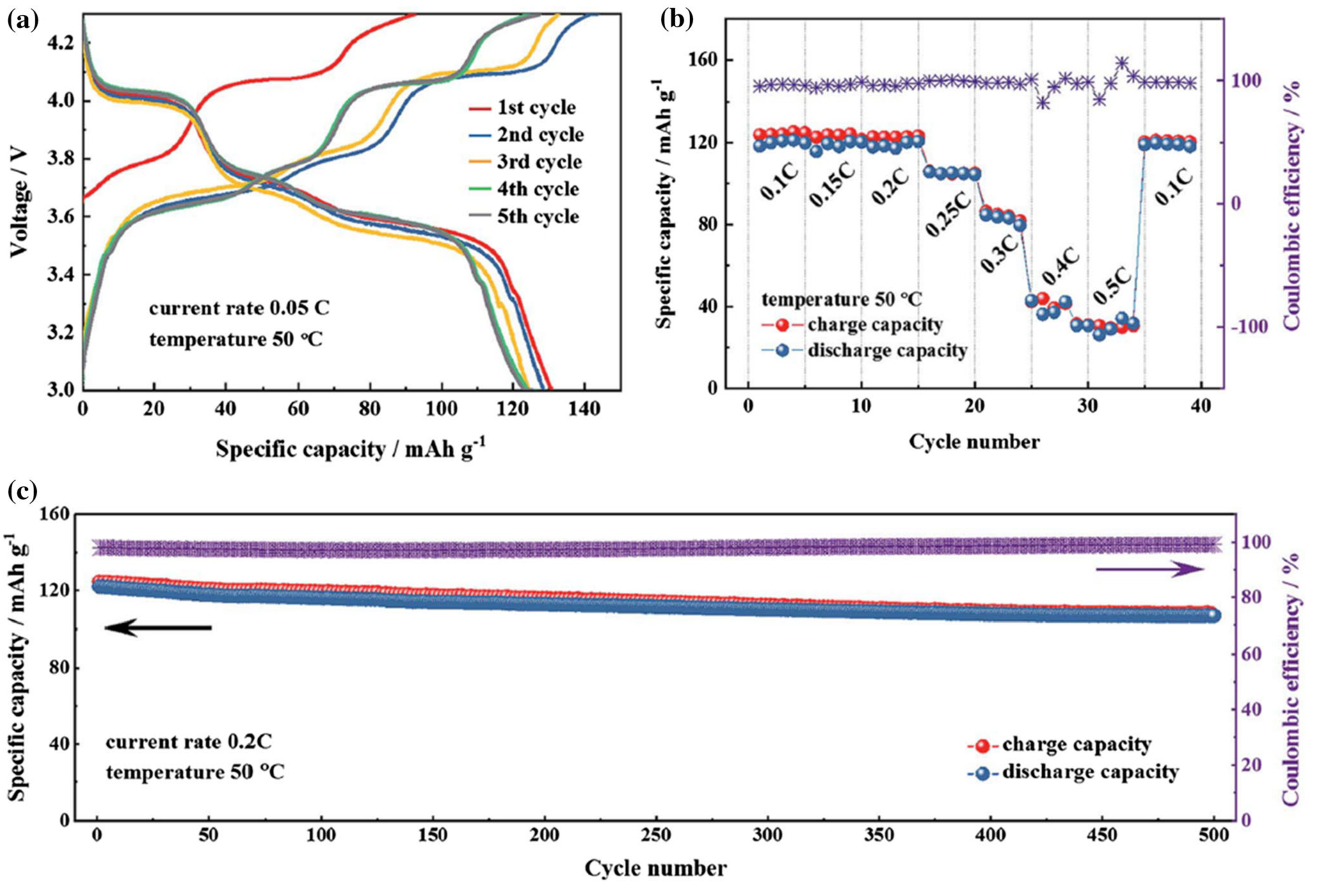

Figure 29 Electrochemical performance of the Li|layered hybrid solid electrolyte|$Li_3V_2(PO_4)_3$/CNT all-solid-state lithium battery at 50 °C in the voltage range of 3.0–4.3 V versus Li/Li^+: **a** charge–discharge curve of the initial five cycles at a current rate of 0.05 C, **b** rate capability at current rates from 0.1 to 0.5 C, respectively, and **c** long-term cycling measurement at a current rate of 0.2 C (Reproduced with permission from Ref. [160] © The Royal Society of Chemistry 2019).

properties. The maximum voltage stability window was about 4.7 V. The electrochemical performance of the layered hybrid solid electrolyte, Li | LHSE | $Li_3V_2(PO_4)_3$/CN. Figure 29a shows the charge–discharge profile for the cell at the current rate of 0.05 C. The initial discharge capacity is about 130.5 mA hg^{-1}, and three plateaus are obtained associated with the three reversible phase transitions of $Li_3V_2(PO_4)_{3}4LiV_2(PO_4)_3$. A tiny plateau associated with $LiFePO_4$ impurity is also observed. Figure 29b shows the rate capability plot and at the high current rate (> 0.2 C), a rapid drop in discharge capacity. Figure 29c shows the cycling stability of the cell for 500 cycles. After 500 cycles, the discharge capacity is about 107.6 mAh g^{-1} with a capacity retention of 88.2%. The gravimetric energy density of about 460 Wh kg^{-1} is obtained for the cell and is almost comparable to the LIBs with liquid electrolyte. The present battery possesses various advantages over the other LATP base battery. The key advantages are: (1) no need to of high pressure for making contacts, (2) broad voltage stability window and operation range, and (3) no chance of LATP decomposition. It was concluded that this strategy may be a game-changer for developing new all-solid-state batteries.

Cross-linked solid polymer electrolyte

Kwon et al. [161] reported the preparation of organic/inorganic hybrid semi-interpenetrating network (semi-IPN) polymer electrolytes (HIPEs) based on poly (ethylene oxide-ethylene carbonate) (PEOEC) as the polymer matrix and $LiClO_4$ salt. The effect of the octa-functional POSS acrylate (OA-POSS) has been investigated on the HIPE properties. Here, POSS stands for polyhedral oligomeric silsesquioxane. The polymer salt system with $[LiClO_4]/([EO] + [EC])$ ratio 0.15 exhibits the highest ionic conductivity of about 4.48×10^{-5} S cm^{-1}. All the HIPE system was thermally stable up to 175 °C. Addition of OA-POSS increases the conductivity and is about 3.74×10^{-5} S cm^{-1} (@ 30 °C) and 3.26×10^{-4} S cm^{-1} (@ 60 °C). Figure 30a shows the voltage stability window of the prepared HIPE and is close to 5.0 V. Figure 36b shows the electrochemical performance in voltage range 2.0–4.0 V of the cell configuration V_2O_5/L-HIPE10/lithium metal. The initial discharge capacity is 280 mAh g^{-1} and shows good retention of up to 30 cycles (Fig. 30b).

Shin et al. [162] prepared the cross-linked composite polymer electrolyte (CLCPE) based on methacrylate-functionalized SiO_2 (MA-SiO_2) nanoparticles, PAN membrane and gel electrolyte precursor containing tri(ethylene glycol) diacrylate (TEGDA). Figure 30c compares the Li-ion migration in the non-porous and mesoporous SiO_2 nanoparticles. Both have a spherical morphology, and the average diameter is about 35 nm. The latter one has the intra-connected pore network structure that facilitates the Li-ion migration. The ionic conductivity of the CLCPE with non-porous MA-SiO_2 particles and mesoporous MA-SiO_2 particles is 1.1×10^{-3} and 1.8×10^{-3} S cm^{-1}, respectively. The highest conductivity is due to porosity in MA-SiO_2 nanoparticles. The electrochemical performance is examined in the range of 3.0–4.5 V, by fabricating the cell with configuration graphite as a negative electrode and $LiNi_{1/3}Co_{1/3}Mn_{1/3}O_2$ as a positive electrode with a composite electrolyte. The initial discharge capacity is about 179.5 mAh g^{-1} and decreases to 157.9 mAh g^{-1} after 300 cycles with a capacity retention of 88.0% (for mesoporous MA-SiO_2). The good cyclability is attributed to the good interfacial contact with electrodes. Figure 30d shows the voltage profile for the cell with MA-SiO_2 and shows a capacity of about 142.7 mAh g^{-1} at a 5.0 C rate, while Fig. 30e shows the plot of discharge capacity at a different current rate. The authors concluded that the mesoporous SiO_2-based cell shows improved performance for all current rates.

The effect of cross-linker on the properties of the solid polymer electrolyte is not studied. So, keeping this in mind Youcef et al. [114] reported the preparation of the cross-linked polymer electrolyte (CLPE) by UV-induced cross-linking of poly (ethylene glycol) diacrylate (PEGDA) and divinylbenzene (DVB) within a poly (ethylene oxide) (PEO) matrix. The DSC analysis showed the lowering of the crystallinity and melting with the addition of cross-linker. There was no effect of the DVB on the conductivity and 10% DVB ionic conductivity (1.4×10^{-4} S cm^{-1}) was usable for practical applications at 60 °C. The voltage stability window of the electrolyte was close to 5.0 V. The cation transference number was 0.23 and is within the desirable limit. The cycling performance was examined by fabricating the cell with configuration $LiFePO_4$/SPE with 10% DVB/Li metal. The fabricated cell shows the initial discharge capacity of 123 mAh g^{-1} which increases to 130 mAh g^{-1} after 5 cycles and increases to 138 mAh g^{-1} after 20 cycles.

Recently, Zhang et al. [163] have prepared the new class of free-standing cross-linked hybrid polymer electrolytes (HPEs) with POSS as the cross-linker. The HPE has been prepared by the one-step free radical polymerization reaction. The HPE system with 5 wt% POSS shows the highest ionic conductivity of 3.94×10^{-5} S cm^{-1} (@ 25 °C) and increases to 1.39×10^{-3} S cm^{-1} (80 °C). The enhancement in the conductivity with the addition of POSS is attributed to the enhanced free volume for cation migration. Another reason given by the authors was that the grafted EO chains on POSS particles create new ion conduction pathways. At high POSS, content decrease is due to the decrease in free volume due to more POSS particles. The electrochemical properties were investigated on the cell $LiFePO_4$/HPE + 5 wt% POSS/Li, and an initial discharge capacity is about 154 mAh g^{-1}. After 150 cycles, the discharge capacity is 152.1 mAh g^{-1} with a capacity retention of 88%. A very high Coulombic efficiency 99% strengthens the use of HPE in practical batteries.

Another report by Zhang et al. [164] demonstrated the preparation of flexible cross-linked SPE with PEO, TEGDMA, and TEGDME (PTT) SPE with LiTFSI salt. In this work, the electrode/electrolyte composite has been prepared by in situ UV-derived dual-reaction to minimize the interfacial resistance and low molecular weight cognate monomers have been introduced to enhance the conductivity and reduce the crystallinity. The prepared PTT-SPE membrane is transparent and flexible, and the benefits of this will be reflected in electrical properties. The PTT-SPE membrane exhibits ionic conductivity of about 0.27 mS cm^{-1} and is 30 times higher than PEO-SPE. The cation transport number is also higher and is about 0.56 and is favorable in the elimination of polarization. The voltage window of the PTT-SPE is about 5.38 V. The electrochemical performance has

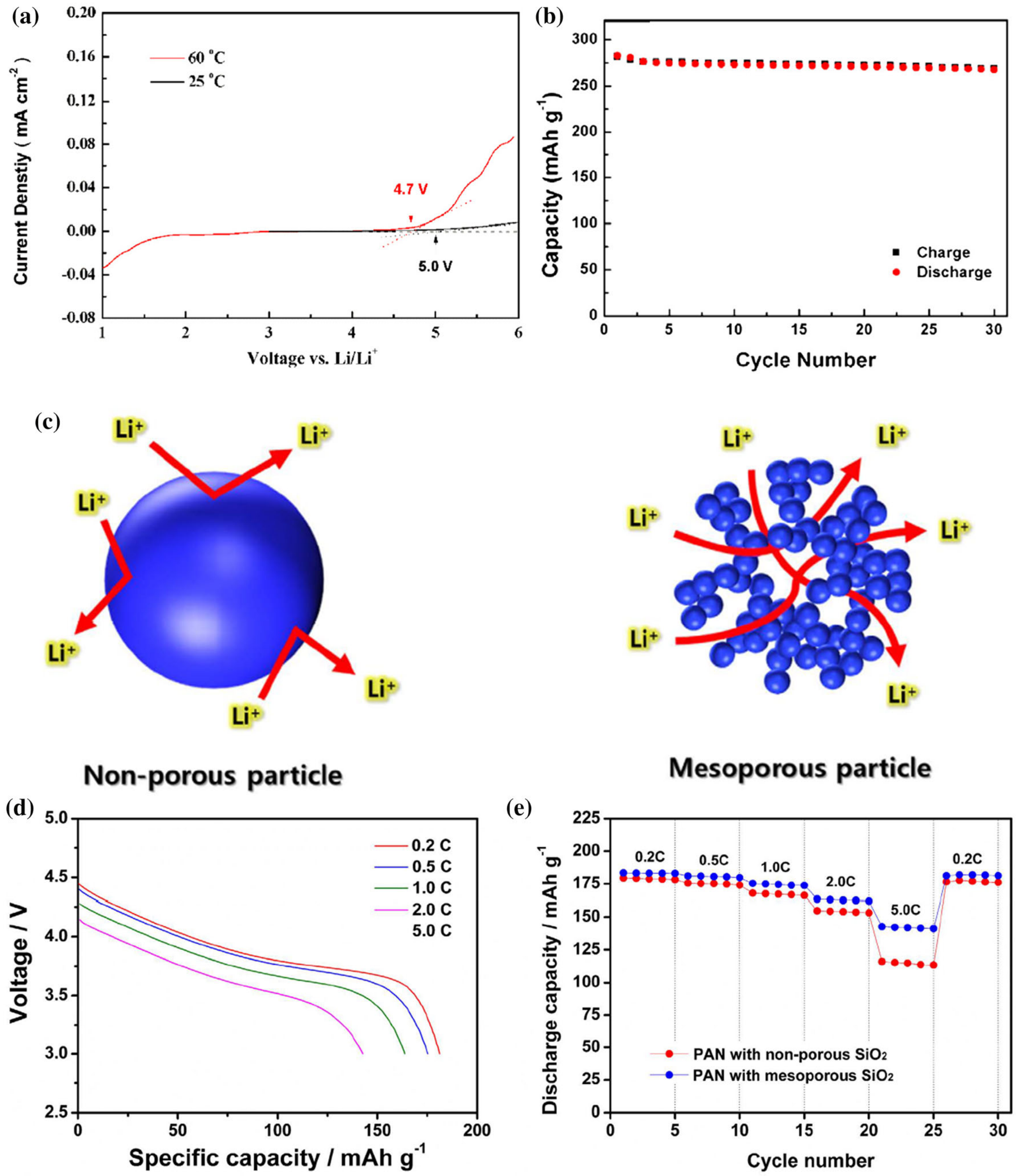

Figure 30 **a** Linear sweep voltammograms of stainless steel electrodes in L-HIPE10 with $LiSO_3CF_3$ at 25 °C and 60 °C, and **b** discharge cycle stability (current density: 0.1 C) of all-solid-state Li/L-HIPE10 (with $LiSO_3CF_3$)/V_2O_5 cells at 60 °C (Reproduced with permission from Ref. [161] © Elsevier 2014), **c** different lithium-ion transport behavior when employing non-porous MA-SiO_2 particles and mesoporous MA-SiO_2 particles in the cross-linked composite gel polymer electrolyte, **d** discharge curves of lithium-ion polymer cell assembled with cross-linked composite gel polymer electrolyte employing mesoporous MA-SiO_2 particles, and **e** discharge capacities of lithium-ion polymer cells assembled with different electrolytes as a function of C-rate (Reproduced with permission from Ref. [162] © 2016).

been evaluated by fabricating LFP/PTT-SPE/Li cells and an initial discharge capacity is about 160 mAh g^{-1} at 0.05 C. The cyclic stability is good for 100 cycles (Fig. 31i). Even after 100 cycles, high capacity retention of about 98.8% confirms the desirable performance of cells sing PTT-SPE. Further, the mechanical test of the fabricated cell was performed by glowing LED in three conditions, free-bending,

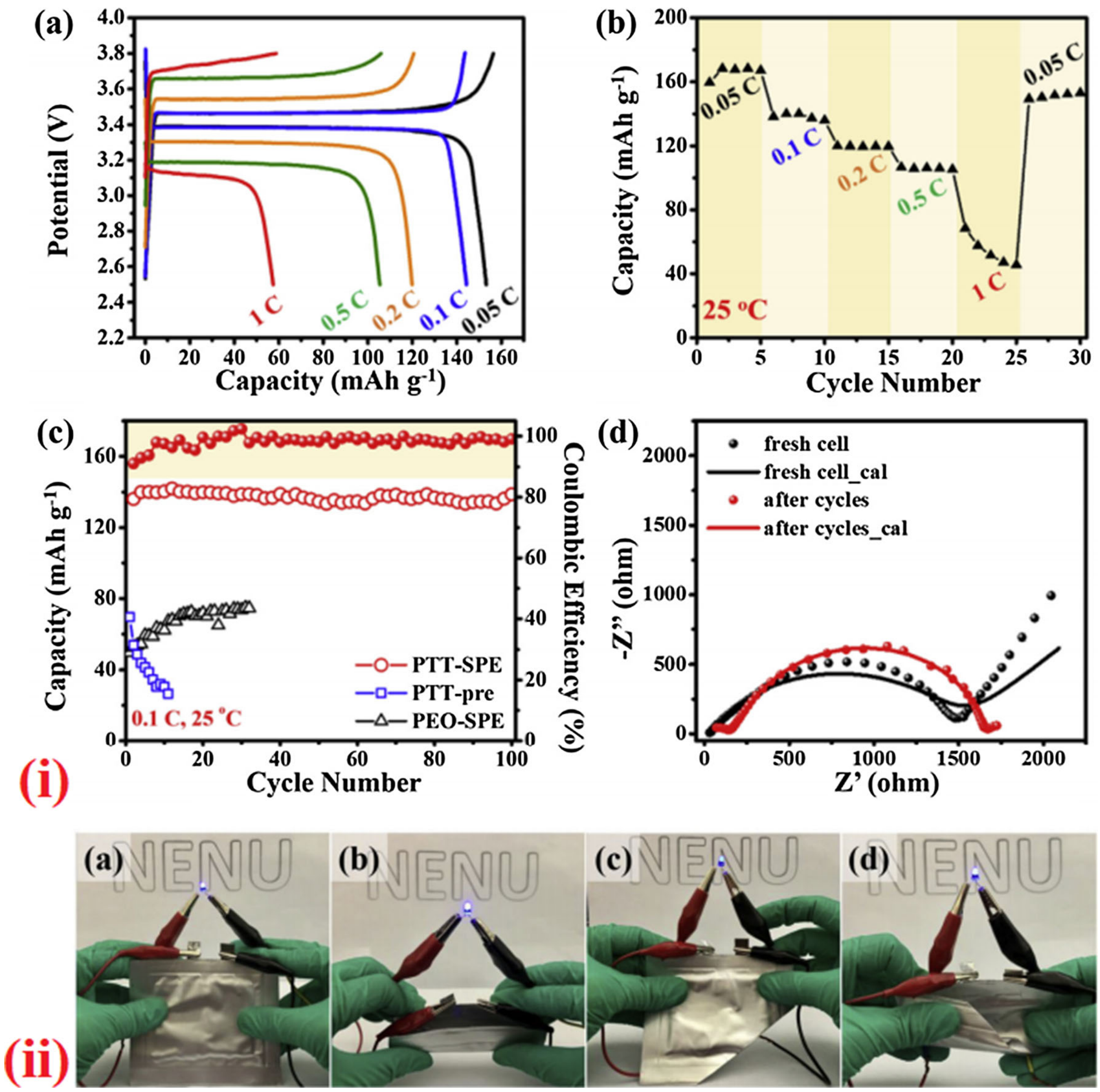

Figure 31 **i** LFP//Li cell performances: (a) Representative charge/discharge profiles, (b) cycle performances at different rates with PTT-SPE, (c) the long-term cycle performances of PTT-SPE, PTT-pre (without UV irradiation) and PEO-SPE at 0.1C, (d) the EIS tests of a cell with PTT-SPE before and after 100 cycles at 0.1C. **ii** Photographs for the LFP/PTT-SPE/Li soft package full cell that powers a blue LED under various condition: (a) free-bending, (b) bending, (c, d) cutting (Reproduced with permission from Ref. [164] © Elsevier 2019).

bending, and after cutting (Fig. 31ii). In conclusion, the prepared SPE has the potential to use it in commercial energy storage/conversion devices.

Soy protein-based solid polymer electrolyte

It is well known that the addition of nanofiller is an attractive approach to enhance the electrochemical properties. The addition of nanofiller effectively promotes the ion dissociation and creates ion-conducting pathways to the cation. However, still, there are restrictions to the enhancement of the conductivity up to the desirable limit, since the availability of huge surface area is the intrinsic property of the nanofiller and is the key behind their selection. So, an alternative that seems to be feasible is the surface functionalization of the nanofiller that will facilitate the desirable ion conduction. The soy protein is an attractive candidate owing to the ability to transfer the cations via the functional group present in it [165]. The availability of the ion conduction pathways or their numbers is directly linked with the active surface area. One unique advantage with modification is that the interaction between the polymer host and ion can be tuned. Modification of nanofiller with SP reduces the nanofiller agglomeration tendency.

Fu et al. [117] investigated the protein-based solid conductor by adding $LiClO_4$ salt in the denatured soy protein. The increase in ionic conductivity with temperature from ~ 10^{-9} to 10^{-5} S cm^{-1} is observed. The Li^+ transference number is 0.94 and confirms the ionic nature of PIC. Also, the modulus was higher as compared to the pure PEO electrolyte. Here, the cation migration occurs via the hopping process by coordinating sites provided by protein backbone oxygen atoms. Here, anions remain immobilized and remain interacted with a positive charge in the protein side group.

Another report by the same group demonstrates the manipulation of protein configuration by nanofiller, and it shows effective enhancement in the ionic conductivity and mechanical properties. Fu et al. [166] reported the preparation of the solid polymer electrolyte by the modification of SP with TiO_2 nanoparticles, i.e. protein-ceramic hybrid nanofiller. The two types of hybrid nanofiller are: (1) TiO_2-(SP-close) hybrid and (2) TiO_2-(SP-open) hybrid. The morphological analysis evidenced the decrease in particle size, while some agglomeration was there with untreated TiO_2. Protein treatment was effective in enhancing the dispersion and compatibility with the polymer matrix. The highest ionic conductivity was exhibited with 5 wt% TiO_2/(SP-open) hybrid nanofiller and is about 6×10^{-5} S cm^{-1}. Figure 32a shows the temperature-dependent ionic conductivity,

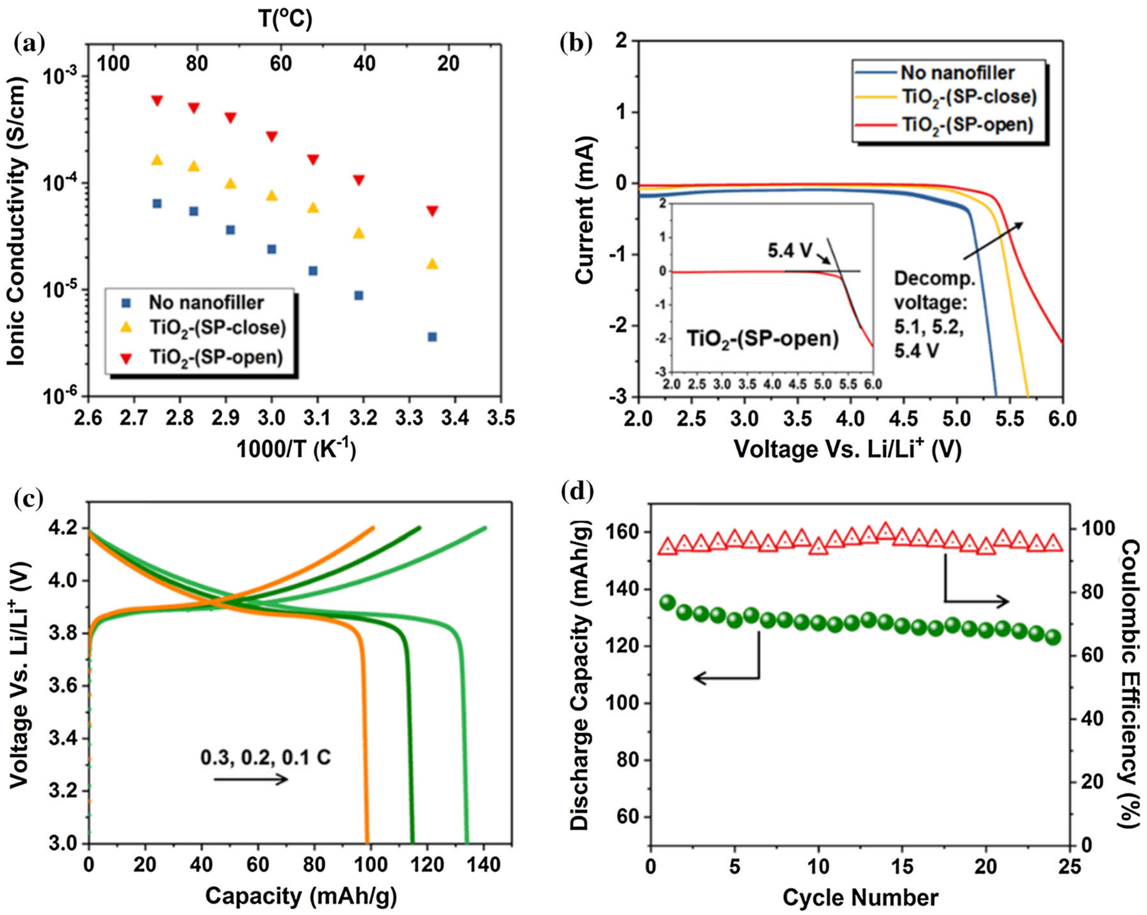

Figure 32 **a** Arrhenius plots of ionic conductivity of CPEs with the TiO_2/SP hybrid nanofillers as compared with the pure PEO–$LiClO_4$ electrolyte; **b** electrochemical stability studies of the CPEs as compared with the pure PEO–$LiClO_4$ electrolyte; **c** discharge–charge profiles of $LiCoO_2$/CPE–TiO_2/(SP-open) hybrid/Li cells with varying C-rates tested at 65 °C; **d** cycle performance and Coulombic efficiency of $LiCoO_2$/CPE–TiO_2/(SP-open) hybrid/Li cells at 0.1 C tested at 65 °C (Reproduced with permission from Ref. [166] © American Chemical Society 2018).

and for the TiO_2/(SP-open) conductivity is comparable to liquid electrolyte at 90 °C i.e. 7×10^{-4} S cm^{-1}. The voltage stability window is very high, 5.2 V for TiO_2/(SP-close)–CPE and 5.4 V for TiO_2/(SP-open)–CPE (Fig. 32b). Figure 32c, d shows the electrochemical performance of the cell configuration $LiCoO_2$/CPE–TiO_2/(SP-open)-hybrid/Li. Figure 32c shows the performance with the different current rates, and Fig. 32d shows the variation of discharge capacity and Coulombic efficiency at 0.1 C. The discharge capacity decreases from 135 to 128 mAh g^{-1} after 24 cycles with Coulombic efficiency of 95%. Another interesting parameter is that the traditional charger transfer resistance is lowest for the 5 wt% TiO_2/(SP-open) hybrid nanofiller system. SP coating on the TiO_2 surface improves the nanofiller dispersion and flexibility. In the CPE matrix, two possible interactions occur: (1) cation interaction with backbone oxygen in protein and (2) formation of anion clusters owing to the presence of electrostatic interactions between anion and positive charge side groups (e.g., Lys and Arg) of protein. It may be concluded that the modification of nanofiller with SP creates new ion conduction channels.

The two important factors that influence the cation dynamics are (1) protein configuration and (2) protein–TiO_2 interaction. Both of these parameters can be tuned by tuning the protein treatment conditions, and it effectively alters the ion migration. The positively charged amino side group in the SP interacts with the anion of the salt, and it enhances the enhanced number of cation contributing to the conductivity. Another report by Fu et al. [167] highlights the preparation of the core–shell protein@TiO_2 hybrid NWs, and their effect on the solid polymer electrolyte [pure ultrahigh-molecular-weight PEO; UHMWPEO-$LiClO_4$] is examined in detail. The growth of protein coating on the TiO_2 nanowire is evidenced by an increased diameter from 221 to 246 nm. The thickness of the protein coating is approx. 8 nm as evidenced by HRTEM. The XRD diffractograms of SP and TiO_2 nanowire concluded that both the SP and TiO_2 NW are integrated well, and also there is a decrease in peak intensity of crystalline TiO_2 NW. It infers that SP coating enhances the amorphous phase that is a very critical requirement for fast ion transport. Further, the interactions between the SP and TiO_2 NW have been examined by FTIR and strong interactions between the –NH group of SP and TiO_2 NW as evidenced by the disappearance of N–H stretching (amide III) located at 1238 cm^{-1}. FTIR spectra confirm the interaction between the positively charged amino side group and the oxygen has a negative charge of TiO_2. It results in the in situ growth of the protein layer on the TiO_2 surface (SP@TiO_2). The addition of salt in the UHMWPEO polymer matrix disrupts the crystallization attributed to the cation coordination with the oxygen of polymer. The highest ionic conductivity was exhibited by the CPE with core–shell SP@TiO_2 NWs and is about 1.1×10^{-4} S cm^{-1} (@ 10 wt% SP@TiO_2 loading). This conductivity value is larger than the SP-TiO_2 nanoparticles-based composite electrolyte. This enhancement is attributed to the high surface area of the nanowire and the high aspect ratio which creates continuous conducting paths. The conductivity increases with temperature and reaches 2×10^{-3} S cm^{-1} (At 80 °C). The highest voltage stability window is obtained for the 10 wt% SP@TiO_2-based composite polymer electrolyte and is about 5.3 V. The cation (Li^+) transference number is very high for the 10 wt% SP@TiO_2-based composite polymer electrolyte and is 0.62 which is higher than the pure PEO ($t_{Li}^{+} = 0.41$). The electrochemical performance of the cell-based on CPEs with SP@TiO_2 NWs was examined at 65 °C. The initial discharge capacity is 135 mAh g^{-1} at 0.2 C current rate and decreases to 111 at 1 C current rate (Fig. 33a, b). It was concluded that the cell comprising composite polymer electrolytes with SP@TiO_2 NWs shows the highest capacity and capacity retention of 94.7% after 70 cycles is witnessed (Fig. 33c). The Coulombic deficiency is about 98.6%.

Ion transport mechanism

In solid polymer electrolytes, an alkali metal salt is dissolved in the polymer matrix and the salt gets dissociated in the cation and anions owing to the electrostatic interactions. The cation migrates via the coordinating sites provided by the polymer chain and anion due to large size is immobilized with the polymer backbone. The combined effect of the hopping and segmental motion results in ion transport. In the case of the polymer salt matrix, the ion transport mechanism is shown in Fig. 34. The four possible processes are: (1) intrachain hopping, (2) interchain hopping, (3) intrachain hopping via ion

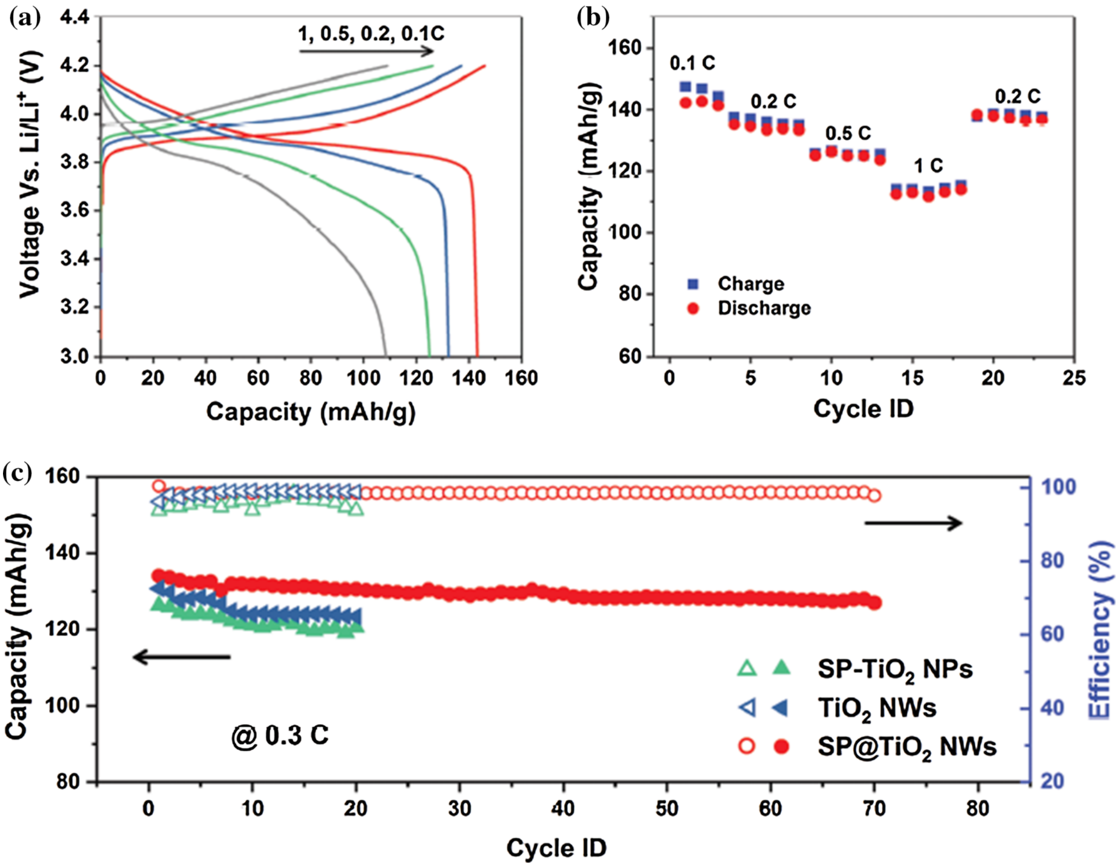

Figure 33 Electrochemical performance of symmetric Li/CPE/Li cells and $LiCoO_2$/CPE/Li half-cells. **a** Voltage profiles of half-cells with CPE loaded with 10 wt% SP@TiO_2 NWs at various current rates. **b** C-rate performance of half-cells with CPE loaded with 10 wt% SP@TiO_2 NWs. **c** Cycle stability of half-cells with CPEs loaded with 10 wt% SP@TiO_2 NWs, SP–TiO_2 NPs, and TiO_2 NWs tested at 0.3 C. All the measurements were performed at 65 °C (Reproduced with permission from Ref. [167] © John Wiley and Sons 2015).

Figure 34 Mechanism of ion transport in PEO (Reproduced with permission from Ref. [21] © Royal Society of Chemistry 2015).

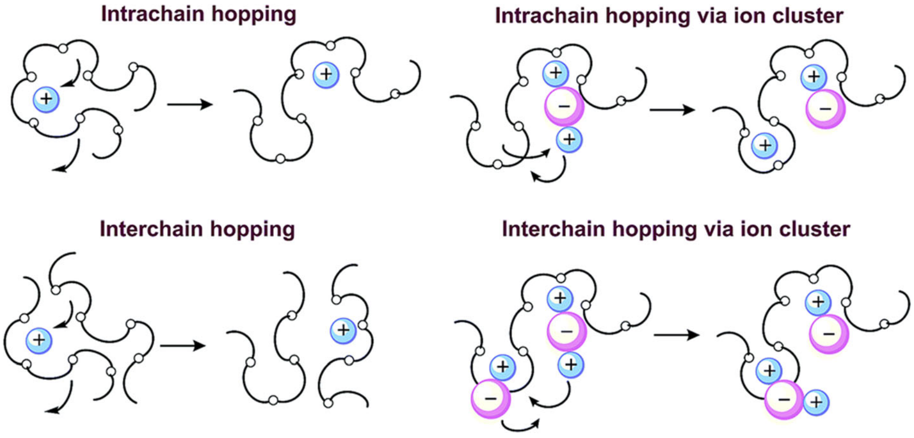

cluster, and (4) interchain hopping via ion cluster [21, 168].

The ion migration in different composite polymer electrolytes of three types is shown in Fig. 35i(a–c). The LLZTO is added in the polymer matrix, and it plays three important roles: (1) enhances the segmental motion of polymer chains, (2) lowers the crystalline content, and (3) increases conductivity by providing additional conducting paths [132]. Nanoparticles play an effective role in the

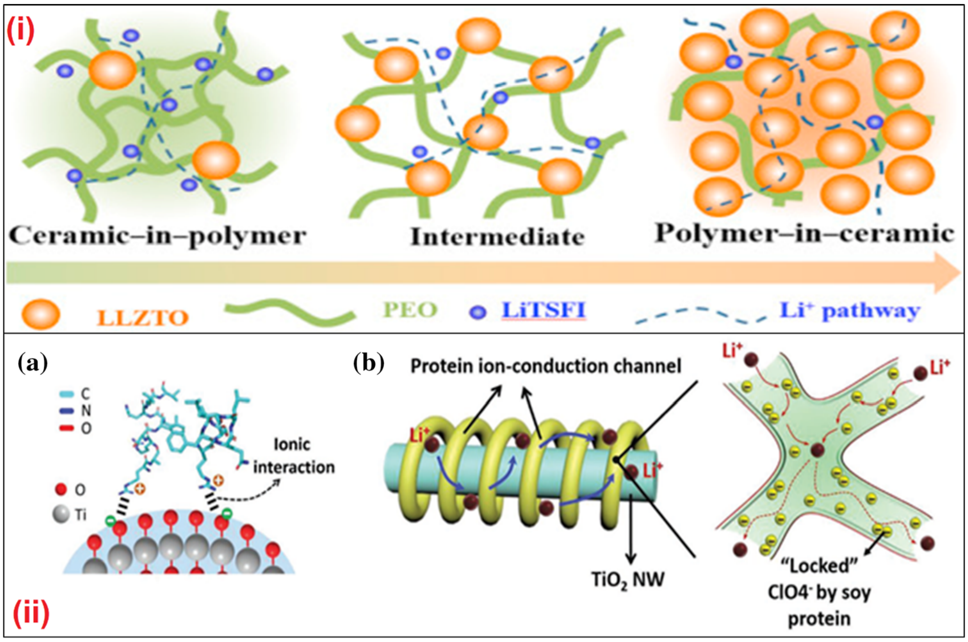

Figure 35 **i** Schematic illustration for PEO-LLZTO CSE: (a) "ceramic-in-polymer"; (b) "intermediate"; (c) "polymer-in-ceramic (Reproduced with permission from Ref. [161] © Elsevier 2018), **ii** (a) schematic of the possible mechanism for the TiO_2/(SP-open) hybrid to improve the adhesion of the CPEs (Reproduced with permission from Ref. [166] © American Chemical Society 2018), (b) schematic illustration of protein ion conduction channel promoting dissociation of lithium salts and conduction of Li^+. Loading of nanofillers in all CPEs: 10 wt% (Reproduced with permission from Ref. [169] © John Wiley and Sons 2015).

enhancement of the ionic conductivity and the ion dynamics in the polymer matrix. In the case of soy protein (SP)-based ion conductor, the protein chain having functional groups in the backbone supports the salt dissociation and enhances the ion migration. So, the combination of these two approaches will be more efficient in promoting ion dynamics and modified nanoparticle will be more effective [166]. Figure 35ii shows the protein–ceramic hybrid nanofiller that enhances the ionic conductivity in solid polymer electrolytes. So, here protein structure is manipulated using ceramic TiO_2 nanoparticle. The optimized protein on the nanoparticle shows various interactions at the protein nanoparticle interface since protein backbone has various functional groups that provide strong interaction to substrate surface, such as charge–charge interactions, hydrogen bonding, van der Waals force, and π–π interactions [169].

In continuation to the above approach, Fu et al. [167] modified the nanowire with protein configuration (core–shell protein@TiO_2 hybrid NWs). The unique feature with this approach was the continuous conduction pathways that facilitate the fast ion conduction. Figure 35 ii shows the ion conduction and the protein interaction with ions in the core–shell protein@TiO_2 hybrid NWs. The functional group present in the protein backbone locks the anion owing to the electrostatic interaction by positively charged amino acid residues. It results in better salt dissociation, and single-ion conductor is obtained, i.e. conduction is dominated by the cation only. Another possible mechanism is that the locked anions clusters and oxygen in the protein backbone provide coordinating sites for cation hopping and a favorable conduction environment is available. It may be concluded that the protein chain is effective in enhancing ion dynamics.

The ion migration in the ceramic-polymer electrolyte is influenced by the hierarchical structures of nanofiller. In this approach, a 3-D nanofiller is obtained to avoid particle agglomeration. One advantage with the nanofiller framework is that it provides continuous pathways for cation migration. Figure 36i shows the ion migration in such a 3-D framework of LLTO. The agglomeration of the nanoparticles decreases the degree of percolation along with interphase volume. This results in a decrease in conductivity owing to the discontinuous

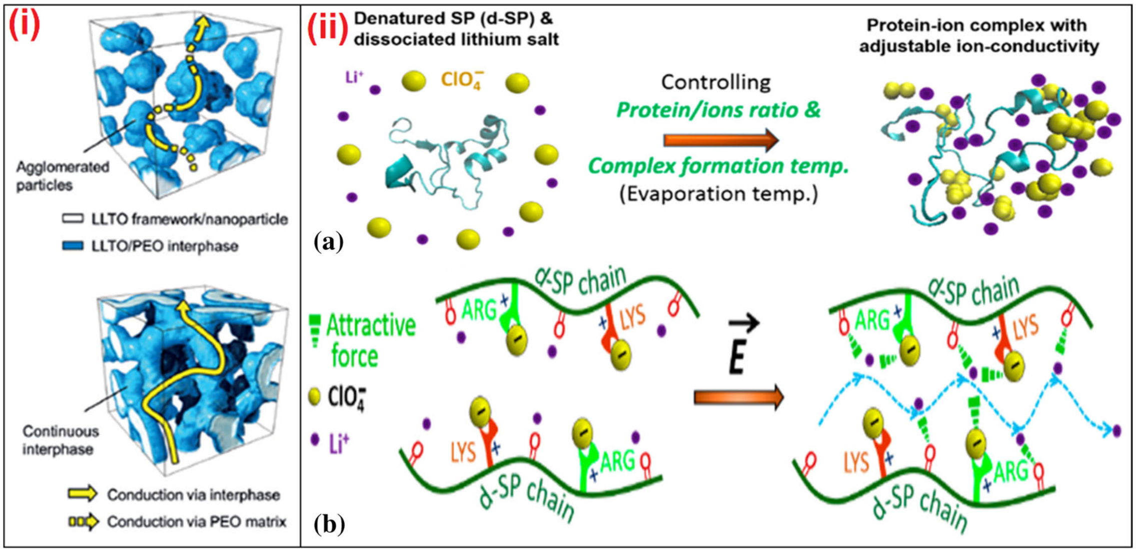

Figure 36 **i** Schematic representation of possible conduction mechanism in composite electrolytes with agglomerated nanoparticles and 3D continuous framework (Reproduced with permission from Ref. [126], © John Wiley and Sons 2018), **ii** Ionic conductivity of protein-based ion conductor (PIC) at room temperature, (a) schematic of the control of a protein–ion complex by adjusting protein/ion ratio and complex formation temperature, (b) schematic illustration of the decoupled Li^+-transportation process. The hopping of Li^+ ions is facilitated by the anions, which are strongly locked by the protein through positively charged side chains (Reproduced with permission from Ref. [117] © American Chemical Society 2016).

path, while the composite polymer electrolyte based on the hydrogel derived LLTO framework evidences enhancement of the conductivity. This enhancement is attributed to the decreased nanoparticle agglomeration, and high interphase volume creates the continuous conducting paths connected in 3D structure [126].

The ion transport in the SP-based polymer electrolytes is altered by the salt concentration and the temperature of evaporation (protein–ion complex formation temperature). Figure 36ii shows the modification observed in the protein–ion complex by controlling the proteins/ions ratio and complex formation temperature. The controlled process results in favorable chain reorganization that contributes to the enhancement of the conductivity. A decoupled ion transport mechanism was developed by Fu et al. [117] in protein ion conductors (PIC). This mechanism was based on the experimental and theoretical results. Figure 36ii shows the locking of the anion (ClO_4^-) with the positive groups of protein and cation migrates via the hopping process. The presence of oxygen in the protein backbone provides coordinating sites to the cation. Here, hopping of the cation is also attributed to the anions connecting coordinating sites and this evidences the decoupled ion transport from protein chain motion. So, in PIC three important benefits are: (1) achieving single-ion conductor due to locked anion or immobilized state with specific functional group of protein and (2) anion clustering lowers the activation energy. Table 7 shows the comparisons of electrical, transport, thermal and electrochemical properties of various solid polymer electrolytes (Fig. 37).

Summary and future prospects

In conclusion, we reviewed the topical evolvement of the solid polymer electrolytes (SPEs) for high-energy all-solid-state Li-ion batteries (ASSLIBs). First of all, the advantages of ASSBs were discussed in detail over the existing battery followed by brief about solid polymer electrolytes. Then solid polymer electrolytes were divided into ceramic, garnet, block, star, cross-linked, polycarbonate and soy protein-polymer electrolytes depending on their morphology, and architecture. Two important sections highlight the thermal runway issue and dendrite growth prevention strategies. We discussed the preparation method, and crucial characterizations need to be done for evaluating the characteristic properties. After that, we discussed in detail the electrochemical performance

Table 7 Different solid polymer electrolytes and their electrical, transport, thermal and electrochemical properties

Materials used	Electrical conductivity (S cm^{-1})	Transference number (t^+; cation)	Electrochemical stability Window(V)	Thermal Stability (°C)	Cell configuration*	Capacity (mAh g^{-1})	Coulombic Efficiency (%)	Capacity retention (%)	Year	References
Ceramic										
PVDF/LLTO-PEO/PVDF	~ 3.01×10^{-3}	0.67/0.70	5	343	LCO/SWEs-III/Li	144 (1 C)	–	91.8 (after 100th Cy.)	2018	[124]
Oxalate-chelated borate-grafted PVFM	~ 10^{-5}	–	5	106	Li/LFP cell	139	82.7 (after 1st 99.7 (after 20th)	–	2014	[125]
PVA/LLTO	8.8×10^{-5} (25 °C) 1.5×10^{-4} (30 °C)	–	4.5	400	–	–	–	–	2018	[126]
β-type PS_4/Li_3PS_4	8.01×10^{-4} (in situ) 6.98×10^{-4} (mechanical-mixing [60 °C]	0.33 (in situ) 0.28 (mechanical-mixing	5.1 (in situ) 4.9 (mechanical-mixing	–	LFP/PEO-2% vol Li_3PS_4 (in situ)/Li	153 (0.1 C)	–	86.1 (after 100th Cy.) 85.9 (after 325th Cy.)	2011	[129]
PEO/LLZTO	1.17×10^{-4} (@ 30 °C) 1.58×10^{-3} (@ 80 °C)	–	5	–	LFP|PEO-LLZTO-PEG-60 wt % LiTFSI|Li	149.1 (0.1 C), 139.1 (0.1 C; after 100th Cy.)	100 (after 50th Cy.)	–	2018	[130]
PEO/LATP	$1.15 \times 10^{-5\ 1}$ (30 °C) 7.03×10^{-4} (80 °C).	–	–	–	LFP/L@P01/Li	118.3 (RT), 151.6 (60 °C),	84.2 (after 20th Cy.)	–	2019	[133]
PEO^B2K-POSS	0.16×10^{-3} (30 °C), and 0.7×10^{-3} (60 °C)	–	4.3	–	Li/$PEOB_{12}$KPOSS/Li	146.5, 144.5 (after 100th Cy.) [0.2 C]	99, 99.7 (after 100th Cy.)	–	2018	[113]
PEO/LiTFSI/LLZO	5.5×10^{-4} (30 °C)	0.207 (60 °C)	5.7	–	Li° |CPE| LFP	150.1 (after 3 cycles); 149.5 (after 50 cycles), 121 (after 100 cycles)	98.9	93.2 (after 1st), 89 (after 100th Cy.)	2017	[170]
PVA/LiTFSI/LLZO	8.5×10^{-5} (25 °C) 10^{-3} (60 °C)	–	5	350	–	–	–	–	2018	[171]
(PVDF)–$LiClO_4$/LLZO	2.6×10^{-4} (25 °C)	0.682	–	300	–	–	–	–	2019	[172]
PEO-PPC-LiTFSI-LLTO	5.66×10^{-5} (25 °C), 5.7×10^{-4} (80 °C)	0.227	5.1	–	LFP/SPE/Li	135 (0.5 C), 130 (after 100th Cy.)	100	96	2019	[173]
PEO-LiTFSI/g-C_3N_4	1.7×10^{-5} (30 °C)	0.56	4.7	–	Li | SPE | LFP	161.3, 155 (after 150th Cy.)	99.5	–	2019	[174]
Block copolymer electrolyte										
Jeffamine®)/(LiFSI)	5.6×10^{-4} (70 °C), 2×10^{-4} (40 °C)	0.16 (70 & 40 °C)	4	200	Li° |BCP| LFP	160 (C/20)	–	–	2018	[134]
BCP with PS and Jeffamine	5.6×10^{-4} (70 °C), 7.9×10^{-5} (40 °C)	0.08 (70 °C)	5.8	346	Li° |BCP| LFP	140 (after 1st)	100 (after 30th)	–	2018	[135]
PEGDE-PEGDA-1000 [DN-SPE]	5.3×10^{-5} (30 °C)	0.44	4.7	–	LFP/DN-SPE/Li	162 (0.2 C) [55 °C], 125 (after 150th Cy.)	99.5	–	2018	[136]
Multi-block copolymer (SI)	3.2×10^{-4}	1	4.8/4.9	–	Li/SI/NCM	150 (C/20)	86, 99.5 (after 230 Cy.; C/5)	–	2018	[137]
BPSO/LiTFSI/PVDF	4×10^{-4} (25 °C)	0.52 (25 °C)	4.7	–	–	–	–	–	2018	[175]

Table 7 continued

Materials used	Electrical conductivity (S cm^{-1})	Transference number (t^{+}; cation)	Electrochemical stability Window(V)	Thermal Stability (°C)	Cell configuration*	Capacity (mAh g^{-1})	Coulombic Efficiency (%)	Capacity retention (%)	Year	References
Polycarbon@-based electrolyte										
PCPU/PCDL/HDI/DEG/LiTFSI	2.2 × 10^{-6} (25 °C), 1.58 × 10^{-5} (60 °C) 1.12 × 10^{-4} (80 °C)	0.45 (80 °C)	4.5 (80 °C),	300	LFP/PCPU10-20% Li/Li	128 (0.2 C 127 (after 100th Cy.)	100	99 (after 100th Cy.) 91 (after 600th Cy.)	2018	[141]
WPU/PEG/HDI	7.3 × 10^{-4} (60 °C) 2.2 × 10^{-3} (80 °C)	–	4.8 V (60 °C)	∼ 200	LFP/SPE/Li	151 (0.1 C),	–	97 (after 50th Cy.)	2018	[144]
Poly(ε-caprolactone) (PCL)	4.1 × 10^{-5} (25 °C)	0.66 (60 °C), 0.62 (40 °C)	–	–	Li/SPE/LFP	150 (C/50),	100	–	2015	[176]
PTMC/LiTFSI	10^{-7} (60 °C)		5	190	LFP/PTMC-LiTFSI/Li	153	–	–	2014	[177]
PTMC/LiTFSI/LiBF$_4$	3 × 10^{-6} (for LiTFSI) 2 × 10^{-6} (LiBF$_4$) (60 °C).	–	–	–	LFP/PC/Li	–	100 (after 140th Cy.)	–	2015	[178]
PAEC/LiTFSI	2 × 10^{-7} (25 °C)	–	–	–	V$_2$O$_5$/PCE/Li	11 µAh/cm^2 (areal capacity)	–	–		[179]
PEC/LiFSI	2.5 × 10^{-5} (30 °C)	0.5	5	–	Li|PEC-LiFSI|LFP	120-130 (C/10)	–	–	2016	[180]
Star polymer electrolyte										
OV-POSS/PEGMEM	1.13 × 10^{-4} (SCP5.1) 5.63 × 10^{-5}(LCP5.1) (25 °C).	0.35 (SCP5.1) 0.19 (LSP5.1)	5.31 (SCP5.1) 5.04 (LSP5.1)	–	Li/SCP5.1/LFP	163.8, 147.8 (after 100 th)	100	90.2	2016	[92]
PEGDMA$_{550}$ (Li-SPE550-Li)	2.82 × 10^{-5} (20 °C)	0.3	5.4	–	Li|K-SPE750-Li|LFP	137.7, 130.5 (after 150th Cy.)	97 (after 1st Cy.), 98 (after 150th Cy.)	95	2019	[119]
PMMA-b-PPEGMA/LITFSI	8.3 × 10^{-5} (30 °C), 2.0 × 10^{-4} (80 °C)	0.31 (@ 60 °C)	4.7	372	–	–	–	–	2016	[181]
(HBPS-(PTFEMA-b-PPEGMA)$_{27}$)/LiTFSI	2.36 × 10^{-5} (25 °C), 4.1 × 10^{-4} (80 °C)	0.26	4.9	374.7	Li/SPE/Li	139, 147 (after 5th Cy.) [0.1 C, 60 °C)]	100 (after 100th Cy.)	–	2018	[93]
PEGMA/DLC-((PS)$_{23}$)$_6$/LiTFSI	1.94 × 10^{-4} (30 °C),	0.37	5.1 (30 °C)	350	Li/SPE/Li	139 (0.1 C), 130 (after 50th Cy.) [60 °C] 162 (0.1 C), 130 (after 50th Cy.) [60 °C]	96, 100 (after 50th Cy.) [60 °C], 97 (80 °C)	–	2018	[182]
The fibrous membrane as the electrolyte										
PVDF–PAN–ESFMs	7.8 × 10^{-3} (25 °C)	–	5.1	–	LCO/PVdF–PAN–ESFM/Li	120.4 (0.1 C	–	93 (after 150th Cy.)	2018	[147]
PVDF-co-HFP/oligomeric ionic liquids	0.12 × 10^{-3}, (RT)	–	4.5	–	Li/PVdF-HFP/70% OIL/LFP	152 (@ 0.1 C)	99 (after 100th Cy.)		2016	[152]
PSF–PEO/LiTFSI/SN	1.6 × 10^{-4} (RT) 1.14 × 10^{-3} (80 °C)	–	4.2	–	Li/PSF–PEO$_{35}$ + LiTFSI + SN/LFP	152 (C/3), ∼ 125 (after 30th Cy.)	–	–	2013	[153]
P(VDF-HFP)-(PE-PM-PVH)	0.81 × 10^{-3}	0.72	∼ 5	200	–	152.7, 149.6 (after 100th Cy.)	99	98	2018	[154]

Table 7 continued

Materials used	Electrical conductivity (S cm^{-1})	Transference number (t^+; cation)	Electrochemical stability Window(V)	Thermal Stability (°C)	Cell configuration*	Capacity (mAh g^{-1})	Coulombic Efficiency (%)	Capacity retention (%)	Year	References
TEOS: PSZ	$1.04 \pm 0.05 \times 10^{-3}$	–	–	–	LCO/PSZ-TEOS/graphite	134	–	93 (after 100th Cy.)	2017	[155]
PAN/PEO/PDMA	0.67×10^{-3} (30 °C)	0.58	4.5		Li/PE/LFP	154 (0.1 C)	–	–	2015	[156]
PEO-LiTFSI/ LLTO nanofiber	1.8×10^{-4} (RT)	0.33	4.5	~ 350	Li|3D-CPE|Li	80 (0.3 C), 25 °C	90-100	–	2018	[157]
Polyphosphazene/ PVDF-HFP/ LiBOB/LATP	–	–	4.7	–	Li|LHSE|$Li_3V_2(PO_4)_3$/CN	130.5, 107.6 (after 500th Cy.)	–	88.2	2019	[160]
PVDF-HFP/ LiTFSI/LLZO nanofiber	9.5×10^{-4} (20 °C)	–	5.2	350	Li/PVDF-HFP/LiTFSI/ LLZO CPE/LFP	140 (0.2 C)	99.9	93 (after 150th cycle 0.5 C)	2019	[94]
PEO/LiTFSI/ LLTO nanofiber	2.4×10^{-4}	–	5	–	–	–	–	–	2018	[97]
Cross-linked solid polymer electrolyte										
PEOEC/LiClO4/ OA-POSS	3.74×10^{-5} (30 °C), 3.26×10^{-4} (60 °C)	–	5.0	175	Li/L-HIPE10 (with $LiSO_3CF_3$)/V_2O_5	280	–	~ 100 (after 30 cy.)	2014	[161]
PAN/SiO_2 (MA-SiO_2)/TEGDA	1.1×10^{-3} (non-porous),1.8×10^{-3} (mesoporous)	–	–	–	NCM/composite electrolyte/graphite	179.5, 157.9 (after 300 Cy.)	–	88.0 (mesoporous)	2016	[162]
PEGDA/DVB	1.4×10^{-4}	0.23	5	–	LFP/SPE with 10% DVB/ Li metal	123, 138 (after 20 Cy.)	–	–	2016,	[114]
POSS	3.94×10^{-5} (25 °C), 1.39×10^{-3} (80 °C)	–	–	–	LFP/HPE + 5 wt% POSS/Li	154, 152.1 (after 150th Cy.)	99	88	2018	[163]
PEG/LiTFSI/ RTIL	4×10^{-4} (25 °C), 1.45×10^{-3} (65 °C).	–	4.8	–	NMC/PE/Li	118 (C/10)	99	–	2016	[183]
PEO-TEGDMA-TEGDME	2.7×10^{-4} (24 °C)	0.56	5.38	120	Li/PTT-SPE/Li	160 (0.05 C)	–	98.8 (after 100 Cy. (0.1 C)	2019	[164]
PEO/Acryl-HBP/ PEGDME	1.24×10^{-4} (20 °C), 1.97×10^{-3} (80 °C) for benzoyl peroxide radical initiator	0.33 (30 °C)	4.5 (30 °C)	–	$Li_4Ti_5O_{12}$/CLPE/LFP–C cell	140 (C/10)	96	–	2018	[184]
	2.44×10^{-4} (25 °C), 3.22×10^{-3} (80 °C). For EB radiation	–	–	–	Cu/LTO/CLPE/LFP-C/Al [Full cell]	42 mAh (C/10)	–	80 (after 340th Cy.) 9. (after 8 month storage)		
Soy protein-based solid polymer electrolyte										
SP + $LiClO_4$	10^{-5} S	0.94	–	–	–	–	–	–	2016	[117]
PEO–$LiClO_4$/ TiO_2-SP-close	10 − 5–10 − 4 (20-90 °C)	–	5.2	–	–	–	–	–	2018	[166]
PEO–$LiClO_4$/ TiO_2-SP-Open	6×10^{-5}, 7×10^{-4} (90 °C)	–	5.4	–	LCO/CPE–TiO_2/(SP-open)-hybrid/Li (65 °C)	135–128 (after 24 Cy.)	95	–		
PEO; UHMWPEO-$LiClO_4$/core–shell protein@TiO_2 NW	1.1×10^{-4}, 2×10^{-3} (80 °C).	0.62 & 0.41 (PEO only)	5.4	–	LCO/CPE/Li (65 °C)	135 (0.2 C)	98.6	94.7 (after 70 Cy.)	2018	[167]

Table 7 continued

Materials used	Electrical conductivity (S cm^{-1})	Transference number (t^{+}; cation)	Electrochemical stability Window(V)	Thermal Stability (°C)	Cell configuration*	Capacity (mAh g^{-1})	Coulombic Efficiency (%)	Capacity retention (%)	Year	References
2D MXene/ore/other containing polymer electrolytes										
PEO-LiTFSI/ MXene ($Ti_3C_2T_x$)	2.2×10^{-5} (28 °C), 0.69×10^{-3} (60 °C)	0.18	5.2	–	LFP|PEO_{20}-LiTFSI-MXene0.02|Li (60 °C)	150 (C/10)	> 97 (after 100th)	91.4 (after 100th Cy.)	2019	[185]
PEO-$LiClO_4$-lepidolite	1.39×10^{-6} (RT), 1.23×10^{-4} (60 °C)	0.72	6	–	LFP|CPE|Li	120 (0.15 C)	100	–	2019	[186]
PEO-LiTFSI/ Vermiculite clay sheets (VS)	2.9×10^{-5} (25 °C), 1.2×10^{-3} (60 °C) 3.1×10^{-3} (100 °C)	0.246 (25 °C), 0.497 (90 °C)	5.35 (25 °C), 5.0 (100 °C)		Li/PEO-LiTFSI + 10% VS/Li	159.9 (0.1 C)	–	–	2018	[187]
PEO-LiTFSI/ Vertically aligned vermiculite sheets (VAVS	1.89×10^{-4} (25 °C),	0.47 (RT)	–	–	Li|VS–CSPE|LFP	167 (0.1 C)	–	82 (after 200th Cy.)	2019	[188]
PEO-LiTFSI-PAGP	1.6×10^{-5}	–	5.0	–	LFP/(HSPE or SPE)/Li	100 (0.1 C)	>99.5	–	2019	[189]
POSS-ILs	8.0×10^{-4} (22 °C) 2.0×10^{-3} (62 °C)	–	5.0	–	Li/POSS-PrMIM-SPE/ LiFePO4	136.3	–	–	2018	[190]
(P(MMA-co-AMPSLi))	4.12×10^{-3}	–	5.0	–	–	–	–	–	2019	[191]
PEO–LiX-LAO	1.36×10^{-5} (30 °C)	–	5.2		Li/PEOL-SPE/LiFePO4	153.1	97	–	2019	[192]
PEO/LiBOB/ LLZTO		0.57	~ 5.0	–	Li/PEO/LiBOB/LLZTO/ LiFePO4	165.9	84.9 (100th Cy.)	–	2019	[193]

*LCO: $LiCoO_2$, LFP: $LiFePO_4$, NCM: $LiNiMnCoO_2$

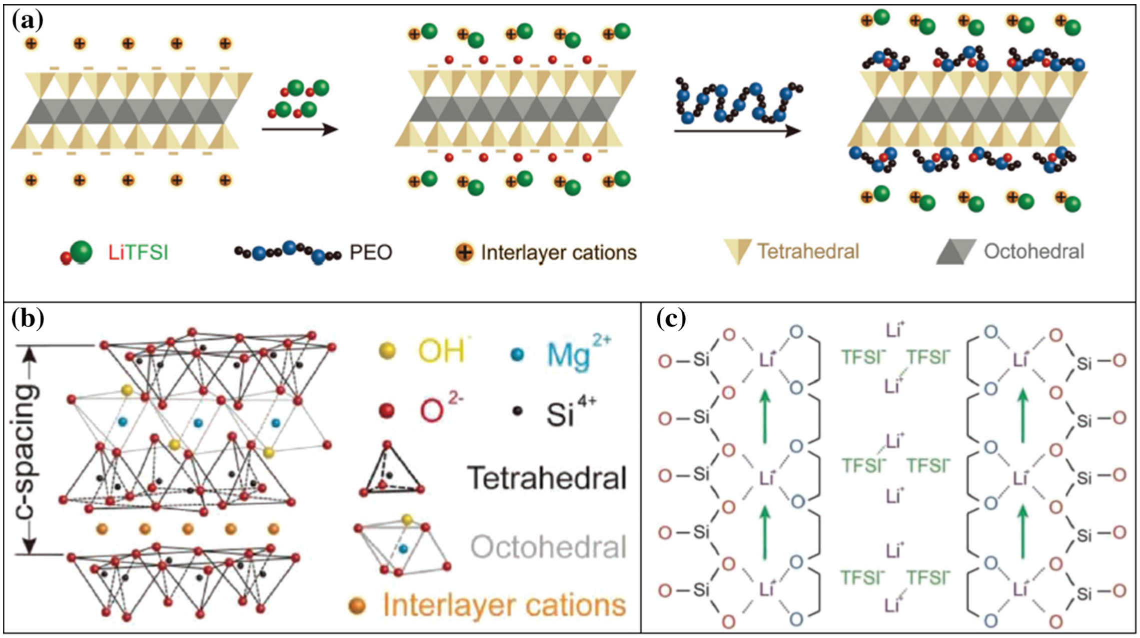

Figure 37 **a** Schematic showing the mechanism for VS enhanced ionic conductivity in SPE (Reproduced with permission from Ref. [187] © John Wiley and Sons 2018), **b** structure model of vermiculite sheet, and **c** schematic of Li^+ transport in VAVS–CSPE (Reproduced with permission from Ref. [188] © John Wiley and Sons 2019).

of various types of solid polymer electrolyte in the ASSLIBs. Finally, we discussed the ion transport mechanism in various types of solid polymer electrolytes.

ASSLIBs have gained attention due to the increasing demand for energy and are discussed in detail in this review. The key advantages of the SSBs are safety, small in size and better fabrication. The important parameters that need to be addressed are ionic conductivity, cation transport number, voltage stability window, good interfacial contact, and thermal stability. Along with this, there is a need for an increase in energy density, Coulombic efficiency, capacity retention, and cyclic stability.

In future scope, there is a need to develop a new method of creating good interfacial contact and development of new material architecture. New materials that have the potential to enhance the electrochemical properties of ASSBs are MXenes (2D) materials owing to their unique features such as higher surface area than 0D and 1D. MXenes is a new family of transition metal carbides and/or nitrides. Along with these advanced SPE, there is significant investigation required to search the novel electrodes (cathode/anode) for optimum performance of the overall battery. In brief, we sincerely hope that this review provides a competent way to project vital breakthroughs in the progress of newly solid polymer electrolytes for ASSLIBs, and also opens doors for novel approaches.

Compliance with ethical standards

Conflict of interest The authors declare that they have no conflict of interest.

References

[1] Arya A, Sharma AL (2017) Insights into the use of polyethylene oxide in energy storage/conversion devices: a critical review. J Phys D Appl Phys 50(44):443002

[2] Croce F, Appetecchi GB, Persi L, Scrosati B (1998) Nanocomposite polymer electrolytes for lithium batteries. Nature 394(6692):456–458

[3] Agrawal RC, Pandey GP (2008) Solid polymer electrolytes: materials designing and all-solid-state battery applications: an overview. J Phys D Appl Phys 41(22):223001

[4] Armand M, Tarascon JM (2008) Building better batteries. Nature 451(7179):652–657

[5] Tarascon JM, Armand M (2011) Issues and challenges facing rechargeable lithium batteries. In: Materials for sustainable energy: a collection of peer-reviewed research and review articles from Nature Publishing Group, pp 171–179

[6] Whittingham MS (2004) Lithium batteries and cathode materials. Chem Rev 104(10):4271–4302

[7] Scrosati B, Garche J (2010) Lithium batteries: status, prospects and future. J Power Sources 195(9):2419–2430

[8] Gulzar U, Goriparti S, Miele E, Li T, Maidecchi G, Toma A, De Angelis F, Capiglia C, Zaccaria RP (2016) Next-generation textiles: from embedded supercapacitors to lithium ion batteries. J Mater Chem A 4(43):16771–16800

[9] Goodenough JB, Kim Y (2011) Challenges for rechargeable batteries. J Power Sources 22(3):587–603

[10] Marom R, Amalraj SF, Leifer N, Jacob D, Aurbach D (2011) A review of advanced and practical lithium battery materials. J Mater Chem 21(27):9938–9954

[11] Wu F, Yushin G (2017) Conversion cathodes for rechargeable lithium and lithium-ion batteries. Energy Environ Sci 10(2):435–459

[12] Croy JR, Abouimrane A, Zhang Z (2014) Next-generation lithium-ion batteries: the promise of near-term advancements, MRS Bulletin. MRS Bull 39(5):407–415

[13] Thackeray MM, Wolverton C, Isaacs ED (2012) Electrical energy storage for transportation—approaching the limits of, and going beyond, lithium-ion batteries. Energy Environ Sci 5(7):7854–7863

[14] Meyers RA (ed) (2012) Encyclopedia of sustainability science and technology, Chap. 2. Springer, New York

[15] Jossen A (2006) Fundamentals of battery dynamics. J Power Sources 154(2):530–538

[16] Pritam, Arya A, Sharma AL (2019) Dielectric relaxations and transport properties parameter analysis of novel blended solid polymer electrolyte for sodium-ion rechargeable batteries. J Mater Sci 54(9):7131–7155. https://doi.org/10.1007/s10853-019-03381-3

[17] Pritam, Arya A, Sharma AL (2019) Selection of best composition of Na^+ ion conducting PEO-PEI blend solid polymer electrolyte based on structural, electrical, and dielectric spectroscopic analysis. Ionics 26:745–766

[18] Goodenough JB, Singh P (2015) Solid electrolytes in rechargeable electrochemical cells. J Electrochem Soc 162(14):A2387–A2392

[19] Wu B, Wang S, Evans WJ, Deng DZ, Yang J, Xiao J (2016) Interfacial behaviours between lithium ion conductors and electrode materials in various battery systems. J Mater Chem A 4(40):15266–15280

[20] Bhattacharya M (2016) Polymer nanocomposites—a comparison between carbon nanotubes, graphene, and clay as nanofillers. Materials 9(4):262

[21] Xue Z, He D, Xie X (2015) Poly (ethylene oxide)-based electrolytes for lithium-ion batteries. J Mater Chem A 3(38):19218–19253

[22] Jiang Y, Yan X, Ma Z, Mei P, Xiao W, You Q, Zhang Y (2018) Development of the PEO based solid polymer electrolytes for all-solid state lithium ion batteries. Polymers 10(11):1237

[23] Saito Y, Morimura W, Kuse S, Kuratani R, Nishikawa S (2017) Influence of the morphological characteristics of separator membranes on ionic mobility in lithium secondary batteries. J Phys Chem C 121(5):2512–2520

[24] Xia L, Yu L, Hu D, Chen GZ (2017) Electrolytes for electrochemical energy storage. Mater Chem Front 1(4):584–618

[25] Cheng XB, Zhao CZ, Yao YX, Liu H, Zhang Q (2019) Recent advances in energy chemistry between solid-state electrolyte and safe lithium-metal anodes. Chem 5:74–96

[26] Yue J, Ma J, Zhang J, Zhao J, Dong S, Liu Z, Cui G, Chen L (2016) All solid-state polymer electrolytes for high-performance lithium ion batteries. Energy Storage Mater 5:139–164

[27] Dirican M, Yan C, Zhu P, Zhang X (2019) Composite solid electrolytes for all-solid-state lithium batteries. Mater Sci Eng R 136:27–46

[28] Meesala Y, Jena A, Chang H, Liu RS (2017) Recent advancements in Li-ion conductors for all-solid-state Li ion batteries. ACS Energy Lett 2:2734–2751

[29] Schnell J, Günther T, Knoche T, Vieider C, Köhler L, Just A, Reinhart G (2018) All-solid-state lithium-ion and lithium metal batteries–paving the way to large-scale production. J Power Sources 382:160–175

[30] Tong B, Wang J, Liu Z, Ma L, Zhou Z, Peng Z (2018) Identifying compatibility of lithium salts with LiFePO4 cathode using a symmetric cell. J Power Sources 384:80–85

[31] Famprikis T, Canepa P, Dawson JA, Islam MS, Masquelier C (2019) Fundamentals of inorganic solid-state electrolytes for batteries. Nat Mater 18:1278–1291

[32] Xia S, Wu X, Zhang Z, Cui Y, Liu W (2019) Practical challenges and future perspectives of all-solid-state lithium-metal batteries. Chem 5(4):753–785

[33] Kerman K, Luntz A, Viswanathan V, Chiang YM, Chen Z (2017) Review—Practical challenges hindering the development of solid state Li ion batteries. J Electrochem Soc 164(7):A1731–A1744

[34] Arya A, Sharma AL (2017) Polymer electrolytes for lithium ion batteries: a critical study. Ionics 23(3):497–540

[35] Arya A, Sharma AL (2019) Electrolyte for energy storage/conversion (Li^+, Na^+, Mg^{2+}) devices based on PVC and their associated polymer: a comprehensive review. J Solid State Electrochem 23(4):997–1059

[36] Arya A, Sharma AL (2020) Polymer Nanocomposites: synthesis and characterization. In: Wiesner M, Bottero JY

(eds) Environmental nanotechnology, vol 4. Springer, Cham, pp 265–315

[37] Xu K, Wang C (2016) Batteries: widening voltage windows. Nat Energy 1(10):16161

[38] Kong L, Li C, Jiang J, Pecht MG (2018) Li-ion battery fire hazards and safety strategies. Energies 11(9):2191

[39] Liu K, Liu Y, Lin D, Pei A, Cui Y (2018) Materials for lithium-ion battery safety. Sci Adv 4(6):eaas9820

[40] Wang Q, Ping P, Zhao X, Chu G, Sun J, Chen C (2012) Thermal runaway caused fire and explosion of lithium ion battery. J Power Sources 208:210–224

[41] Arya A, Sharma AL (2018) Structural, microstructural and electrochemical properties of dispersed-type polymer nanocomposite films. J Phys D Appl Phys 51(4):045504

[42] Arya A, Sharma AL (2018) Structural, electrical properties and dielectric relaxations in Na^+-ion-conducting solid polymer electrolyte. J Phys Condens Matter 30(16):165402

[43] Petronico A, Moneypenny TP, Nicolau BG, Moore JS, Nuzzo RG, Gewirth AA (2018) Solid-liquid lithium electrolyte nanocomposites derived from porous molecular cages. J Am Chem Soc 24:7504–7509

[44] Rosso M, Brissot C, Teyssot A, Dollé M, Sannier L, Tarascon JM, Bouchet R, Lascaud S (2006) Dendrite short-circuit and fuse effect on Li/polymer/Li cells. Electrochim Acta 51(25):5334–5340

[45] Wu B, Liu Q, Mu D, Xu H, Wang L, Shi L, Gai L, Wu F (2016) Suppression of lithium dendrite growth by introducing a low reduction potential complex cation in the electrolyte. RSC Adv 6(57):51738–51746

[46] Bai P, Li J, Brushett FR, Bazant MZ (2016) Transition of lithium growth mechanisms in liquid electrolytes. Energy Environ Sci 9(10):3221–3229

[47] Ilott AJ, Mohammadi M, Chang HJ, Grey CP, Jerschow A (2016) Real-time 3D imaging of microstructure growth in battery cells using indirect MRI. Proc Natl Acad Sci USA 113(39):10779–10784

[48] Mehdi BL, Stevens A, Qian J, Park C, Xu W, Henderson WA, Zhang JG, Mueller KT, Browning ND (2016) The impact of Li grain size on coulombic efficiency in Li batteries. Sci Rep 6:34267

[49] Ma J, Chen B, Wang L, Cui G (2018) Progress and prospect on failure mechanisms of solid-state lithium batteries. J Power Sources 392:94–115

[50] Brissot C, Rosso M, Chazalviel JN, Baudry P, Lascaud S (1998) In situ study of dendritic growth in lithium/PEO-salt/lithium cells. Electrochim Acta 43:1569–1574

[51] Brissot C, Rosso M, Chazalviel JN (1999) Dendritic growth mechanisms in lithium/polymer cells. J Power Sources 81:925–929

[52] Dollé M, Sannier L, Beaudoin B (2002) Live scanning electron microscope observations of dendritic growth in lithium/polymer cells. Electrochem Solid-state Lett 5:A286–A289

[53] Rosso M, Brissot C, Teyssot A, Dollé M, Sannier L, Tarascon JM, Bouchet R, Lascaud S (2006) Dendrite short-circuit and fuse effect on Li/polymer/Li cells. Electrochim Acta 51:5334–5340

[54] Harry KJ, Hallinan DT, Parkinson DY, MacDowell AA, Balsara NP (2014) Detection of subsurface structures underneath dendrites formed on cycled lithium metal electrodes. Nat Mater 13:69–73

[55] Yang L, Wang Z, Feng Y, Tan R, Zuo Y, Gao R, Zhao Y, Han L, Wang Z, Pan F (2017) Flexible composite solid electrolyte facilitating highly stable "soft contacting" Li–electrolyte interface for solid state lithium-ion batteries. Adv Energy Mater 7:1701437

[56] Wang C, Yang Y, Liu X, Zhong H, Xu H, Xu Z, Shao H, Ding F (2017) Suppression of lithium dendrite formation by using LAGP-PEO (LiTFSI) composite solid electrolyte and lithium metal anode modified by PEO (LiTFSI) in all-solid-state lithium batteries. ACS Appl Mater Interfaces 9:13694–13702

[57] Wu H, Zhuo D, Kong D, Cui Y (2014) Improving battery safety by early detection of internal shorting with a bifunctional separator. Nat Commun 5:5193

[58] Li W, Yao H, Yan K, Zheng G, Liang Z, Chiang YM, Cui Y (2015) The synergetic effect of lithium polysulfide and lithium nitrate to prevent lithium dendrite growth. Nat Commun 6:7436

[59] Zhao CZ, Zhang XQ, Cheng XB, Zhang R, Xu R, Chen PY, Peng HJ, Huang JQ, Zhang Q (2017) An anion-immobilized composite electrolyte for dendrite-free lithium metal anodes. Proc Natl Acad Sci USA 114(42):11069–11074

[60] Kim SH, Choi KH, Cho SJ, Kil EH, Lee SY (2013) Mechanically compliant and lithium dendrite growth-suppressing composite polymer electrolytes for flexible lithium-ion batteries. J Mater Chem A 1(16):4949–4955

[61] Luo W, Zhou L, Fu K, Yang Z, Wan J, Manno M, Yao Y, Zhu H, Yang B, Hu L (2015) A thermally conductive separator for stable Li metal anodes. Nano Lett 15(9):6149–6154

[62] Wu JY, Ling SG, Yang Q, Li H, Xu XX, Chen LQ (2016) Forming solid electrolyte interphase in situ in an ionic conducting $Li_{1.5}Al_{0.5}Ge_{1.5}(PO_4)$ 3-polypropylene (PP) based separator for Li-ion batteries. Chin Phys B 25:78204

[63] Zhao CZ, Chen PY, Zhang R, Chen X, Li BQ, Zhang XQ, Cheng XB, Zhang Q (2018) An ion redistributor for dendrite-free lithium metal anodes. Sci Adv 4(11):eaat3446

[64] Hendricks C, Williard N, Mathew S, Pecht M (2015) A failure modes, mechanisms, and effects analysis (FMMEA) of lithium-ion batteries. J Power Sources 297:113–120

[65] Niitani T, Shimada M, Kawamura K, Kanamura K (2005) Characteristics of new-type solid polymer electrolyte controlling nano-structure. J Power Sources 146(1–2):386–390

[66] Khan IM, Fish D, Delaviz Y, Smid J (1989) ABA triblock comb copolymers with oligo (oxyethylene) side chains as matrix for ion transport. Macromol Chem Phys 190(5):1069–1078

[67] Kamigaito M, Ando T, Sawamoto M (2001) Metal-catalyzed living radical polymerization. Chem Rev 101(12):3689–3746

[68] Holmberg S, Holmlund P, Wilén CE, Kallio T, Sundholm G, Sundholm F (2002) Synthesis of proton-conducting membranes by the utilization of preirradiation grafting and atom transfer radical polymerization techniques. J Polym Sci Part A Polym Chem 40(4):591–600

[69] Grewal MS, Tanaka M, Kawakami H (2019) Bifunctional poly (ethylene glycol) based crosslinked network polymers as electrolytes for all-solid-state lithium ion batteries. Polym Int 68(4):684–693

[70] Porcarelli L, Gerbaldi C, Bella F, Nair JR (2016) Super soft all-ethylene oxide polymer electrolyte for safe all-solid lithium batteries. Sci Rep 6:19892

[71] Cui Y, Liang X, Chai J, Cui Z, Wang Q, He W, Feng J (2017) High performance solid polymer electrolytes for rechargeable batteries: a self-catalyzed strategy toward facile synthesis. Adv Sci 4(11):1700174

[72] Huang S, Cui Z, Qiao L, Xu G, Zhang J, Tang K, Cui G (2019) An in situ polymerized solid polymer electrolyte enables excellent interfacial compatibility in lithium batteries. Electrochim Acta 299:820–827

[73] Nair JR, Colò F, Kazzazi A, Moreno M, Bresser D, Lin R, Appetecchi GB (2019) Room temperature ionic liquid (RTIL)-based electrolyte cocktails for safe, high working potential Li-based polymer batteries. J Power Sources 412:398–407

[74] Nair JR, Destro M, Bella F, Appetecchi GB, Gerbaldi C (2016) Thermally cured semi-interpenetrating electrolyte networks (s-IPN) for safe and aging-resistant secondary lithium polymer batteries. J Power Sources 306:258–267

[75] Nair JR, Porcarelli L, Bella F, Gerbaldi C (2015) Newly elaborated multipurpose polymer electrolyte encompassing RTILs for smart energy-efficient devices. ACS Appl Mater Interfaces 7:12961–12971

[76] Falco M, Simari C, Ferrara C, Nair JR, Meligrana G, Bella F, Gerbaldi C (2019) Understanding the effect of UV-induced crosslinking on the physico-chemical properties of highly performing PEO/LiTFSI-based polymer electrolytes. Langmuir 35:8210–8219

[77] Nair JR, Shaji I, Ehteshami N, Thum A, Diddens D, Heuer A, Winter M (2019) Solid polymer electrolytes for lithium metal battery via thermally induced cationic ring-opening polymerization (CROP) with an insight into the reaction mechanism. Chem Mater 31(9):3118–3133

[78] Nuyken O, Pask S (2013) Ring-opening polymerization—an introductory review. Polymers 5(2):361–403

[79] Ehteshami N, Eguia-Barrio A, de Meatza I, Porcher W, Paillard E (2018) Adiponitrile-based electrolytes for high voltage, graphite-based Li-ion battery. J Power Sources 397:52–58

[80] Zaheer M, Xu H, Wang B, Li L, Deng Y (2020) An in situ polymerized comb-like PLA/PEG-based solid polymer electrolyte for lithium metal batteries. J Electrochem Soc 167(7):070504

[81] Arya A, Sharma AL (2018) Effect of salt concentration on dielectric properties of Li-ion conducting blend polymer electrolytes. J Mater Sci Mater Electron 29(20):17903–17920

[82] Arya A, Saykar Nilesh G, Sharma AL (2019) Impact of shape (nanofiller vs. nanorod) of TiO_2 nanoparticle on free-standing solid polymeric separator for energy storage/conversion devices. J Appl Polym Sci 136(16):47361

[83] Zhang X, Xie J, Shi F, Lin D, Liu Y, Liu W, Pei A, Gong Y, Wang H, Liu K, Xiang Y, Cui Y (2018) Vertically aligned and continuous nanoscale ceramic-polymer interfaces in composite solid polymer electrolytes for enhanced ionic conductivity. Nano Lett 18(6):3829–3838

[84] Liang X, Han D, Wang Y, Lan L, Mao J (2018) Preparation and performance study of a PVDF-LATP ceramic composite polymer electrolyte membrane for solid-state batteries. RSC Adv 8(71):40498–40504

[85] Young WS, Kuan WF, Epps TH (2014) Block copolymer electrolytes for rechargeable lithium batteries. J Polym Sci Part B Polym Phys 52(1):1–16

[86] Giacomelli C, Schmidt V, Aissou K, Borsali R (2010) Block copolymer systems: from single chain to self-assembled nanostructures. Langmuir 26(20):15734–15744

[87] Young WS, Epps TH (2012) Ionic conductivities of block copolymer electrolytes with various conducting pathways: Sample preparation and processing considerations. Macromolecules 45(11):4689–4697

[88] Cho BK, Jain A, Gruner SM, Wiesner U (2004) Mesophase structure-mechanical and ionic transport correlations in extended amphiphilic dendrons. Science 305(5690):1598–1601

[89] Mindemark J, Lacey MJ, Bowden T, Brandell D (2018) Beyond PEO—alternative host materials for Li + -

conducting solid polymer electrolytes. Prog Polym Sci 81:114–143

[90] Zhang J, Yang J, Dong T, Zhang M, Chai J, Dong S, Cui G (2018) Aliphatic polycarbonate-based solid-state polymer electrolytes for advanced lithium batteries: advances and perspective. Small 14(36):1800821

[91] Ren S, Chang H, He L, Dang X, Fang Y, Zhang L, Li H, Hu Y, Lin Y (2013) Preparation and ionic conductive properties of all-solid polymer electrolytes based on multiarm star block polymers. J Appl Polym Sci 129(3):1131–1142

[92] Zhang J, Ma C, Liu J, Chen L, Pan A, Wei W (2016) Solid polymer electrolyte membranes based on organic/inorganic nanocomposites with star-shaped structure for high performance lithium ion battery. J Membr Sci 509:138–148

[93] Xu H, Wang A, Liu X, Feng D, Wang S, Chen J, Zhang L (2018) A new fluorine-containing star-branched polymer as electrolyte for all-solid-state lithium-ion batteries. Polymer 146:249–255

[94] Li Y, Zhang W, Dou Q, Wong KW, Ng KM (2019) $Li_7La_3Zr_2O_{12}$ ceramic nanofiber-incorporated composite polymer electrolytes for lithium metal batteries. J Mater Chem A 7(7):3391–3398

[95] Zhang X, Ji L, Toprakci O, Liang Y, Alcoutlabi M (2011) Electrospun nanofiber-based anodes, cathodes, and separators for advanced lithium-ion batteries. Polym Rev 51(3):239–264

[96] Liu W, Liu N, Sun J, Hsu PC, Li Y, Lee HW, Cui Y (2015) Ionic conductivity enhancement of polymer electrolytes with ceramic nanowire fillers. Nano Lett 15(4):2740–2745

[97] Zhu P, Yan C, Dirican M, Zhu J, Zang J, Selvan RK, Chung CC, Jia H, Li Y, Kiyak Y, Wu N, Zhang X (2018) $Li_{0.33}La_{0.557}TiO_3$ ceramic nanofiber-enhanced polyethylene oxide-based composite polymer electrolytes for all-solid-state lithium batteries. J Mater Chem A 6(10):4279–4285

[98] Lu Q, He YB, Yu Q, Li B, Kaneti YV, Yao Y, Kang F, Yang QH (2017) Dendrite-free, high-rate, long-life lithium metal batteries with a 3D cross-linked network polymer electrolyte. Adv Mater 29(13):1604460

[99] Kim GT, Appetecchi GB, Carewska M, Joost M, Balducci A, Winter M, Passerini S (2010) UV cross-linked, lithium-conducting ternary polymer electrolytes containing ionic liquids. J Power Sources 195(18):6130–6137

[100] Lin YC, Ito K, Yokoyama H (2018) Solid polymer electrolyte based on crosslinked polyrotaxane. Polymer 136:121–127

[101] Ji J, Li B, Zhong WH (2011) An ultraelastic poly (ethylene oxide)/soy protein film with fully amorphous structure. Macromolecules 45(1):602–606

[102] Younesi R, Veith GM, Johansson P, Edström K, Vegge T (2015) Lithium salts for advanced lithium batteries: Li–metal, Li–O_2 and Li–S. Energy Environ Sci. https://doi.org/10.1039/c5ee01215e.8(7),1905-1922

[103] Ahmad S (2009) RETRACTED ARTICLE: polymer electrolytes: characteristics and peculiarities. Ionics 15(3):309–321

[104] Ue M (1994) Mobility and ionic association of lithium and quaternary ammonium salts in propylene carbonate and γ-butyrolactone. J Electrochem Soc 141(12):3336–3342

[105] Xu K (2004) Nonaqueous liquid electrolytes for lithium-based rechargeable batteries. Chem Rev 104(10):4303–4418

[106] Henderson WA (2014) Electrolytes for lithium and lithium-ion batteries, vol 58. Springer, New York

[107] Niedzicki L, Grugeon S, Laruelle S, Judeinstein P, Bukowska M, Prejzner J, Szczeciñski P, Wieczorek W, Armand M (2011) New covalent salts of the 4 + v class for Li batteries. J Power Sources 196(20):8696–8700

[108] Kim HS, Jeong CS (2011) Electrochemical properties of binary electrolytes for lithium-sulfur batteries. Bull Korean Chem Soc 32(10):3682–3686

[109] Read J (2006) Ether-based electrolytes for the lithium/oxygen organic electrolyte battery. J Electrochem Soc 153(1):A96–A100

[110] Gutmann V (1976) Solvent effects on the reactivities of organometallic compounds. Coord Chem Rev 18(2):225–255

[111] Linert W, Camard A, Armand M, Michot C (2002) Anions of low Lewis basicity for ionic solid state electrolytes. Coord Chem Rev 226(1–2):137–141

[112] Schmeisser M, Illner P, Puchta R, Zahl A, Van Eldik R (2012) Gutmann donor and acceptor numbers for ionic liquids. Chem Eur J 18(35):10969–10982

[113] Wei W, Xu Z, Xu L, Zhang X, Xiong H, Yang J (2018) Flexible ionic conducting elastomers for all-solid-state room-temperature lithium batteries. ACS Appl Energy Mater 1(12):6769–6773

[114] Garcia-Calvo O, Lago N, Devaraj S, Armand M (2016) Cross-linked solid polymer electrolyte for all-solid-state rechargeable lithium batteries. Electrochim Acta 220:587–594

[115] Rupp B, Schmuck M, Balducci A, Winter M, Kern W (2008) Polymer electrolyte for lithium batteries based on photochemically crosslinked poly(ethylene oxide) and ionic liquid. Eur Polymer J 44(9):2986–2990

[116] Souzandeh H, Johnson KS, Wang Y, Bhamidipaty K, Zhong WH (2016) Soy-protein-based nanofabrics for highly efficient and multifunctional air filtration. ACS Appl Mater Interfaces 8(31):20023–20031

[117] Fu X, Jewel Y, Wang Y, Liu J, Zhong WH (2016) Decoupled ion transport in a protein-based solid ion conductor. J Phys Chem Lett 7(21):4304–4310

[118] Yuan B, Luo G, Liang J, Cheng F, Zhang W, Chen J (2019) Self-assembly synthesis of solid polymer electrolyte with carbonate terminated poly(ethylene glycol) matrix and its application for solid state lithium battery. J Energy Chem 38:55–59

[119] Xiao Z, Zhou B, Wang J, Zuo C, He D, Xie X, Xue Z (2019) PEO-based electrolytes blended with star polymers with precisely imprinted polymeric pseudo-crown ether cavities for alkali metal ion batteries. J Membr Sci 576:182–189

[120] Murray V, Hall DS, Dahn JR (2019) A guide to full coin cell making for academic researchers. J Electrochem Soc 166(2):A329–A333

[121] Lagadec MF, Zahn R, Wood V (2019) Characterization and performance evaluation of lithium-ion battery separators. Nat Energy 4:16–25

[122] Doyle M, Fuller TF, Newman J (1994) The importance of the lithium ion transference number in lithium/polymer cells. Electrochim Acta 39(13):2073–2081

[123] Zhou W, Wang S, Li Y, Xin S, Manthiram A, Goodenough JB (2016) Plating a dendrite-free lithium anode with a polymer/ceramic/polymer sandwich electrolyte. J Am Chem Soc 138(30):9385–9388

[124] Li H, Li M, Siyal SH, Zhu M, Le Lan J, Sui G, Yu Y, Zhong W, Yang X (2018) A sandwich structure polymer/polymer-ceramics/polymer gel electrolytes for the safe, stable cycling of lithium metal batteries. J Membr Sci 555:169–176

[125] Lian F, Guan HY, Wen Y, Pan XR (2014) Polyvinyl formal based single-ion conductor membranes as polymer electrolytes for lithium ion batteries. J Membr Sci 469:67–72

[126] Bae J, Li Y, Zhang J, Zhou X, Zhao F, Shi Y, Goodenough JB, Yu G (2018) A 3D nanostructured hydrogel-framework-derived high-performance composite polymer lithium-ion electrolyte. Angewandte Chemie Int Ed 57(8):2096–2100

[127] Leo CJ, Rao GVS, Chowdari BVR (2002) Studies on plasticized PEO–lithium triflate–ceramic filler composite electrolyte system. Solid State Ion 148(1–2):159–171

[128] Liu W, Liu N, Sun J, Hsu P-C, Li Y, Lee H-W, Cui Y (2015) Ionic conductivity enhancement of polymer electrolytes with ceramic nanowire fillers. Nano Lett 15:2740–2745

[129] Wang Y-J, Pan Y, Chen L (2005) Ion-conducting polymer electrolyte based on poly(ethylene oxide) complexed with Li1.3Al0.3Ti1.7(PO4)3 salt. Mater Chem Phys 92:354–360

[130] Chen S, Wang J, Zhang Z, Wu L, Yao L, Wei Z, Xu X (2018) In-situ preparation of poly (ethylene oxide)/Li_3PS_4 hybrid polymer electrolyte with good nanofiller distribution for rechargeable solid-state lithium batteries. J Power Sources 387:72–80

[131] Homma K, Yonemura M, Kobayashi T, Nagao M, Hirayama M, Kanno R (2011) Crystal structure and phase transitions of the lithium ionic conductor Li_3PS_4. Solid State Ion 182(1):53–58

[132] Chen L, Li Y, Li SP, Fan LZ, Nan CW, Goodenough JB (2018) PEO/garnet composite electrolytes for solid-state lithium batteries: from "ceramic-in-polymer" to "polymer-in-ceramic". Nano Energy 46:176–184

[133] Liu L, Chu L, Jiang B, Li M (2019) $Li_{1.4}Al_{0.4}Ti_{1.6}(PO_4)_3$ nanoparticle-reinforced solid polymer electrolytes for all-solid-state lithium batteries. Solid State Ion 331:89–95

[134] Aldalur I, Martinez-Ibañez M, Piszcz M, Rodriguez-Martinez LM, Zhang H, Armand M (2018) Lowering the operational temperature of all-solid-state lithium polymer cell with highly conductive and interfacially robust solid polymer electrolytes. J Power Sources 383:144–149

[135] Aldalur I, Martinez-Ibañez M, Piszcz M, Zhang H, Armand M (2018) Self-standing highly conductive solid electrolytes based on block copolymers for rechargeable all-solid-state lithium-metal batteries. Batter Supercaps 1(4):149–159

[136] Duan H, Yin YX, Zeng XX, Li JY, Shi JL, Shi Y, Wen R, Guo YG, Wan LJ (2018) In-situ plasticized polymer electrolyte with double-network for flexible solid-state lithium-metal batteries. Energy Storage Mater 10:85–91

[137] Nguyen HD, Kim GT, Shi J, Paillard E, Judeinstein P, Lyonnard S, Bresser D, Iojoiu C (2018) Nanostructured multi-block copolymer single-ion conductors for safer high-performance lithium batteries. Energy Environ Sci 11(11):3298–3309

[138] Xiao Y, Jiang L, Liu Z, Yuan Y, Yan P, Zhou C, Lei J (2017) Effect of phase separation on the crystallization of soft segments of green waterborne polyurethanes. Polym Test. https://doi.org/10.1016/j.polymertesting.2017.03.029. 60,160-165

[139] Xu C, Huang Y, Tang L, Hong Y (2017) Low-initial-modulus biodegradable polyurethane elastomers for soft tissue regeneration. ACS Appl Mater Interfaces 9(3):2169–2180

[140] Karimi MB, Khanbabaei G, Sadeghi GMM (2017) Vegetable oil-based polyurethane membrane for gas separation. J Membr Sci 527:198–206

[141] Bao J, Shi G, Tao C, Wang C, Zhu C, Cheng L, Qian G, Chen C (2018) Polycarbonate-based polyurethane as a polymer electrolyte matrix for all-solid-state lithium batteries. J Power Sources 389:84–92

[142] Lee YH, Kim JS, Noh J, Lee I, Kim HJ, Choi S, Seo J, Jeon S, Kim TS, Lee JY, Choi JW (2013) Wearable textile battery rechargeable by solar energy. Nano Lett 13(11):5753–5761

[143] Wang S, Jeung S, Min K (2010) The effects of anion structure of lithium salts on the properties of in situ polymerized thermoplastic polyurethane electrolytes. Polymer 51(13):2864–2871

[144] Cong B, Song Y, Ren N, Xie G, Tao C, Huang Y, Xu G, Bao J (2018) Polyethylene glycol-based waterborne polyurethane as solid polymer electrolyte for all-solid-state lithium ion batteries. Mater Des 142:221–228

[145] Choudhary S, Sengwa RJ (2017) Effects of different inorganic nanoparticles on the structural, dielectric and ion transportation properties of polymers blend based nanocomposite solid polymer electrolytes. Electrochim Acta 247:924–941

[146] Zhang J, Zang X, Wen H, Dong T, Chai J, Li Y, Yue L (2017) High-voltage and free-standing poly (propylene carbonate)/$Li_{6.75}La_3Zr_{1.75}Ta_{0.25}O_{12}$ composite solid electrolyte for wide temperature range and flexible solid lithium ion battery. J Mater Chem A 5(10):4940–4948

[147] Gopalan AI, Santhosh P, Manesh KM, Nho JH, Kim SH, Hwang CG, Lee KP (2008) Development of electrospun PVdF-PAN membrane-based polymer electrolytes for lithium batteries. J Membr Sci 325(2):683–690

[148] Song MK, Kim YT, Cho JY, Cho BW, Popov BN, Rhee HW (2004) Composite polymer electrolytes reinforced by non-woven fabrics. J Power Sources 125(1):10–16

[149] Jeong HS, Choi ESH, Lee SY, Kim JH (2012) Evaporation-induced, close-packed silica nanoparticle-embedded nonwoven composite separator membranes for high-voltage/high-rate lithium-ion batteries: advantageous effect of highly percolated, electrolyte-philic microporous architecture. J Membr Sci 415:513–519

[150] Zhu Y, Wang F, Liu L, Xiao S, Chang Z, Wu Y (2013) Composite of a nonwoven fabric with poly(vinylidene fluoride) as a gel membrane of high safety for lithium ion battery. Energy Environ Sci. https://doi.org/10.1039/c2ee23564a.6(2),618-624

[151] Pitawala J, Navarra MA, Scrosati B, Jacobsson P, Matic A (2014) Structure and properties of Li-ion conducting polymer gel electrolytes based on ionic liquids of the pyrrolidinium cation and the bis(trifluoromethanesulfonyl)imide anion. J Power Sources 245:830–835

[152] Kuo PL, Tsao CH, Hsu CH, Chen ST, Hsu HM (2016) A new strategy for preparing oligomeric ionic liquid gel polymer electrolytes for high-performance and nonflammable lithium ion batteries. J Membr Sci 499:462–469

[153] Lu Q, Fang J, Yang J, Yan G, Liu S, Wang J (2013) A novel solid composite polymer electrolyte based on poly(ethylene oxide) segmented polysulfone copolymers for rechargeable lithium batteries. J Membr Sci 425:105–112

[154] Shi J, Yang Y, Shao H (2018) Co-polymerization and blending based PEO/PMMA/P(VDF-HFP) gel polymer electrolyte for rechargeable lithium metal batteries. J Membr Sci 547:1–10

[155] Smith SA, Williams BP, Joo YL (2017) Effect of polymer and ceramic morphology on the material and electrochemical properties of electrospun PAN/polymer derived ceramic composite nanofiber membranes for lithium ion battery separators. J Membr Sci 526:315–322

[156] Tsao CH, Kuo PL (2015) Poly(dimethylsiloxane) hybrid gel polymer electrolytes of a porous structure for lithium ion battery. J Membr Sci 489:36–42

[157] Wang X, Zhang Y, Zhang X, Liu T, Lin YH, Nan CW (2018) Lithium-salt-rich PEO/$Li_{0.3}La_{0.557}TiO_3$ interpenetrating composite electrolyte with three-dimensional ceramic nano-backbone for all-solid-state lithium-ion batteries. ACS Appl Mater Interfaces 10(29):24791–24798

[158] Zekoll S, Marriner-Edwards C, Hekselman AKO, Kasemchainan J, Kuss C, Armstrong DEJ, Cai D, Wallace RJ, Richter FH, Thijssen JHJ, Bruce PG (2018) Hybrid electrolytes with 3D bicontinuous ordered ceramic and polymer microchannels for all-solid-state batteries. Energy Environ Sci 11(1):185–201

[159] Wang B, Rivard E, Manners I (2002) A new high-yield synthesis of $Cl_3P = NSiMe_3$, a monomeric precursor for the controlled preparation of high molecular weight polyphosphazenes. Inorg Chem 41(7):1690–1691

[160] Yu S, Schmohl S, Liu Z, Hoffmeyer M, Schön N, Hausen F, Tempel H, Kungl H, Wiemhöfer HD, Eichel RA (2019) Insights into a layered hybrid solid electrolyte and its application in long lifespan high-voltage all-solid-state lithium batteries. J Mater Chem A 7(8):3882–3894

[161] Kwon SJ, Kim DG, Shim J, Lee JH, Baik JH, Lee JC (2014) Preparation of organic/inorganic hybrid semi-interpenetrating network polymer electrolytes based on poly (ethylene oxide-co-ethylene carbonate) for all-solid-state lithium batteries at elevated temperatures. Polymer 55(12):2799–2808

[162] Shin WK, Cho J, Kannan AG, Lee YS, Kim DW (2016) Cross-linked composite gel polymer electrolyte using mesoporous methacrylate-functionalized SiO_2 nanoparticles for lithium-ion polymer batteries. Sci Rep 6:26332

[163] Zhang J, Li X, Li Y, Wang H, Ma C, Wang Y, Hu S, Wei W (2018) Cross-linked nanohybrid polymer electrolytes with POSS cross-linker for solid-state lithium ion batteries. Front Chem 6:186

[164] Zhang Y, Lu W, Cong L, Liu J, Sun L, Mauger A, Liu J (2019) Cross-linking network based on Poly (ethylene oxide): solid polymer electrolyte for room temperature lithium battery. J Power Sources 420:63–72

[165] Zhu M, Tan C, Fang Q, Gao L, Sui G, Yang X (2016) High performance and biodegradable skeleton material based on soy protein isolate for gel polymer electrolyte. ACS Sustai Chem Eng 4(9):4498–4505

[166] Fu X, Li C, Wang Y, Kovatch LP, Scudiero L, Liu J, Zhong W (2018) Building ion-conduction highways in polymeric electrolytes by manipulating protein configuration. ACS Appl Mater Interfaces 10(5):4726–4736

[167] Fu X, Wang Y, Fan X, Scudiero L, Zhong WH (2018) Core-shell hybrid nanowires with protein enabling fast ion conduction for high-performance composite polymer electrolytes. Small 14(49):1803564

[168] Kumar B, Scanlon LG (1994) Polymer-ceramic composite electrolytes. J Power Sources 52(2):261–268

[169] Wang X, Fu X, Wang Y, Zhong W (2016) A protein-reinforced adhesive composite electrolyte. Polymer 106:43–52

[170] Chen F, Yang D, Zha W, Zhu B, Zhang Y, Li J, Gu Y, Shen Q, Zhang L, Sadoway DR (2017) Solid polymer electrolytes incorporating cubic $Li_7La_3Zr_2O_{12}$ for all-solid-state lithium rechargeable batteries. Electrochim Acta 258:1106–1114

[171] Bae J, Li Y, Zhao F, Zhou X, Ding Y, Yu G (2018) Designing 3D nanostructured garnet frameworks for enhancing ionic conductivity and flexibility in composite polymer electrolytes for lithium batteries. Energy Storage Mater 15:46–52

[172] Sun Y, Zhan X, Hu J, Wang Y, Gao S, Shen Y, Cheng YT (2019) Improving ionic conductivity with bimodal-sized $Li_7La_3Zr_2O_{12}$ fillers for composite polymer electrolytes. ACS Appl Mater Interfaces 11:13

[173] Zhu L, Zhu P, Yao S, Shen X, Tu F (2019) High-performance solid PEO/PPC/LLTO-nanowires polymer composite electrolyte for solid-state lithium battery. Int J Energy Res 43:4854–4866

[174] Sun Z, Li Y, Zhang S, Shi L, Wu H, Bu H, Ding S (2019) G-C_3N_4 nanosheets enhanced solid polymer electrolytes with excellent electrochemical performance, mechanical properties, and thermal stability. J Mater Chem A 7(18):11069–11076

[175] Chen L, Fan LZ (2018) Dendrite-free Li metal deposition in all-solid-state lithium sulfur batteries with polymer-in-salt polysiloxane electrolyte. Energy Storage Mater 15:37–45

[176] Mindemark J, Sun B, Törmä E, Brandell D (2015) High-performance solid polymer electrolytes for lithium batteries operational at ambient temperature. J Power Sources 298:166–170

[177] Sun B, Mindemark J, Edström K, Brandell D (2014) Polycarbonate-based solid polymer electrolytes for Li-ion batteries. Solid State Ion 262:738–742

[178] Sun B, Mindemark J, Edström K, Brandell D (2015) Realization of high performance polycarbonate-based Li polymer batteries. Electrochem Commun 52:71–74

[179] Mindemark J, Imholt L, Montero J, Brandell D (2016) Allyl ethers as combined plasticizing and crosslinkable side groups in polycarbonate-based polymer electrolytes for solid-state Li batteries. J Polym Sci Part A Polym Chem 54(14):2128–2135

[180] Kimura K, Yajima M, Tominaga Y (2016) A highly-concentrated poly (ethylene carbonate)-based electrolyte for all-solid-state Li battery working at room temperature. Electrochem Commun 66:46–48

[181] Wang A, Xu H, Zhou Q, Liu X, Li Z, Gao R, Wu N, Guo Y, Li H, Zhang L (2016) A new all-solid-state hyperbranched star polymer electrolyte for lithium ion batteries: synthesis and electrochemical properties. Electrochim Acta 212:372–379

[182] Wang S, Wang A, Yang C, Gao R, Liu X, Chen J, Wang Z, Zeng Q, Liu X, Zhou H, Zhang L (2018) Six-arm star polymer based on discotic liquid crystal as high performance all-solid-state polymer electrolyte for lithium-ion batteries. J Power Sources 395:137–147

[183] Chaudoy V, Ghamouss F, Luais E, Tran-Van F (2016) Cross-linked polymer electrolytes for Li-based batteries: from solid to gel electrolytes. Ind Eng Chem Res 55(37):9925–9933

[184] Sakakibara T, Kitamura M, Honma T, Kohno H, Uno T, Kubo M, Itoh T (2019) Cross-linked polymer electrolyte and its application to lithium polymer battery. Electrochimica Acta 296:1018–1026

[185] Pan Q, Zheng Y, Kota S, Huang W, Wang S, Qi H, Li CY (2019) 2D MXene-containing polymer electrolytes for all-solid-state lithium metal batteries. Nanoscale Adv 1(1):395–402

[186] Wang B, Tang M, Wu Y, Chen Y, Jiang C, Zhuo S, Zhu S, Wang C (2019) A 2D layered natural ore as a novel solid-state electrolyte. ACS Appl Energy Mater 2(8):5909–5916

[187] Tang W, Tang S, Zhang C, Ma Q, Xiang Q, Yang YW, Luo J (2018) Simultaneously enhancing the thermal stability, mechanical modulus, and electrochemical performance of solid polymer electrolytes by incorporating 2D sheets. Adv Energy Mater 8(24):1800866

[188] Tang W, Tang S, Guan X, Zhang X, Xiang Q, Luo J (2019) High-performance solid polymer electrolytes filled with vertically aligned 2D materials. Adv Funct Mater 29(16):1900648

[189] Piana G, Bella F, Geobaldo F, Meligrana G, Gerbaldi C (2019) PEO/LAGP hybrid solid polymer electrolytes for ambient temperature lithium batteries by solvent-free, "one pot" preparation. J Energy Storage 26:100947

[190] Fu J, Lu Q, Shang D, Chen L, Jiang Y, Xu Y, Yuan S (2018) A novel room temperature POSS ionic liquid-based solid polymer electrolyte. J Mater Sci 53(11):8420–8435

[191] Cui W, Tang DY, Gong ZL, Guo YD (2012) Performance enhancement induced by electrospinning of polymer electrolytes based on poly(methyl methacrylate-co-2-acrylamido-2-methylpropanesulfonic acid lithium). J Mater Sci 47:6276–6285. https://doi.org/10.1007/s10853-012-6547-3

[192] Zhang N, He J, Han W, Wang Y (2019) Composite solid electrolyte PEO/SN/$LiAlO_2$ for a solid-state lithium battery. J Mater Sci 54(13):9603–9612. https://doi.org/10.1007/s10853-019-03535-3

[193] Guo HL, Sun H, Jiang ZL, Luo CS, Gao MY, Wei MH, Zhou HJ (2019) A new type of composite electrolyte with high performance for room-temperature solid-state lithium battery. J Mater Sci 54(6):4874–4883. https://doi.org/10.1007/s10853-018-03188-8